Rev.	Publish date	Description	Made by	Checked by	Project appro.	Client appro.
0	15.08.2019	Final issue	AGF/FCWH/PGS	RML	SEJ	

Client

Statens vegvesen

Contractor

AAS-JAKOBSEN COWI Multiconsult
JOHS HOLT AkerSolutions entail NGI DISSING+WEITLING architecture a/s mossmaritime

Contract no.:

18/91094

Document name:

Preferred solution, K12 – Appendix H

Global analyses – Special studies

Document no.:	Rev.:	Pages:
SBJ–33–C5–AMC–21–RE–108	0	155

CONCEPT DEVELOPMENT, FLOATING BRIDGE E39 BJØRNAFJORDEN

Preferred solution, K12

Appendix H – Global Analyses - Special studies

AAS-JAKOBSEN COWI Multiconsult

JOHS HOLT AkerSolutions entail NGI DISSING+WEITLING architecture a|s mossmaritime

REPORT

PROJECT	Concept development, floating bridge E39 Bjørnafjorden	DOCUMENT CODE	SBJ-33-C5-AMC-21-RE-108
SUBJECT	Appendix H – Global Analyses - Special studies – K12	ACCESSIBILITY	Restricted
CLIENT	Statens vegvesen	PROJECT MANAGER	Svein Erik Jakobsen
CONTACT	Øyvind Kongsvik Nedrebø	PREPARED BY	Arnt Gunvald Fredriksen Finn-Christian W. Hansen Pål Grøthe Sandnes
		RESPONSIBLE UNIT	AMC

SUMMARY

This report describes the work performed in consideration of special studies in the concept development work of a floating bridge over Bjørnafjorden. Considered effects are hydrodynamic effects such as viscous damping, wave-current interaction, hydrodynamic interaction effects and freeboard exceedance.

Preliminary global analysis with wave-current interaction shows large influence on almost all response variables, partly due to a doppler-shift of the wave excitation frequency and partly due to an additional change in the radiation solution and wave excitation loads due to wave-current interaction. With a current in opposite direction of the waves, the encounter frequencies for the waves on the pontoons are decreased and different eigenmodes are excited. With a current velocity of 1.5 m/s combined with the 100-year easterly wind wave, the resulting motion is significantly increased compared to the zero-current case. Especially the strong axis moment is influenced. The realism of the studied case with an extreme current opposing the extreme wind wave is questionable as extreme currents are believed to be wind-driven. Met-ocean data must be updated in order to find a realistic combination of opposing current and wind waves before the effect on the load effects for the selected concept can be determined.

The hydrodynamic interaction between pontoons has an influence on the response. The effect is found to be largest for the vertical motion and the weak axis moment. Further, the hydrodynamic interaction effect is larger for shorter span widths. This is checked in the global analysis by comparing 100 m span width and 125 m span width, with and without hydrodynamic interaction. The effect may be important for typical fatigue sea states, especially for 100 m pontoon spacings.

The effect of computing full quadratic transfer functions (QTF) in WAMIT for the slowly varying drift loads on a pontoon has been compared with the Newman approximation. The comparison shows that the Newman approximation is conservative for the most relevant wave periods.

A simplified analysis has been performed with an inhomogeneous wave field. A fully uncorrelated wave field between the pontoons have been simulated by changing the phase angle of the wave excitation load coefficients for every pontoon. More analysis is needed, but the preliminary results show that it potentially can give a slight increase in the response. Studies with varying wave height across the fjord have been completed, where the results show some local effects towards the abutments.

A methodology to assess the effect of freeboard exceedance has been developed. The methodology is checked for both a single pontoon and on the global bridge system. The first analysis on the global bridge system in 100-year wind wave event resulted in negligible change in response compared to the equivalent simulation without the methodology.

The effects studied in this report have been considered in terms of their global consequence. They were not explicitly accounted for in the global analysis run in Appendix G, but considered as a requirement to robustness of the design that has affected the design development throughout the project.

0	15.08.2019	Final issue		AGF / FCWH / PGS	R. M. Larssen	S. E. Jakobsen
REV.	DATE	DESCRIPTION		PREPARED BY	CHECKED BY	APPROVED BY

TABLE OF CONTENTS

1   Introduction

This report describes the work performed in consideration of special studies in the concept development work of a floating bridge over Bjørnafjorden. Considered effects/areas are hydrodynamic effects such as viscous damping, wave-current interaction, hydrodynamic interaction effects and freeboard exceedance.

2   Viscous loads on pontoons

This section estimates the viscous loads on a single pontoon. The viscous loads are expressed through a quadratic drag coefficient like in the well-known Morison equation. The considered pontoon is of circtangel shape with length 53 m, breadth 14.9 m and draught 5 m. The focus is on sway, as this is the degree of freedom where viscous forces are expected to be most significant for the global bridge response. Viscous sway damping is expected to be especially important in the swell wave period range, where the potential-flow damping is small.

Although strictly speaking valid for a circular cylinder, we use the Morison equation to describe the loads on the pontoon. The Morison equation takes different forms depending on if the structure is fixed in an ambient flow, moving in still water or a combination of the two. We here refer to the equations as stated in DNVGL-RP-C205 [1]. If the structure is fixed, the sectional normal force (here corresponding to the force per unit draught) is

$$f(t) = \rho(1 + C_A)A\dot{u} + \frac{1}{2}\rho C_D D u|u|,$$

where ρ is the water density, C_A is a mass coefficient, C_D is a drag coefficient, A is the cross-sectional area, D is the diameter and u is the incident fluid particle velocity. If the structure is moving in still water, the Morison equation is written

$$f(t) = -\rho C_A A\ddot{r} - \frac{1}{2}\rho C_D D\dot{r}|\dot{r}|,$$

where r is the position of the structure so that $\dot{r}$ and $\ddot{r}$ are respectively the velocity and acceleration of the structure. For a structure that is moving in waves and/or current, the Morison equation may be written

$$f(t) = -\rho C_A A\ddot{r} + \rho(1 + C_A)A\dot{u} + \frac{1}{2}\rho C_D D u|u| - \frac{1}{2}\rho C_D D\dot{r}|\dot{r}|.$$

The latter equation can alternatively be reformulated using a relative velocity $u_r = u - \dot{r}$ and acceleration $a_r = \dot{u} - \ddot{r}$:

$$f(t) = \rho A\dot{u} + \rho C_A A a_r + \frac{1}{2}\rho C_D D u_r|u_r|.$$

In principle every shape has a specific drag coefficient C_D that needs to be determined separately by model tests or CFD simulations solving the Navier-Stokes equations. The drag coefficient can also be estimated based on empirical data for similar shapes and theoretical considerations. Such estimate is presented in section 2.1. In section 2.2, force coefficients in the Morison equation obtained from CFD analysis are presented. The relation between the empirical/theoretical drag coefficients and those obtained from CFD analysis are discussed in section 2.3. Recommended drag coefficients to be used in the global analysis are proposed.

2.1   Drag coefficient from empirical and theoretical considerations

Using empirical data and theoretical considerations, the drag coefficient is estimated from the following stepwise procedure:

1. Determine the 2-dimensional drag coefficient for steady current from relevant literature

2. Determine the 3-dimensional correction factor for steady current from relevant literature

3. Estimate the KC-number for the case to be considered, based on the expected relative velocity between the pontoon and the water

4. Determine a KC-dependent correction factor to the steady drag coefficient from step 2.

Inherent in each step is the consideration of the roughness due to the marine growth and the effect is has on the drag coefficient.

2.1.1   2-dimensional drag coefficient

Figure 2-1 from [1] gives the 2-dimensional drag coefficient for the considered circtangle shaped pontoon. The pontoon has $L/D \approx 3.5$ and $R/D = 0.5$, for which Figure 2-1 suggests a 2-dimensional drag coefficient between 0.29 and 0.4 for a Reynolds number around 10^5. For a circular cylinder this is below the super-critical flow regime, where the flow separation point changes because of fully turbulent flow and the drag coefficient is reduced. If a Reynolds number of 10^5 is large enough for the flow to be considered fully turbulent for the considered circtangle geometry is however not fully understood and should be subject to further examination. In full scale when the bridge pontoons are installed, the flow conditions are expected to be fully turbulent due to the large Reynolds number, the surface roughness and possibly turbulent inflow conditions.

Geometry		Drag coefficient, C_D					
4. Rectangle with rounded corners		L/D	R/D	C_D	L/D	R/D	C_D
		0.5	0	2.5	2.0	0	1.6
			0.021	2.2		0.042	1.4
			0.083	1.9		0.167	0.7
			0.250	1.6		0.50	0.4
		1.0	0	2.2	6.0	0	0.89
			0.021	2.0		0.5	0.29
			0.167	1.2			
			0.333	1.0			
		$R_e \sim 10^5$					
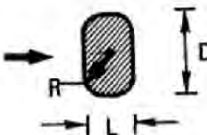
Figure 2-1 Table with 2-dimensional drag coefficient for the circtangle shape from [2]

Note that the change in drag coefficient with respect to the direction of the relative velocity for the considered pontoon is expected to be relatively large. As an example, consider an ellipse with aspect ratio of 1.2. For flow in the longitudinal direction of the ellipse, there will be one separation point at the end of the ellipse. However, for flow in the transverse direction of the ellipse there will be two separation points, one at each side. As a result, the drag coefficient changes significantly between the two cases. Similar flow behaviour can be expected for the considered circtangle shape. A relevant question to ask is how large inflow angle is needed for flow separation to occur at the upstream end. Here however the focus is on the drag coefficient for flow/motion perpendicular to the pontoon longitudinal axis.

2.1.2 3-dimensional drag coefficient

For a circular cylinder the finite length of the cylinder changes the flow locally around the edges. This has mainly two consequences for the flow pattern: At the edge, a tip-vortex is created which isolated leads to an increase in the drag force on the structure. The tip-vortex furthermore creates a downwash that disturbs the flow separation along the rest of the cylinder. The downwash effect reduces the viscous drag force. For cylinders with relatively large aspect ratios AR (H/D), the reduction of the viscous drag force due to downwash is larger than the increased viscous drag force due to the tip vortex. At a critical AR, the downwash from the edge will suppress the vortex separation from the rest of the structure, see for instance [3]. Note that in [3] the conclusion is based on a study with a cylinder of finite length over a flat ground, where the ground-boundary layer thickness influences the results.
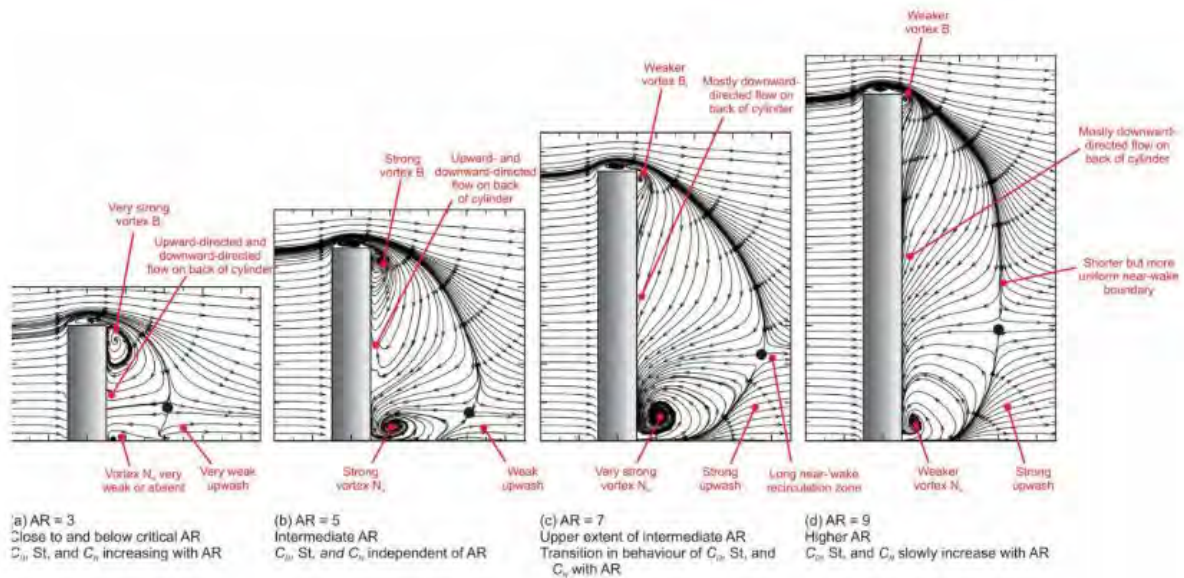
Figure 2-2 Principle sketch of the downwash due to the tip vortex, from [3].

For the present scenario, it is unknown how large influence the vorticity created on bottom of the pontoon has. Figure 2-3 illustrates the vorticity created on top of the cylinder in the case studied by [4].
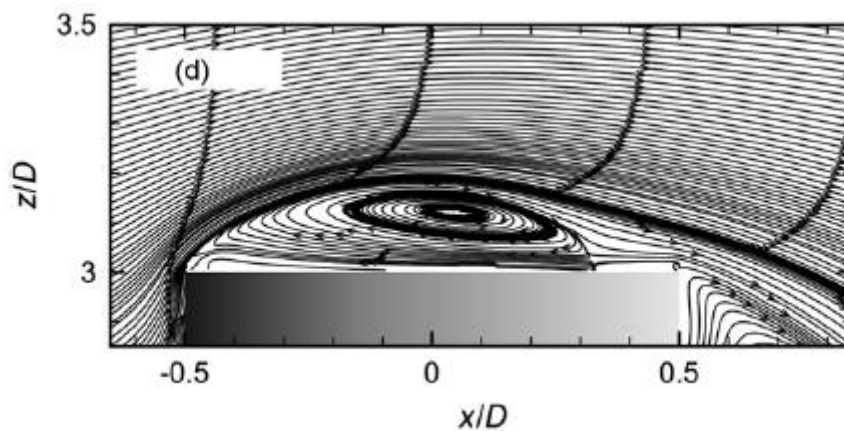

Figure 2-3 Tip-vortex due to flow separation from the front edge of an upright cylinder.

Several studies suggest a reduction of the drag coefficient for the 3-dimensional case compared to the 2-dimensional case for a circular cylinder. It is however not clear if these conclusions can be extrapolated to the circtangle pontoon.

2.1.3 KC-number

The Keulegan-Carpenter number KC is defined as

$$KC = \frac{VT}{L}$$

where *V* is the amplitude of the oscillatory velocity, *T* the period of oscillation and *L* a characteristic length scale. For harmonic motion the KC number can be rewritten as

$$KC = \frac{2\pi A}{L}$$

where *A* is the motion amplitude.

The characteristic length will be relevant for the flow separation. For the 2-dimensional flow, the width of the structure can be a relevant parameter, as it says something about how far the flow has travelled along the half-circle before a possible separation occurs. For the 3-dimensional flow it depends on the relative magnitude of the tip-vortex versus the inline vorticity. If the drag coefficient is dominated by the tip-vortex, it seems natural to use the draught of the structure as the length parameter in estimating the KC-number. Hence, there is no obvious unique definition of the KC number in this case. However, to compare with literature we must use a similar definition as in the relevant sources.

2.1.4 KC-dependent correction factor on the drag coefficient

The behavior of the drag coefficient for a smooth circular cylinder compared to a sharp-edged object is different for low and high KC-numbers. For a smooth circular cylinder, the vortex shedding disappears for low KC-numbers, see illustration of the different flow regimes in Figure 2-4. This reduces the drag coefficient. However, at very low KC-numbers the drag force due to skin friction becomes dominant and the drag coefficient increases again.

For objects with sharp edges, the KC-dependence is somewhat more predictable since the flow will always separate from the sharp corners. Several studies found in the literature report a drag coefficient that is continuously increasing with decreasing KC-number, see for instance [5].

For the present geometry it is difficult to determine which of the two literature cases that are most relevant, since it is consists of a blunt "base shape" but has a sharp edge at the bottom. If the 2-dimensional flow separation governs the viscous force, the KC-number dependence for an infinitely long circular cylinder is relevant. However, if the 3-dimensional effect governs the viscous forces, the KC-number dependence for a sharp edge object is more relevant. Getting closer to answering this question with confidence requires model tests, CFD analysis or ideally a combination of the two.
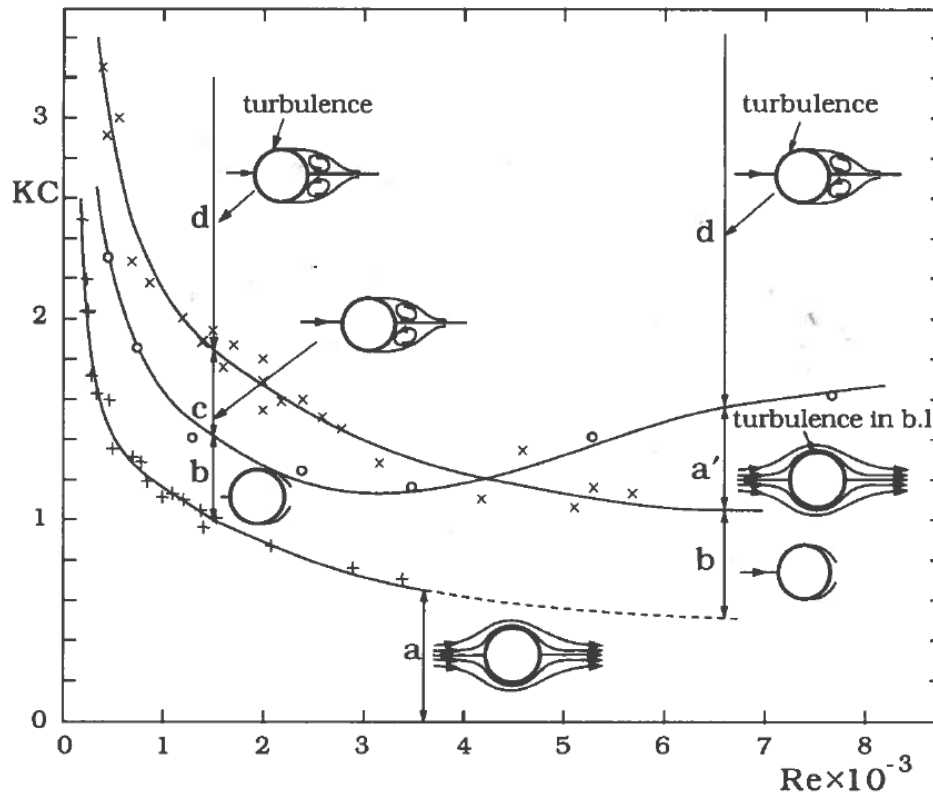
Figure 2-4 Illustrations of the different flow regimes for a smooth circular cylinder, from [6]

2.1.5 Recommended drag coefficient based on literature review

For the present geometry it has been challenging to determine a proper drag coefficient only based on literature for reasons that are discussed above. However, in the early phase of the project it was decided that $C_D = 0.3$ was a reasonable assumption for the drag coefficient in sway based on the literature survey. Some of the effects explained above lean towards increasing this drag coefficient, but there are also effects that would suggest reducing the drag coefficient.

In principle the geometry of the pontoon can be modified to achieve a higher drag coefficient by forcing flow separation, which could be attractive e.g. to increase the viscous damping. However, this will influence other hydrodynamic parameters as well as local structural stresses and strains. Before introducing means to increase the viscous loads on a pontoon, a careful consideration of these effects should be done.

2.2 Force coefficients from CFD analysis

A CFD analysis has been performed by CoreMarine to estimate the drag coefficient in sway of a single pontoon in steady and oscillatory flow. Their results are documented in [7], Enclosure 2.

Here an extended discussion is given together with force coefficients obtained from fitting the force time series from the CFD analysis to the Morison equation.

2.2.1 Analysis setup

The analysis is performed with the IHFOAM version of OpenFOAM, solving the Reynolds averaged Navier-Stokes (RANS) equations for two-phase incompressible flow. The interface between the two phases (air and water) is captured using the volume of fluid (VOF) method. Since the mesh is too coarse to resolve turbulent boundary-layer flow, and since the RANS equations are solved, an SST turbulence model is applied. The pontoon is kept fixed and the free-surface deformation is

neglected, i.e. the free surface is modelled as a frictionless flat plate. The fluid domain is 250x250 m in the horizontal plane and with a water depth of 50 m. Along the vertical outer domain boundaries, uniform (velocity) boundary conditions are given.

2.2.2 Assumptions and simplifications

The choice of incompressible flow in the analysis is deemed reasonable. Solving the compressible Navier-Stokes equations is associated with a substantial increase in CPU time. Moreover, compressibility effects are generally only important when dealing with violent flow phenomena such as slamming or cavitating flows. None of these are relevant here.

Neglecting the deformation of the free surface implies that the time-varying wave elevation due to incident and diffracted surface waves contribute insignificantly to viscous loads. Although these assumptions are not uncommon and clearly simplifies the analysis, their validity is not obvious. As an attempt to verify the assumption, an analysis with the pontoon oscillating in still fluid with a deforming free surface was attempted with rigid wall boundary conditions along the vertical outer walls of the computational domain. However, it was discovered that the dimensions of the fluid domain were too small for this scenario (the fluid disturbances did not die out towards the ends of the domain and this is likely to influence the pressure on the structure due to blockage effects and reflections, see Figure 2-5). Clearly, this type of setup requires a larger domain that than of a fixed cylinder in an ambient flow. Verifying the flat free-surface assumption is hence left as future work.
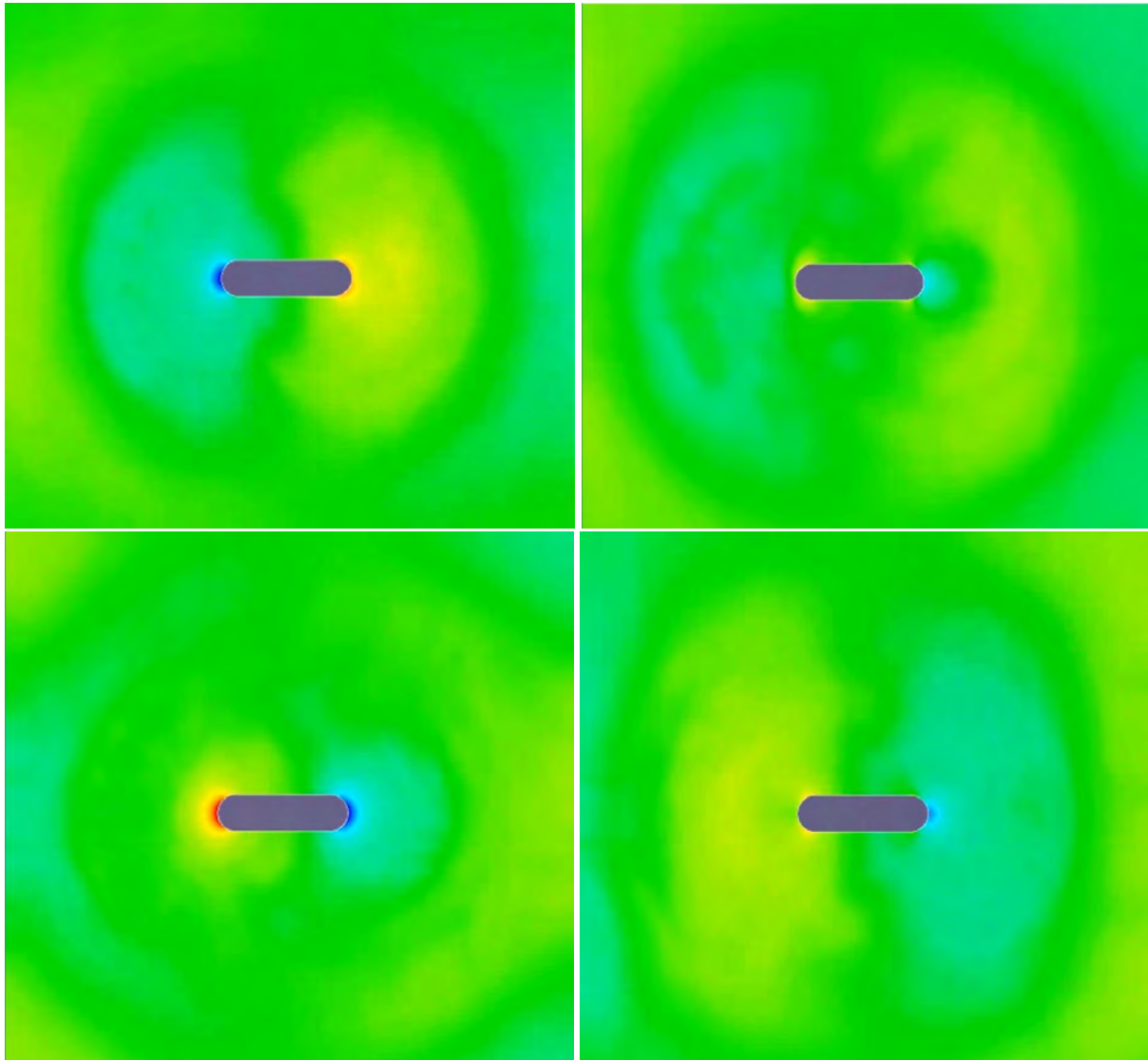
Figure 2-5 Free-surface elevation in computational domain at different time instants for an oscillating pontoon in initially still water. Contour levels: red; elevation 0.25 m, blue; elevation -0.25 m.

While the flow separation from the bottom of the pontoon should be straightforward to predict in the CFD analysis, the separation points along the vertical sides of the pontoon depend amongst others on the turbulence in the boundary layer. The turbulence model used in the analysis may influence this, and hence also the drag coefficient. The turbulence model used in the present analysis has not been validated for this particular project but was chosen based on the CFD analyst's preference and experience.

2.2.3 Results

Processing of CFD data for oscillatory flow

Mass and drag coefficients C_A and C_D are estimated through fitting the Morison equation to the time series of the sway force on the pontoon obtained from the CFD analysis. Since the pontoon is fixed in an ambient flow, we use the following form of the Morison equation:

$$f(t) = \rho(1 + C_A)A\dot{u} + \frac{1}{2}\rho C_D Du|u|.$$

The velocity u and acceleration $\dot{u}$ of the ambient flow are given as

$$u = U_a \cos(\omega t),$$

$$\dot{u} = -\omega U_a \sin(\omega t),$$

where U_a is the velocity amplitude and ω is the oscillation frequency given as $2\pi/T$ with T the oscillation period. It is verified that these analytical expressions for the fluid velocity and acceleration correspond to those imposed in the CFD analysis, see Figure 2-6. In fitting the Morison equation to the CFD results, we apply the velocity as reported from the CFD analysis together with the acceleration estimated from a second order finite-difference method. In general, there is little difference between using the velocity and acceleration reported from the CFD analysis and the analytical values (other than an initial ramp-up that is not represented by the latter).
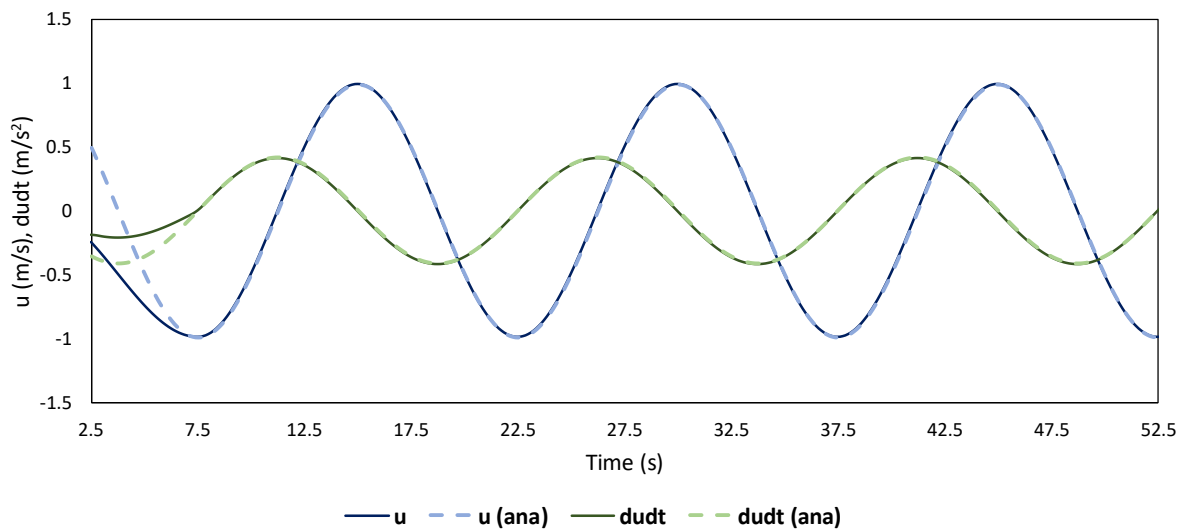
Figure 2-6 Fluid velocity and acceleration for case $KC = 1.0$. The dashed lines correspond to the cosine/sine analytical expressions while the full lines correspond to the values imposed as boundary conditions in the CFD analysis.

The following procedure is followed to fit the Morison equation to the CFD results:

1. Select one period of oscillation between time steps n_1 and n_2 after transient effects have vanished in the CFD results

2. Guess initial values for C_A and C_D

3. Compute the square error $\sum_{n_1}^{n_2}(F_{CFD} - F_{Morison})^2$

4. Use a non-linear solver in Excel to minimize the square error by iterating on C_A and C_D.

The procedure has been verified with a least square approach in pyhton. Another approach has also been attempted where the entire force is assumed to be due to drag when the acceleration is zero and the entire force due to inertia when the velocity is zero. The above procedure to minimize the square error is however found to give a better agreement and is preferred.

For the case where the flow is uniform, the mass force is zero so that the drag coefficient is straightforward to derive. For the oscillatory-flow cases, different values for the flow velocity and oscillation period are considered. These are characterized by two non-dimensional numbers:

The Keulegan Carpenter (KC) number is again defined as

$$KC = \frac{U_a T}{B},$$

where U_a is the velocity oscillation amplitude, T is the oscillation period and B is the pontoon breadth.

The viscous frequency parameter β is defined in [1] as

$$\beta = \frac{Re}{KC},$$

where $Re = UB/\nu$ with $\nu = 1.05 \cdot 10^{-6} \ m^2 s^{-1}$ the kinematic water viscosity. An overview of the simulated cases is given in Table 2-1. It is noted that the cases considered here are the most relevant cases from the CFD analysis. Postprocessing of the CFD results to determine Morison coefficients is done by AMC using simulation data provided by the CFD subcontractor.

Table 2-1 Oscillatory-flow cases in CFD analysis.

Case ID	$KC \ (-)$	$T \ (s)$	$U_a \ (ms^{-1})$	$Re \ (-)$	$\beta \ (-)$
KC = 0.5	0.5	15	0.5	7.10E+06	1.42E+07
KC = 1.0	1	15	0.99	1.40E+07	1.40E+07
KC = 2.0	2	15	1.99	2.82E+07	1.41E+07
KC = 3.0	3	15	2.98	4.22E+07	1.41E+07
KC = 4.0	4	15	3.97	5.63E+07	1.41E+07
KC = 20.0	20	30	9.935	1.41E+08	7.05E+06
KC = 1.0B	1	8	1.87	2.65E+07	2.65E+07
KC = 1.0C	1	25	0.595	8.44E+06	8.44E+06
KC = 2.0B	2	8	3.725	5.29E+07	2.64E+07

Both the total load and the load on individual 1 m strips of the pontoon is reported, see Figure 2-7. We here follow the approach of fitting the coefficients of the Morison equation for each of the five individual strips. Formally, this is more theoretically sound since also the Morison equation is formulated so that it represents the force per unit height of the structure. It also enables us to study the distribution of the drag coefficient as a function of depth, which can give information regarding which flow mechanisms that matter. Finally, the total mass and drag coefficients are taken as the average of the drag coefficients for each strip. It is noted that the forces on the individual strips are found to be in phase with each other. The frictional drag on the flat bottom ("HULL_Bot") is neglected in this procedure, which can be justified by the fact that this force is in orders of magnitude smaller than the forces on any of the vertical strips.
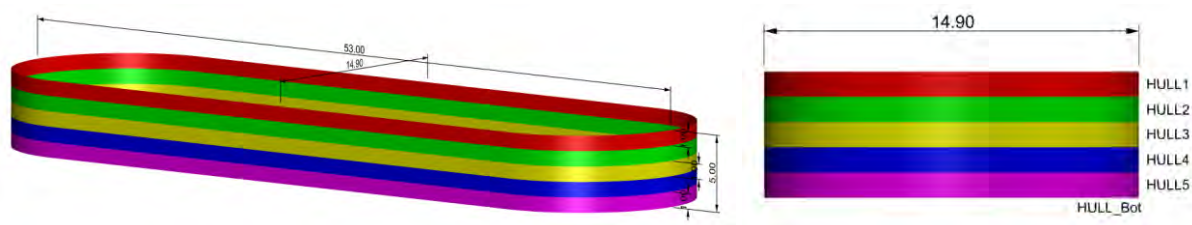

Figure 2-7 CFD model of pontoon hull. The individual load on the strips "HULL1" – "HULL5" are reported.

An example of the fitted Morison forces on each section compared with the CFD results for KC = 1.0 is shown in Figure 2-8. The Morison equation with fitted coefficients is generally seen to reproduce well the CFD forces for all cases in Table 2-1. Hence, the results indicate that the Morison equation is well suited to describe the loading on the pontoon for the studied scenario (oscillatory flow without free-surface deformations).
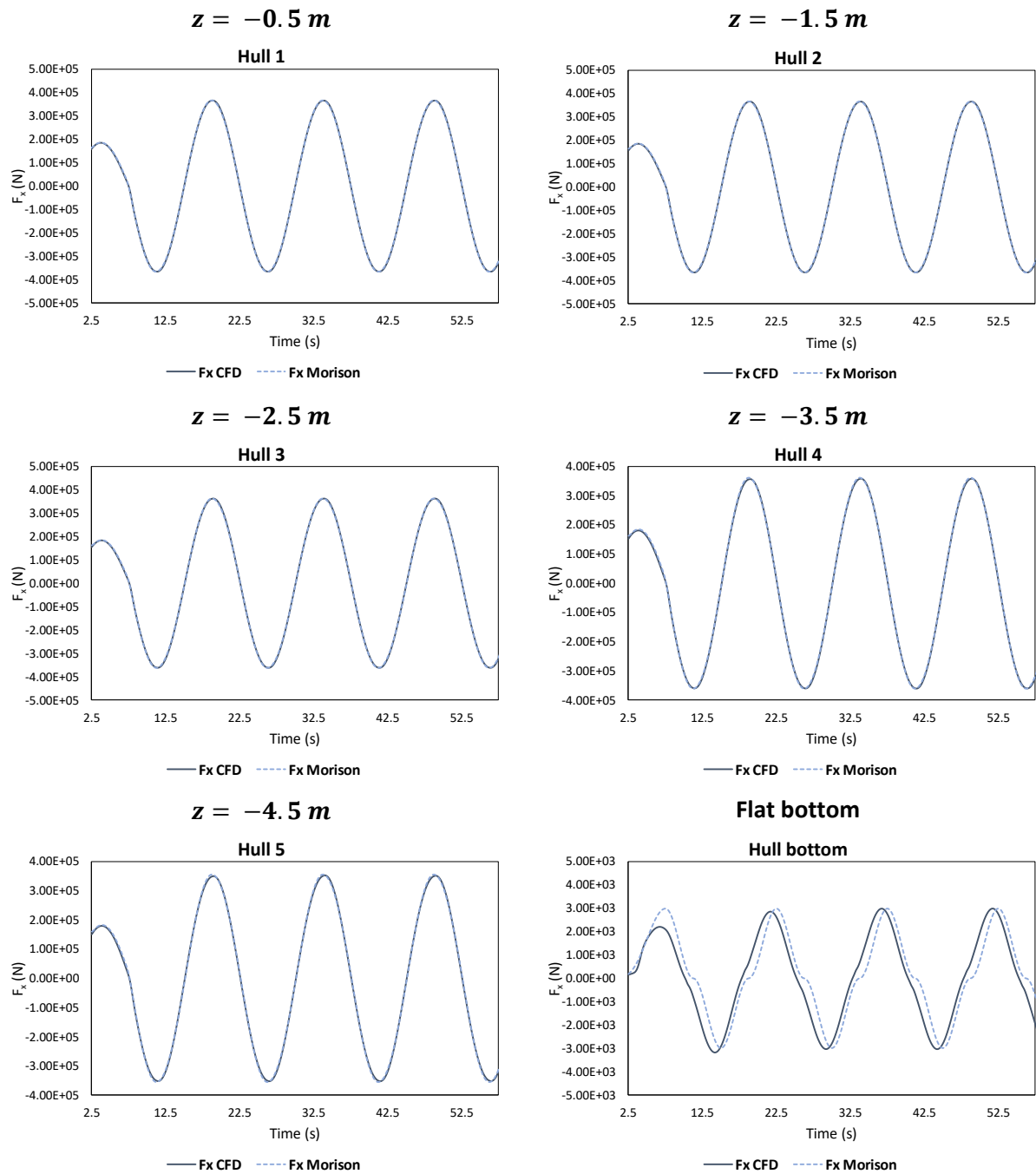
Figure 2-8 Morison equation fitted to sway force on the different structural components in Figure 2-7 from CFD analysis for case KC = 1.0 in Table 2-1.

2.2.4 Discussion of results

Constant (non-oscillatory) current

First we consider the case where the pontoon is placed in a constant flow with uniform flow velocity $U = 1.5\ m/s$. The drag coefficients for flow in surge and sway direction, respectively, are given as

$$C_{D,surge} = \frac{F_{surge}}{\frac{1}{2}\rho L U^2},$$

$$C_{D,sway} = \frac{F_{sway}}{\frac{1}{2}\rho B U^2},$$

where F_{surge} is the force with flow perpendicular to the length dimension and F_{sway} is the force with flow parallel to the length dimension, ρ is the water density, L is the pontoon's length and B is the pontoon's breadth.

The drag coefficients on the individual structural sections in Figure 2-7 are plotted as a function of the distance to the free surface in Figure 2-9. Especially the surge drag coefficient is reduced towards the bottom of the pontoon. The drag coefficient in sway is more uniformly distributed over the depth of the pontoon. Here we see only a small reduction of drag coefficient towards the bottom of the cylinder. This may suggest that flow separation occurs also from the vertical downstream sides of the pontoon, which is also indicated in Figure 2-10 showing the velocity field from the CFD analysis.
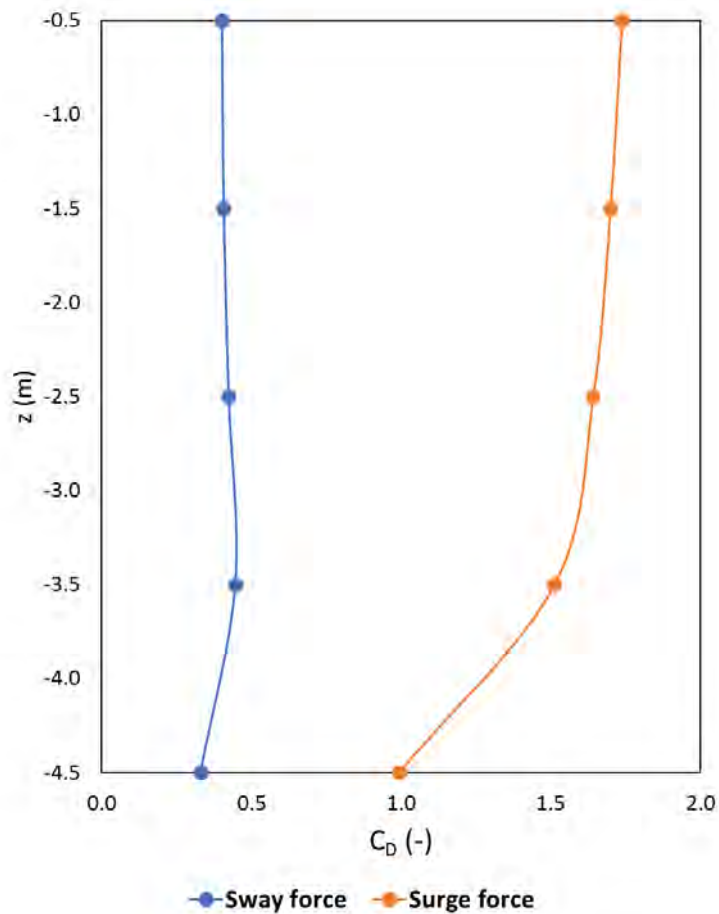
Figure 2-9 Drag coefficients for pontoon in steady flow on individual sections plotted as a function of the vertical coordinate z (the vertical position of the centre of the section relative to the waterline). The sway force is parallel with the longest dimension of the pontoon.

Figure 2-10 Velocity fields for pontoon in steady flow seen in a centre-cut parallel with the pontoons length axis.

The average drag coefficients in steady flow is $C_D = 0.41$ in sway direction and $C_D = 1.52$ in surge direction. In comparison, the sway drag coefficient recommended based on the literature survey in section 2.1.5 was $C_D = 0.3$, i.e. some 25% lower than the CFD value.

Harmonically oscillating current

For the cases with oscillatory flow, we restrict ourselves to consider forces in sway direction with current parallel to the length dimension of the pontoon. The Morison mass and drag coefficients on each section, as well as the average value, for all cases in Table 2-1 are listed in Table 2-2.

Table 2-2 Best-fit mass and drag coefficients in Morison equation, both for the individual structural sections in Figure 2-7 and the average coefficient between all sections. The z-values indicates the vertical position of the centre of the section relative to the waterline.

Case ID	C_A (−)						C_D (−)					
	Hull 1 $z=-0.5m$	Hull 2 $z=-1.5m$	Hull 3 $z=-2.5m$	Hull 4 $z=-3.5m$	Hull 5 $z=-4.5m$	Avg.	Hull 1 $z=-0.5m$	Hull 2 $z=-1.5m$	Hull 3 $z=-2.5m$	Hull 4 $z=-3.5m$	Hull 5 $z=-4.5m$	Avg.
KC = 0.5	0.148	0.145	0.140	0.131	0.111	0.135	3.017	3.038	3.118	3.431	4.871	3.495
KC = 1.0	0.140	0.138	0.133	0.123	0.105	0.128	1.400	1.455	1.601	1.984	2.442	1.776
KC = 2.0	0.142	0.139	0.134	0.124	0.104	0.129	0.906	0.958	1.099	1.372	1.324	1.132
KC = 3.0	0.142	0.140	0.134	0.122	0.099	0.127	0.807	0.844	0.932	1.079	0.994	0.931
KC = 4.0	0.142	0.139	0.133	0.121	0.097	0.126	0.754	0.788	0.863	0.984	0.904	0.859
KC = 20.0	0.131	0.132	0.133	0.135	0.124	0.131	0.467	0.495	0.548	0.632	0.605	0.549
KC = 1.0B	0.159	0.157	0.152	0.142	0.123	0.147	2.295	2.346	2.494	2.887	3.301	2.665
KC = 1.0C	0.134	0.131	0.126	0.117	0.099	0.121	0.999	1.065	1.219	1.581	2.107	1.394
KC = 2.0B	0.157	0.154	0.149	0.138	0.117	0.143	1.403	1.456	1.597	1.869	1.813	1.628

The Morison mass coefficients are plotted as a function of the KC number in the upper panel of Figure 2-11. In the lower panel, the mass coefficients are plotted as function of β for KC = 1.0. Similar plots for the drag coefficients are given in Figure 2-12. In general, the average mass coefficient is insensitive to KC and equal to $C_A \approx 0.13$ if $KC \gtrsim 1.0$. A somewhat stronger KC dependence is observed for the lowest section (z = -4.5 m), which is likely related to flow separation from the pontoon bottom. The mass coefficients tend to increase weakly with β.
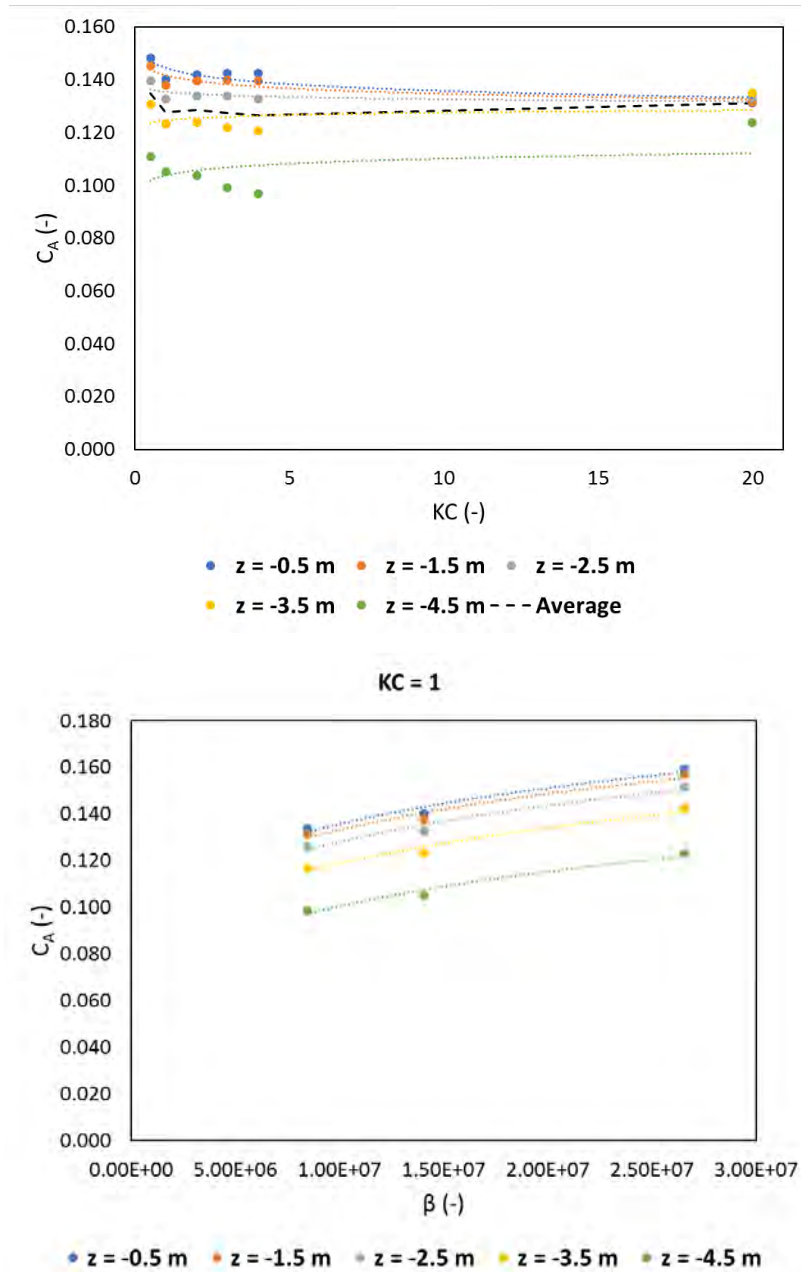
Figure 2-11 Mass coefficients for pontoon in oscillatory flow. The lower plot shows results for $KC = 1$ with three different values of $\beta = Re/KC$. The dashed lines in the upper plot are curve fits on the form $a \cdot KC^b$ and in the lower plot on the form $a \cdot \beta^b$, where a and b are arbitrary coefficients.

From Figure 2-12, the drag coefficient depends strongly on the KC number, in particular for KC numbers below approximately 2.0. This is qualitatively consistent with the wake amplification factor, i.e. the ratio between the drag coefficient in oscillatory and stationary flow, given in DNVGL-RP-C205 [1] where the drag coefficient for an infinitely long circular cylinder is seen to increase significantly for low KC numbers. The magnitude of the increase as well as the KC number where it starts to do so, however, cannot be directly compared since the pontoon's shape is substantially different from an infinitely long circular cylinder and hence other *quantitative* results should be expected. We also note that when the KC number increases, the drag coefficient tends towards the constant-flow value of 0.41, as it logically should. However, it is possible that even higher KC numbers have to be considered in order to reach the exact same value (in [1] a KC number of 60 is required for the wake amplification factor to be exactly equal to unity). At $KC = 20$, [1] suggests a wake amplification

factor of approximately 1.25. In our case we have $0.549/0.41 \approx 1.34$, which is considered a reasonable agreement given that the results are for different geometrical shapes.

For $KC = 1$, it is found that the drag coefficient increases somewhat with β. This tells us that the β parameter do have some importance for the results at low KC numbers (a Reynolds dependency so that the period of oscillation has an effect).

KC = 1
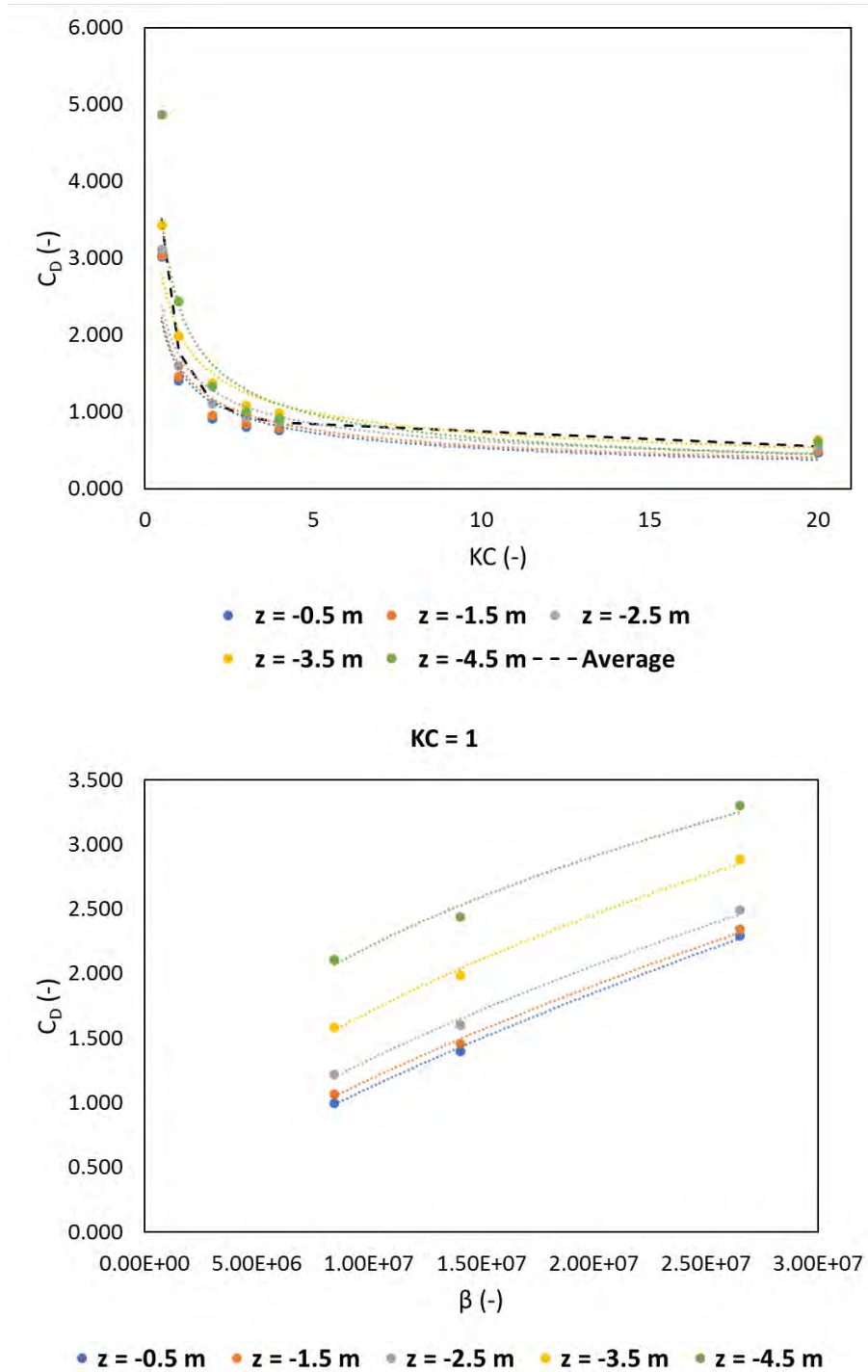
Figure 2-12 Drag coefficients for pontoon in oscillatory flow. The lower plot shows results for $KC = 1$ with three different values of $\beta = Re/KC$. The dashed lines in the upper plot are curve fits on the form $a \cdot KC^b$ and in the lower plot on the form $a \cdot \beta^b$, where a and b are arbitrary coefficients.

In Figure 2-13, the drag coefficient on each pontoon section is plotted as a function of the sections' mean submergence. Especially for low KC numbers the drag coefficient tends to increase towards the

bottom of the pontoon, while for higher KC numbers the drag coefficient is more uniformly distributed over the draught similar to the constant-flow curve for sway in Figure 2-9. One may anticipate that for low KC numbers, the flow will not separate properly from the vertical pontoon sides, whereas the flow will always separate from the pontoon bottom where there is a sharp edge. In this interpretation, the results suggest that the flow separation from the pontoon bottom contributes to substantially increase the viscous drag force on the pontoon at low KC numbers. Although not conclusive, the results do also suggest that the β dependence is stronger for low KC numbers than for higher ones (indicated by looking at "KC = 1.0B" relative to "KC = 1.0" compared to "KC = 2.0B" relative to "KC = 2.0").
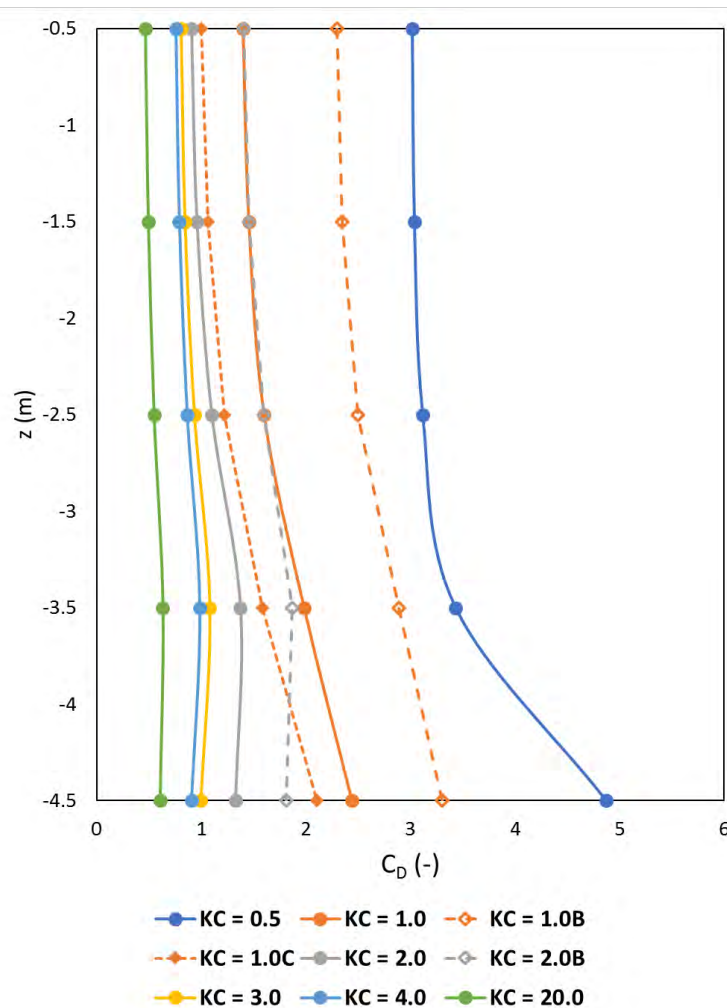

Figure 2-13 Morison drag coefficients for pontoon in oscillatory flow on individual sections plotted as a function of the vertical coordinate z (the vertical position of the centre of the section relative to the waterline). All cases defined in Table 2-1 are included in the plot.

Constant and harmonically oscillating current superimposed

An additional analysis was performed to investigate the effect of having an oscillatory current superimposed on a constant current. The oscillatory flow has velocity amplitude period $U_a = 0.99 \ m/s$ and period $T = 15 \ s$, while the steady current has velocity $U = 1.0 \ m/s$. Following [1], the combined KC number for this scenario is defined as

$$KC = \frac{(U_a + U)T}{B} \approx 2.0.$$

Hence, the constant current effectively increases the KC number, and according to Figure 2-12 one would expect the drag coefficient to decrease. This is indeed the case; the depth-averaged mass and drag coefficients for this case are found to be $C_a = 0.123$ and $C_d = 0.66$. This can be compared to the case $KC = 1.0$ which is similar expect from the constant current. This case gave be $C_a = 0.128$ and $C_d = 1.78$. Hence, the mass coefficient is not significantly influenced by the constant current whereas the drag coefficient is reduced because of an increased KC number. The distribution of the drag coefficient over the individual strips is plotted in Figure 2-14, where the case with constant and oscillatory current superimposed denoted "KC = 1.0D" is compared with the other simulations with KC = 1.0 and 2.0, respectively. Clearly the drag coefficient is more uniformly distributed when the constant current is introduced than for the other KC = 1.0 cases, and qualitatively more like KC = 2.0.
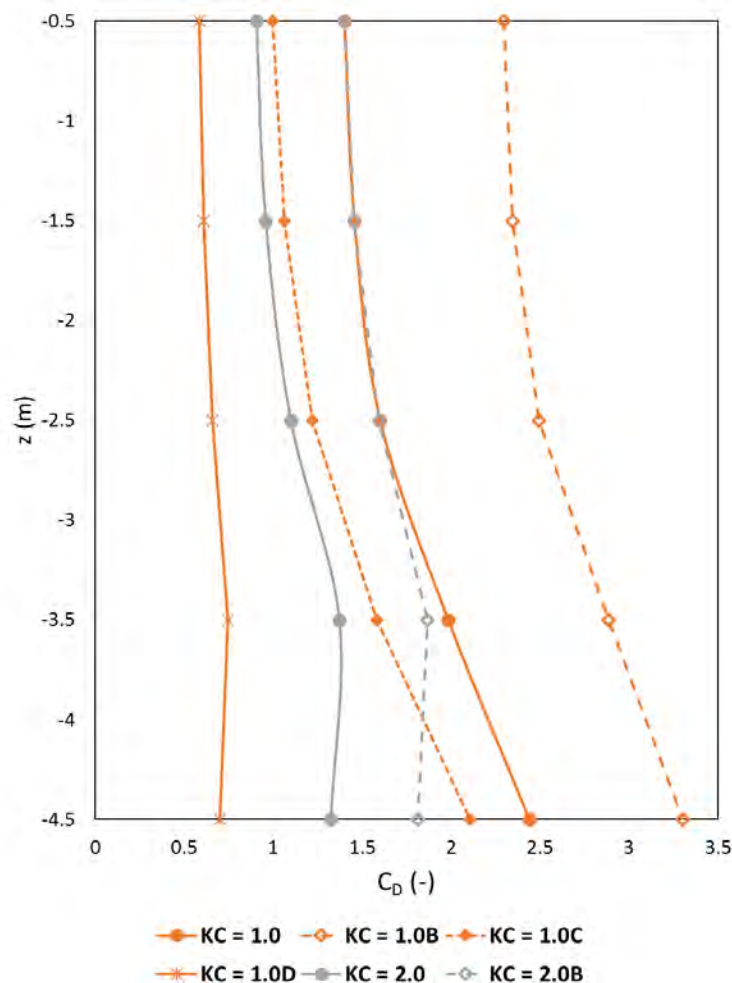
Figure 2-14 Morison drag coefficients for pontoon in oscillatory flow on individual sections plotted as a function of the vertical coordinate z (the vertical position of the centre of the section relative to the waterline). The case with a constant and oscillatory current superimposed is denoted "KC = 1.0D".

More work is required to understand fully how different combinations of oscillatory and constant current influences the drag forces. It may also be more relevant to define the KC number in a different manner. Nevertheless, it seems evident that a constant current tends to reduce the drag coefficient. It is further recommended that *one* common drag coefficient is used in the global analysis that combines the current and the oscillatory flow.

2.2.5 Discussion of uncertainty in CFD analysis

There are indeed aspects that gives confidence in the accuracy of the adequacy of the performed CFD analysis:

- The mass coefficient is less sensitive to the KC number than the drag coefficient, as is also indicated in DNVGL-RP-C205 [1]

- The drag coefficient has a well-defined decrease with increasing KC numbers and tends asymptotically towards the value found for stationary-flow conditions.

Especially for low KC numbers, the obtained drag coefficient is somewhat sensitive to the way of fitting the CFD force time series to the analytical (Morison) force time series. To estimate reliable drag coefficients at low KC numbers is generally known to be a challenging task. Even though the results from the CFD analysis have an apparently logical behaviour both with respect to KC number and the importance of the flow separation from the sharp edge at the bottom, the absolute values of the mass and drag coefficients have not been validated against model tests. Eventually, this is necessary in order to increase the confidence to the level required for future phases of the project. There are also other sources of uncertainty that has not been clarified in the present analysis and that may be of importance:

- The structure will generate waves when it oscillates, and moreover there will be incident waves that will disrupt the generation of vorticity. Hence, the assumption that free-surface deformations can be neglected may not always be adequate. An attempt was made to verify this assumption, but as described in section 2.2.2, these results were disqualified due to a too small domain.

- Here the scenario studied is a fixed pontoon in a harmonically oscillating flow. Generally, waves in the ocean are irregular and not necessarily well described by Airy wave theory. Although the draught of the pontoon is small, the wave particle velocity may vary slightly over the draught. It is possible that the idealized conditions used in the CFD analysis not fully reflects the wave loading in a realistic condition.

- Boundary-layer turbulence is important especially for the drag forces due to flow separation from a smooth wall. For sharp edges, such as the bottom of the pontoon, the turbulence has less importance since the flow always separates at the sharp corner. Thus, the drag forces due to flow separation from the upright cylinder walls contains some uncertainty because the verification of the turbulence model is not properly documented. When flow separation from the bottom edge dominates, however, there is less uncertainty. One may therefore claim that the choice of turbulence model leads to some uncertainty for the value of the drag coefficient, but this uncertainty is smaller for very low KC numbers than for larger KC numbers (because the flow separation from the bottom edge appears to be more dominant at low KC numbers).

- Since the drag coefficient is highly dependent of parameters such as KC and β, one should consider this as a sea-state dependent parameter. Thus, it is difficult to indicate a single value to be used in the analysis model without including significant uncertainty. An alternative is to, at a later stage when the general uncertainty is reduced, have a functional relationship that expresses the drag coefficient to be used as a function of fundamental sea state parameters and pontoon motions.

- The convergence studies performed for the time step in the CFD analysis is not performed with the high Reynolds number cases in mind. Hence, there is some additional uncertainty

for the results with high β especially. Further time step convergence studies are necessary in future studies.

- Turbulence modelling of the wake. The flow pattern for every structure can be considered to be unique and hence the turbulence model that fitted the experimental data for one structure might not be applicable for the next.

In order to reduce the level of uncertainty in relation to the choice of drag coefficient in general and in the CFD analysis, the following is suggested:

1. *Short term:* Do more CFD work to investigate properly the effect of the free surface deformation, incident waves, turbulence modelling etc.

2. *Long term:* Do model tests designed to extract the mass and drag coefficients on a single pontoon both in idealized conditions (such as here studied in the CFD analysis) and in realistic conditions (i.e. being part of a larger bridge model and subject to motions and incident current, waves and possibly wind).

Neglecting the uncertainty due to the simplified conditions studied, the consistency of the CFD results does give confidence that the obtained mass and drag coefficients are realistic. Hence, the CFD results add value to the present phase of the project.

2.3   Discussion and recommendations

The drag coefficient suggested from the CFD analysis in steady-flow conditions is 0.41, which is somewhat higher than the value of 0.30 estimated based on literature review. To add some conservatism, the following procedure is suggested:

- Let the KC-dependence be expressed by the draught-averaged drag coefficient in Figure 2-12

- Multiply the KC-dependent drag coefficients with a correction factor 0.30/0.41 for oscillating flow.

- Use 0.41 as drag coefficient for stationary flow.

This gives a set of data points, where linear interpolation can be assumed between them, as presented in Figure 2-15. The values are tabulated in Table 2-3. It is conservatively assumed that the drag coefficient for KC < 1.0 is equal to the value at KC = 1.0. Furthermore, it is assumed that at KC = 60 the drag coefficient is equal to in steady-flow conditions.
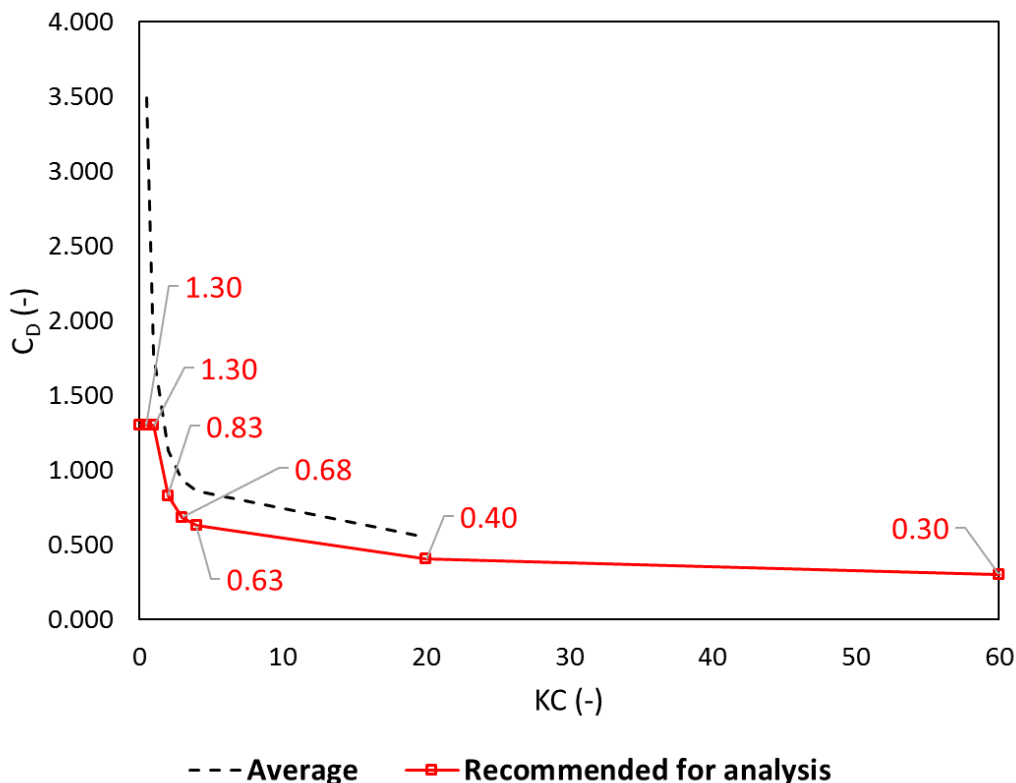
Figure 2-15 KC-dependent Morison drag coefficients for pontoon proposed for global analysis model (red line with square markers). The numbers indicate the value of the drag coefficient in the different data points.

Table 2-3 Value of drag coefficient in sway for various values of the KC number.

$KC = U_aT/B$	C_D
0.00	1.30
0.50	1.30
1.00	1.30
2.00	0.83
3.00	0.68
4.00	0.63
20.00	0.40
60.00	0.30

The method proposed here is a pragmatic one that combines a confidence in that the CFD results are qualitatively correct with the uncertainty that is inherent in the CFD analysis and the value of the drag coefficient in general at very low KC numbers. It is believed that the proposed functional $KC - C_D$ relationship yields values for C_D on the conservative side (in terms of the amount of damping originating from viscous effects).

In using these data, it is important to realize that the Keulegan-Carpenter number is defined as

$$KC = U_aT/B,$$

where T might be approximated as the peak spectral period T_p in an irregular sea state and $U_a = 0.5\omega_p H_s$ with $\omega_p = 2\pi/T_p$ and H_s the significant wave height. Other ways to define U_a and T may be equally valid/suitable.

It is also important to ensure that the drag force is defined in the same way as assumed here, i.e.

$$F_D = \frac{1}{2}\rho A_{proj}C_D U^2$$

Where A_{proj} is a projected area. If the definition differs, the drag coefficient must be modified accordingly.

In order to further reduce this uncertainty and increase the accuracy of the viscous loading on the pontoon, it is recommended to do dedicated model tests in future phases. Since the drag forces are much smaller than the inertia forces, one must design these tests in a clever way so that the drag force can be extracted in a reliable manner. Furthermore, model tests can give additional information regarding possible added damping (and excitation) in waves. One should also do additional CFD studies, using the model tests to validate these. A properly validated CFD model enables more thorough parameter studies to be performed with increased confidence in the results.

3 Wave-current interaction

Wave-current interaction effects are examined by performing hydrodynamic analysis in Wasim [8] and comparing hydrodynamic coefficients, i.e. radiation and wave excitation loads, with results obtained with Wadam (Wamit) [9].

3.1 Theory

Wasim is a program developed for the purpose of analyzing loads and response of a vessel with forward speed (as long as the vessel is not planing) in time domain. The fact that the analysis is performed in time domain implies that in order to compute wave excitation loads, the vessel must be fixed (i.e. restricted form undergoing wave-frequency motions), and to compute wave radiation loads, the vessel must be subject to forced oscillations in the motion-mode of interest. Hence, to perform analysis in Wasim is a more comprehensive task than to perform analysis in frequency domain in Wadam or Wamit.

Wasim uses the Rankine panel method, as opposed to Wadam or Wamit that use Green functions (that automatically satisfies the linear free-surface condition). Hence, not only the wetted part of the hull but also a portion of the free surface must be discretized in Wasim.

Wasim can be run both as a linear and non-linear analysis. The latter is strictly speaking not a fully non-linear analysis since e.g. the radiation potential is still linear. In the present analysis, the linear option is used, which is sufficient because the wave-current interaction problem is covered by linear theory.

Some relevant aspects, largely taken from a presentation given by Torgeir Vada in DNV GL [10], are summarized below.

The combined linear kinematic and dynamic free-surface condition is modified to

$$\frac{\partial^2 \varphi}{\partial t^2} - 2U\frac{\partial^2 \varphi}{\partial t \partial x} + U^2\frac{\partial^2 \varphi}{\partial x^2} + g\frac{\partial \varphi}{\partial z} = 0 \ on \ z = 0,$$

where φ is the velocity potential, U is the forward speed (or equivalently the current velocity) and g is the acceleration of gravity. The two terms in red are due to wave-current interaction, while the remainder of the equation is similar as the one that applies in Wadam/Wamit with zero velocity.

An important parameter to assess the importance of wave-current interaction effects, and the applicability of a theory, is the non-dimensional frequency

$$\tau = \frac{U\omega_e}{g},$$

where ω_e is the frequency of encounter given as

$$\omega_e = \omega_0 + kU cos(\beta - \alpha).$$

ω_0 is here the wave frequency, k is the wavenumber, β is the wave direction and α is the current direction. Physically, this means that if the current is in opposite direction of the waves the wavelength will increase and vice versa. There is a numerical singularity at $\tau = 0.25$, around where one should pay particular attention towards the accuracy of numerical results. Values for ω_e and τ for relevant conditions in the present analysis are shown in Figure 3-1 below. Clearly, the only scenarios where τ is close to 0.25 is for $U = -1m/s$ and $-2m/s$ around $T = 3s$ and for $U = 2m/s$ around $T = 6s$. This is to be kept in mind when analyzing the numerical results. A positive value of U means that the current direction and wave direction coincide, while a negative value means that the current direction is opposite of the wave direction. Based on the figures, one may expect that the

wave-current interaction effects are stronger for low and intermediate wave periods than for longer wave periods typically associated with swells.
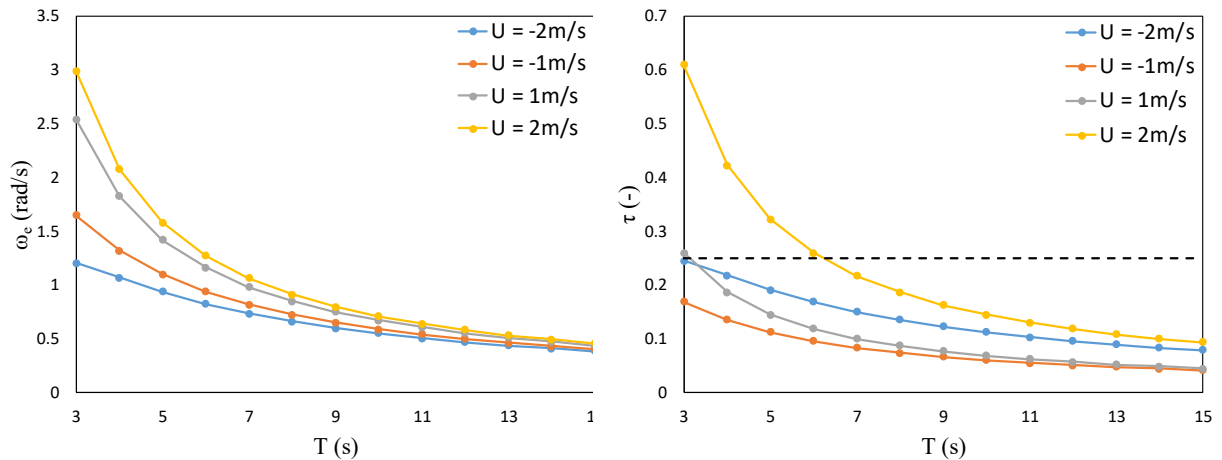

Figure 3-1 Frequency of encounter ω_e and non-dimensional wave frequency τ plotted as function of the incident wave period T.

In order to establish the diameter of the free-surface mesh to be used in Wasim, it is of interest to examine the wavelength associated with the encounter frequency, i.e. $\lambda_e = 2\pi/k_e$ where $k_e = \omega_e^2/g$. These are plotted in Figure 3-2.
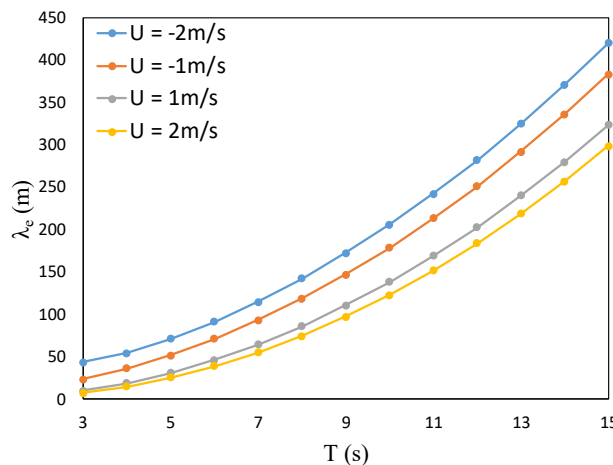
Figure 3-2 Wavelength λ_e associated with encounter wave plotted as function of the incident wave period T.

3.2   Numerical model

The free-surface mesh used in the analysis is shown in Figure 3-3. The diameter of the mesh is approximately 650m, i.e. longer than any of the wave lengths in Figure 3-2, but with a diameter slightly lower than λ_e for wave periods $T > 13s$ when the current direction is opposite of the wave direction. However, as noted in the Wasim user manual [8], it is often sufficient that the mesh has an extent at least five times the length of the vessel. This condition is here satisfied. Based on these two criteria, the extent of the applied mesh is considered sufficient.
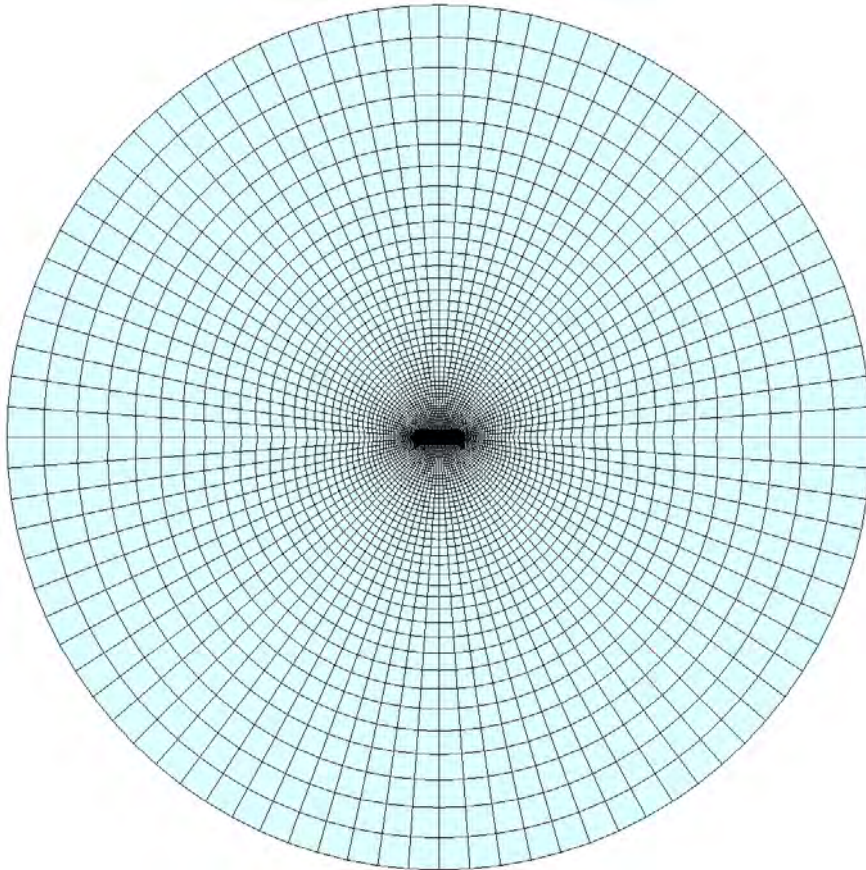
Figure 3-3 Wasim free-surface mesh seen from above.

The hull mesh, as well as the details of the free-surface mesh close to the pontoon, are shown in Figure 3-4. The hull mesh is refined in vertical direction close to the free surface, and the number of panels in the horizontal directions is established with short wavelengths in mind.
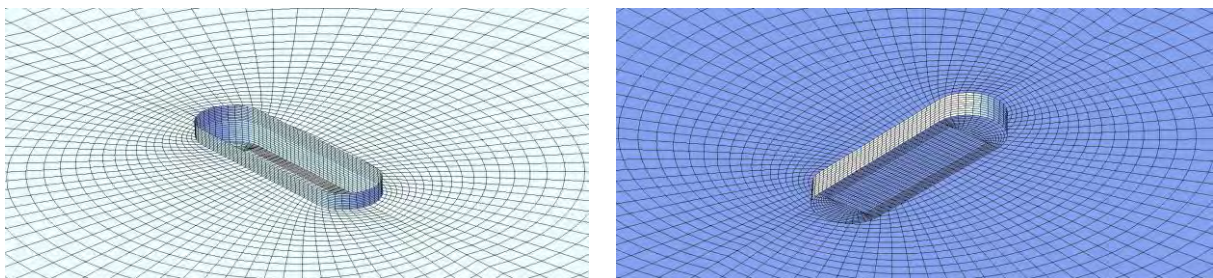
Figure 3-4 Wasim model seen from above and below.

3.3 Analysis cases

Due to symmetry, only wave directions $\beta = 0 - 90°$ are simulated with a spacing $\Delta\beta = 10°$. In addition to $U = 0m/s$, current velocities $U = 1m/s$ and $U = 2m/s$ are simulated with current directions $\alpha = 0°$ and $\alpha = 180°$.

For each case in the analysis matrix, simulations are performed with the pontoon fixed (in order to obtain wave excitation loads) and forced harmonic motions in surge, sway, heave, roll, pitch and yaw in order to obtain wave radiation loads.

Since the analysis is performed in time domain, a Fourier analysis is performed to express the results in frequency domain for comparison with Wadam results. The Fourier analysis is performed by an internal function included in Wasim.

3.4   Results wave excitation

We here compare results with Wadam analysis without any current. With respect to wave excitation loads, we may separate the effect of the current into two parts:

1.   A pure Doppler-shift effect

2.   What we may refer to as additional wave-current interaction effects.

If the former effect dominates, the wave excitation loads computed in Wasim can be expected to compare well with Wadam results plotted as a function of the encounter frequency. Otherwise, one may conclude that there are important wave-current interaction effects that are beyond a simple shift of frequency.

The wave excitation loads in sway, heave and roll for wave directions $\beta = \{0°, 20°, 40°\}$ are shown in the following figures, with motions and wave and current directions defined in Figure 3-5.
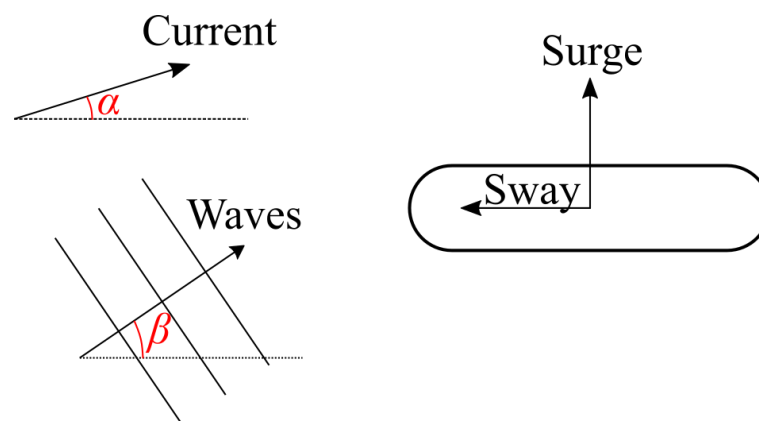
Figure 3-5 Definition of environmental directions and motions.

The Wasim results with zero current are in good agreement with Wadam, which gives confidence that the numerical setup in Wasim is adequate.

The general observations to be made from the results are:

- In sway, there are significant wave-current interaction effects that are not fully accounted for by introducing a Doppler shift in the Wadam results. This is especially evident for T_e larger than $6 - 8 \, s$, depending on the current velocity. Amplitudes are more affected than phase angles.

- In heave, the excitation is well represented in Wadam if the Doppler shift is considered. The effect of additional wave-current interactions is small.

- In roll, wave-current interaction effects appear to give a significant increase in the wave excitation moment beyond introducing the Doppler shift in the Wadam results. The deviation can be seen over a broad range of encounter periods, and phase angles are affected.
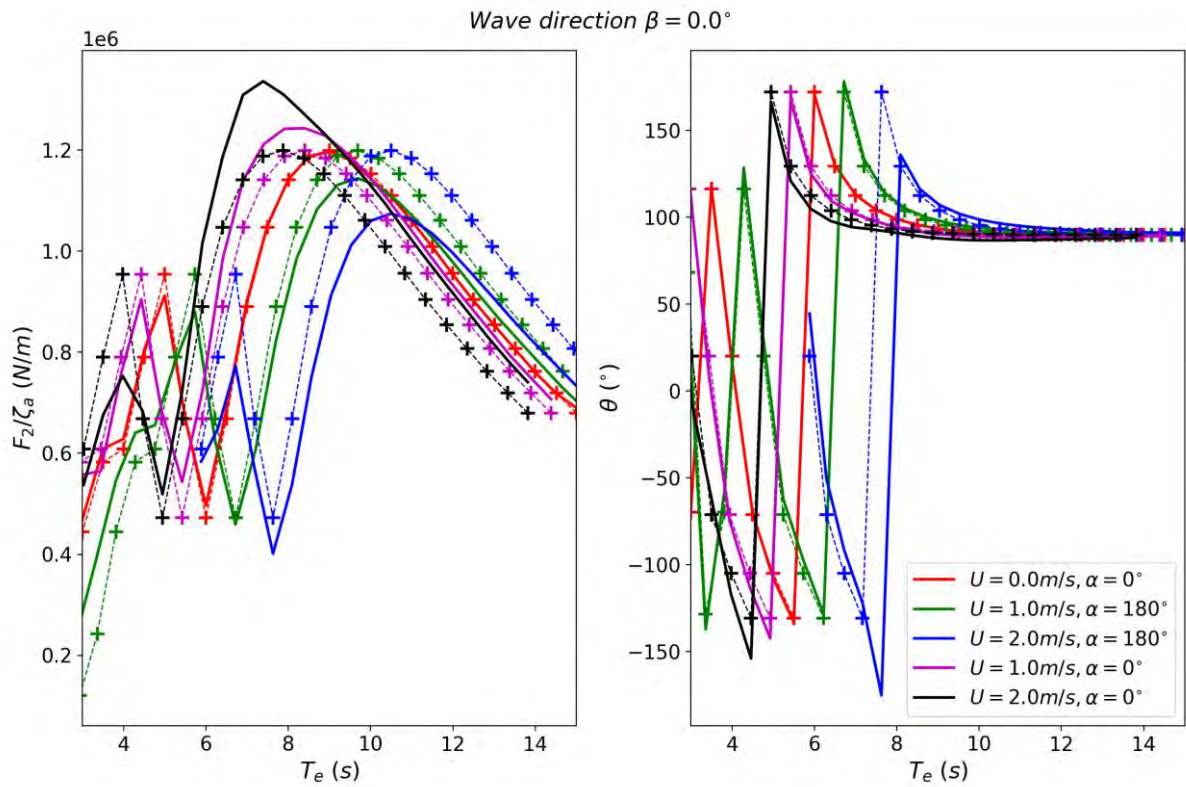
Figure 3-6 Wave excitation loads in sway, wave direction 0°. Wadam results plotted as a function of encounter period T_e are dashed with (+) markers.
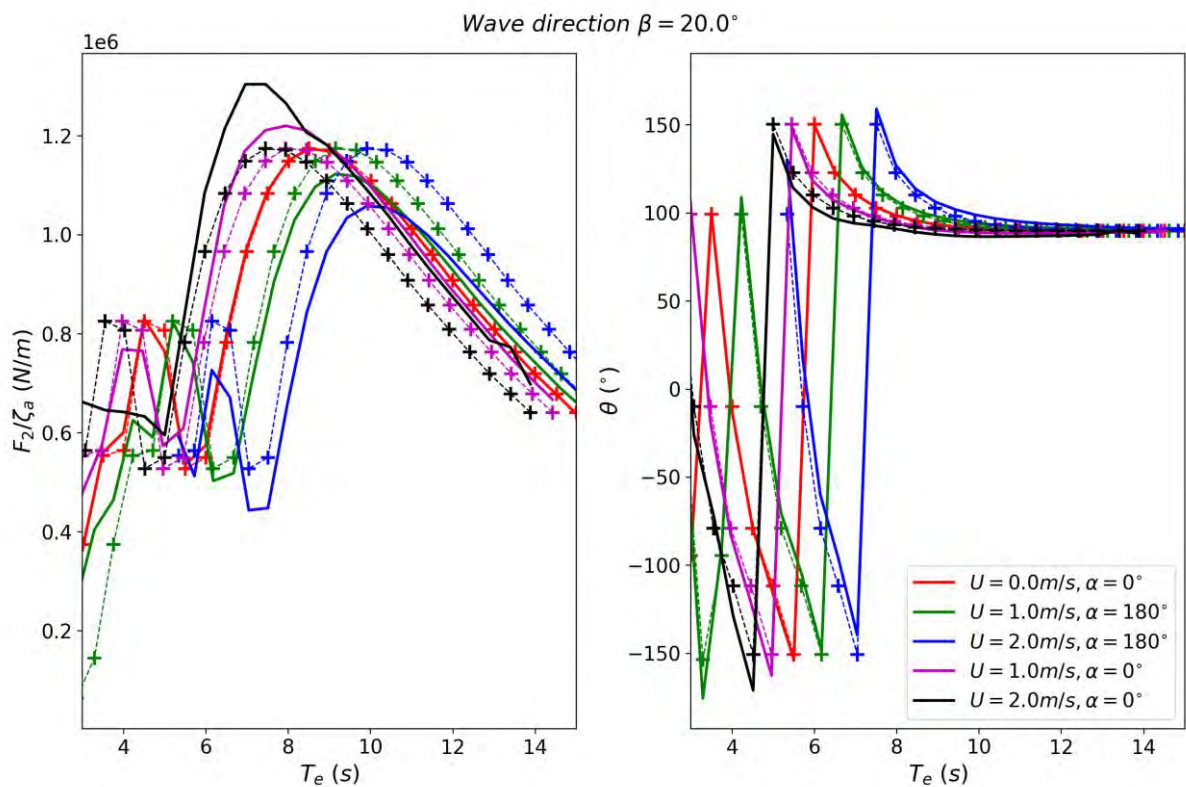

Figure 3-7 Wave excitation loads in sway, wave direction 20°. Wadam results plotted as a function of encounter period T_e are dashed with (+) markers.
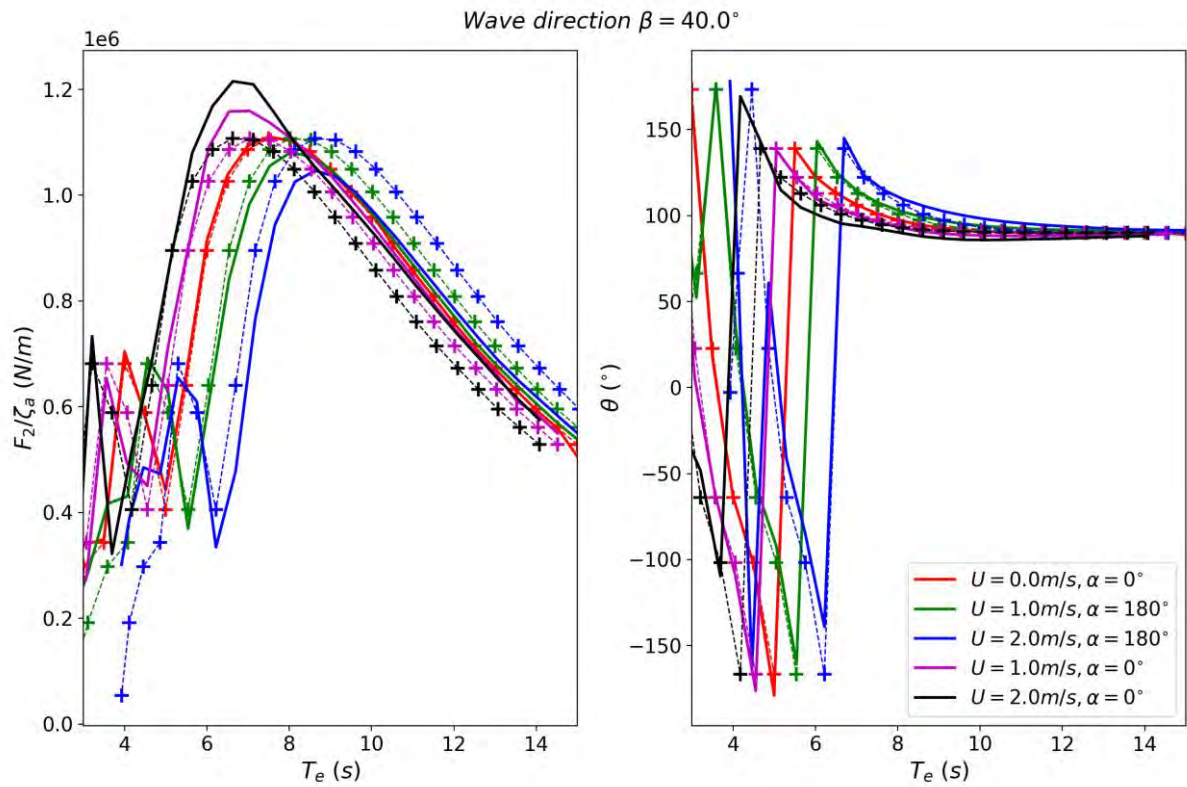
Figure 3-8 Wave excitation loads in sway, wave direction $40°$. *Wadam results plotted as a function of encounter period* T_e *are dashed with (+) markers.*
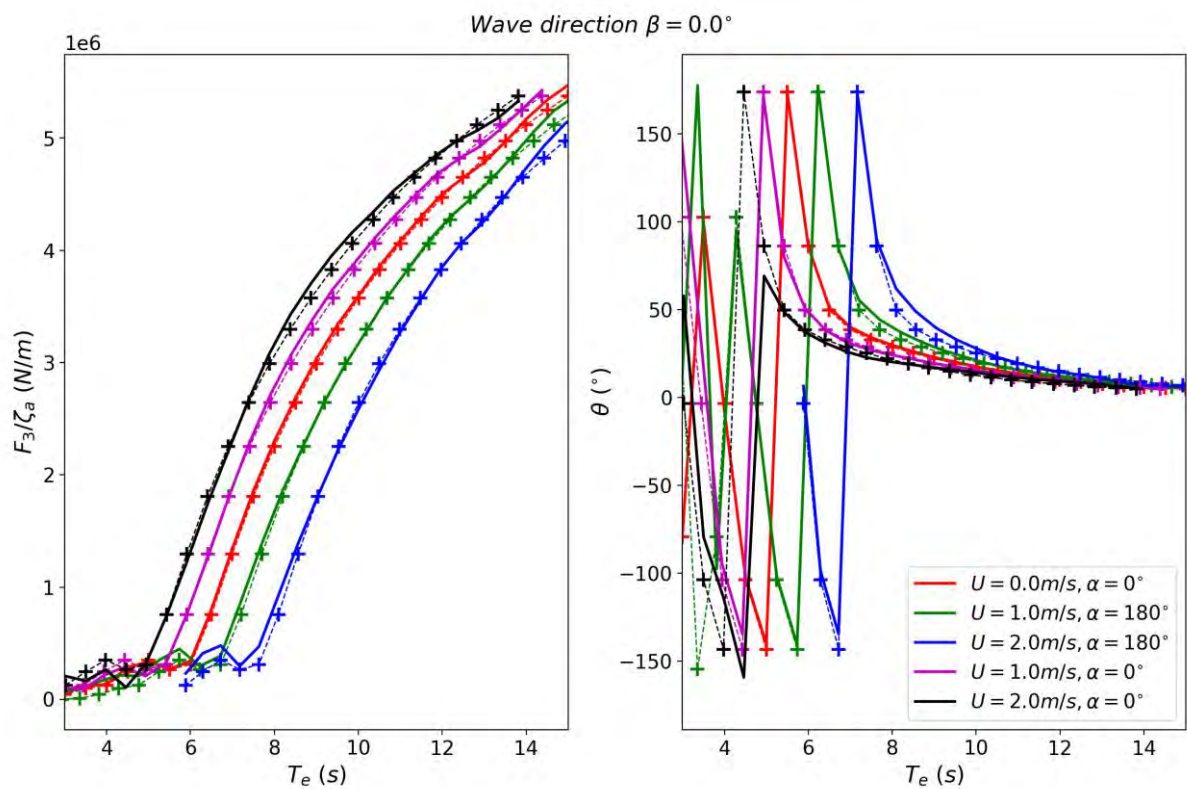
Figure 3-9 Wave excitation loads in heave, wave direction $0°$. *Wadam results plotted as a function of encounter period* T_e *are dashed with (+) markers.*
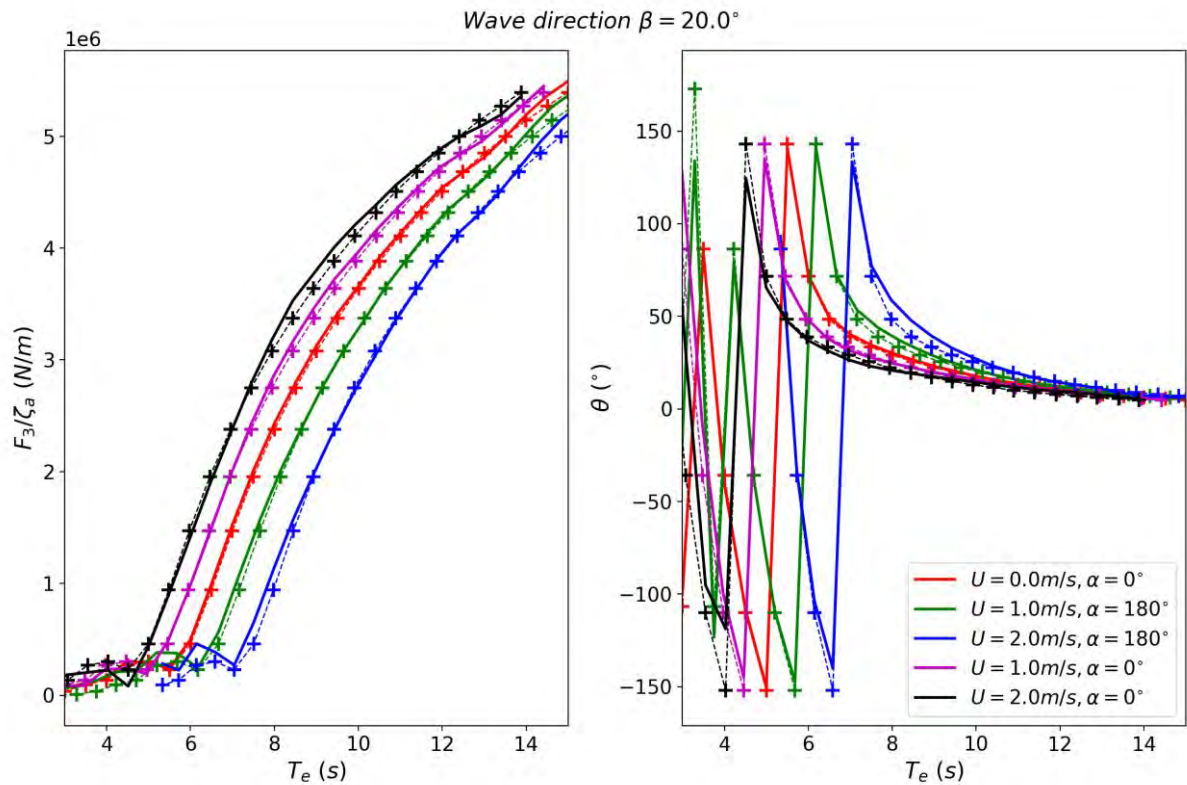
Figure 3-10 Wave excitation loads in heave, wave direction 20°. Wadam results plotted as a function of encounter period T_e are dashed with (+) markers.
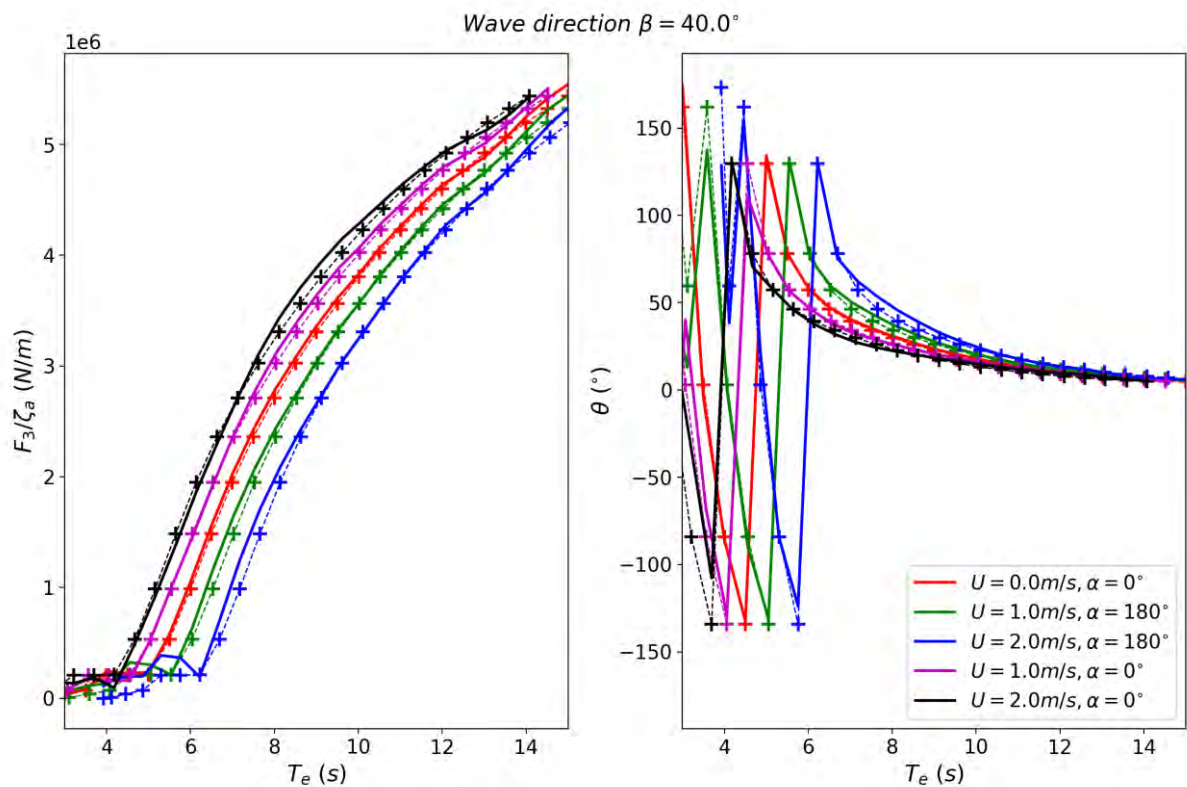
Figure 3-11 Wave excitation loads in sway, wave direction 40°. Wadam results plotted as a function of encounter period T_e are dashed with (+) markers.
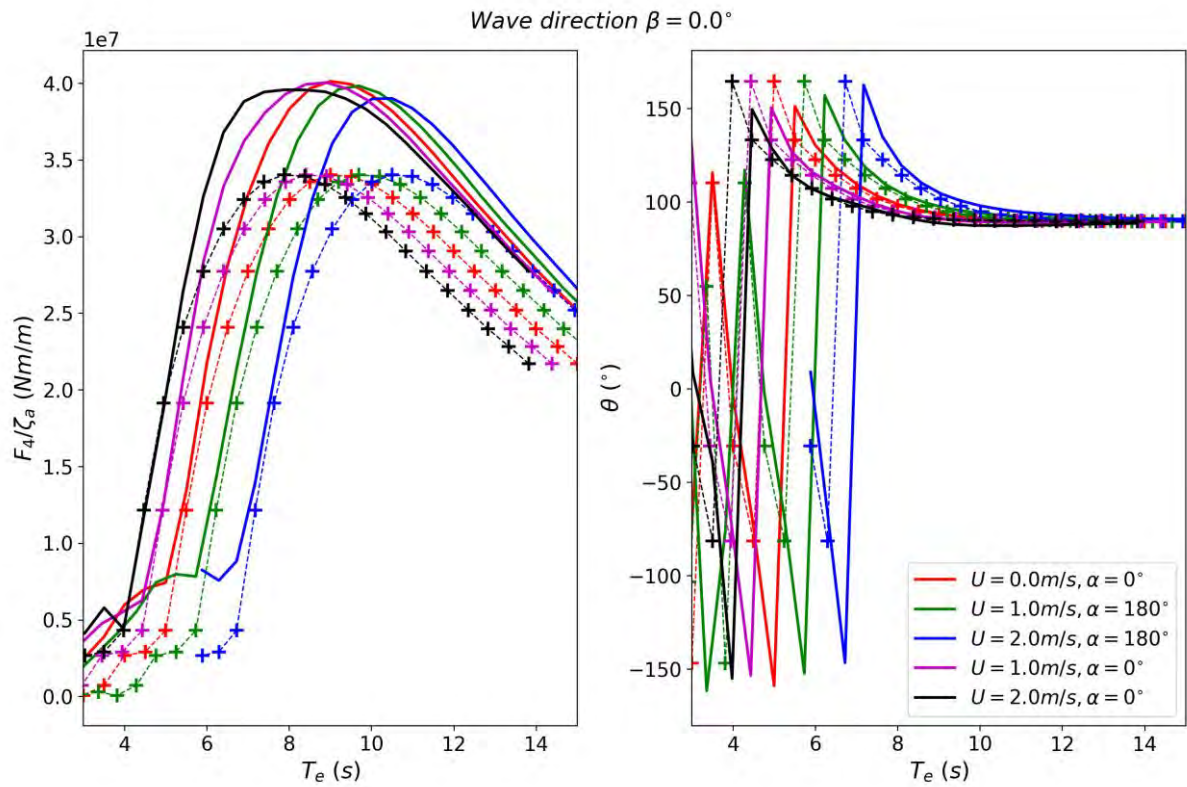
Figure 3-12 Wave excitation loads in roll, wave direction 0°*. Wadam results plotted as a function of encounter period T_e are dashed with (+) markers.*
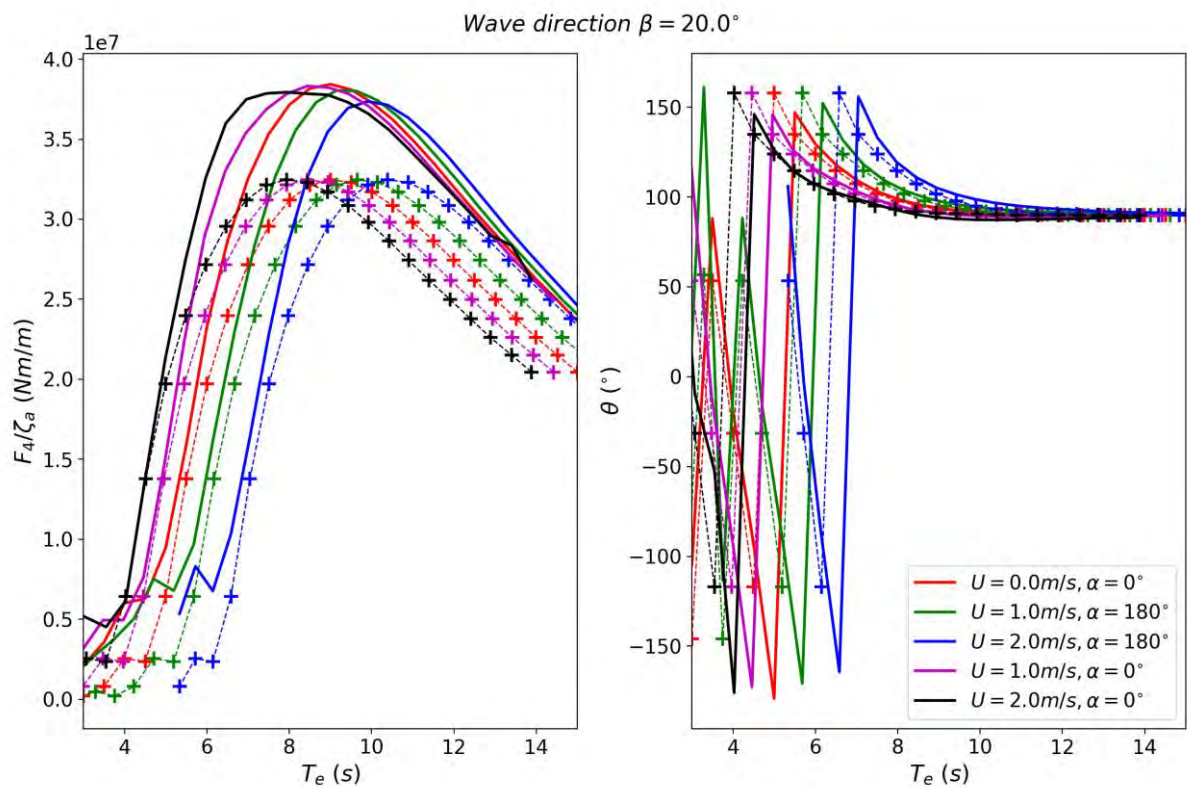
Figure 3-13 Wave excitation loads in roll, wave direction 20°*. Wadam results plotted as a function of encounter period T_e are dashed with (+) markers.*
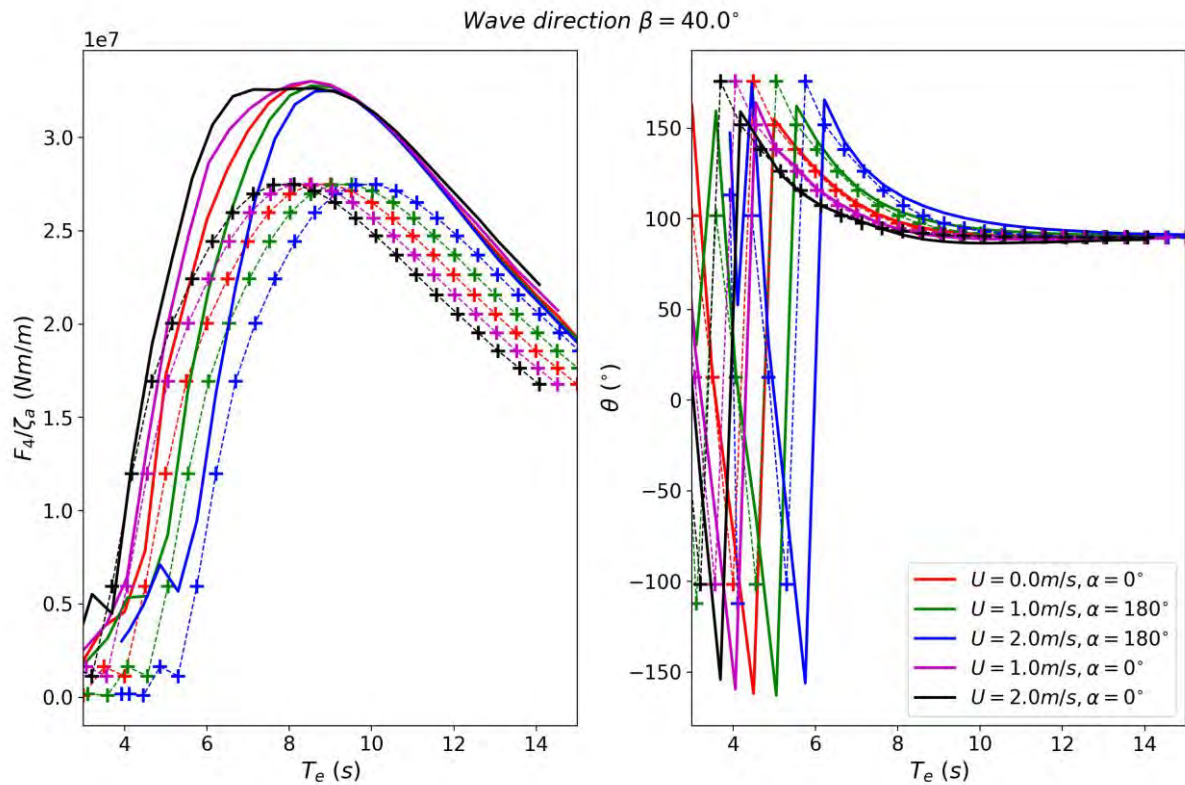
Figure 3-14 Wave excitation loads in roll, wave direction $40°$. Wadam results plotted as a function of encounter period T_e are dashed with (+) markers.

3.5 Results radiation

This section presents results for the wave-current interaction for the radiation loads for a current speed of 1.5 m/s.

Note that the encounter frequency is equal to the intrinsic frequency (i.e. not equal to the encounter frequency) for the radiation problem.

In addition to the hydrodynamic coefficients given in figures below for the main diagonal, new coupling terms between motions appear that do not exist for the zero-current case.
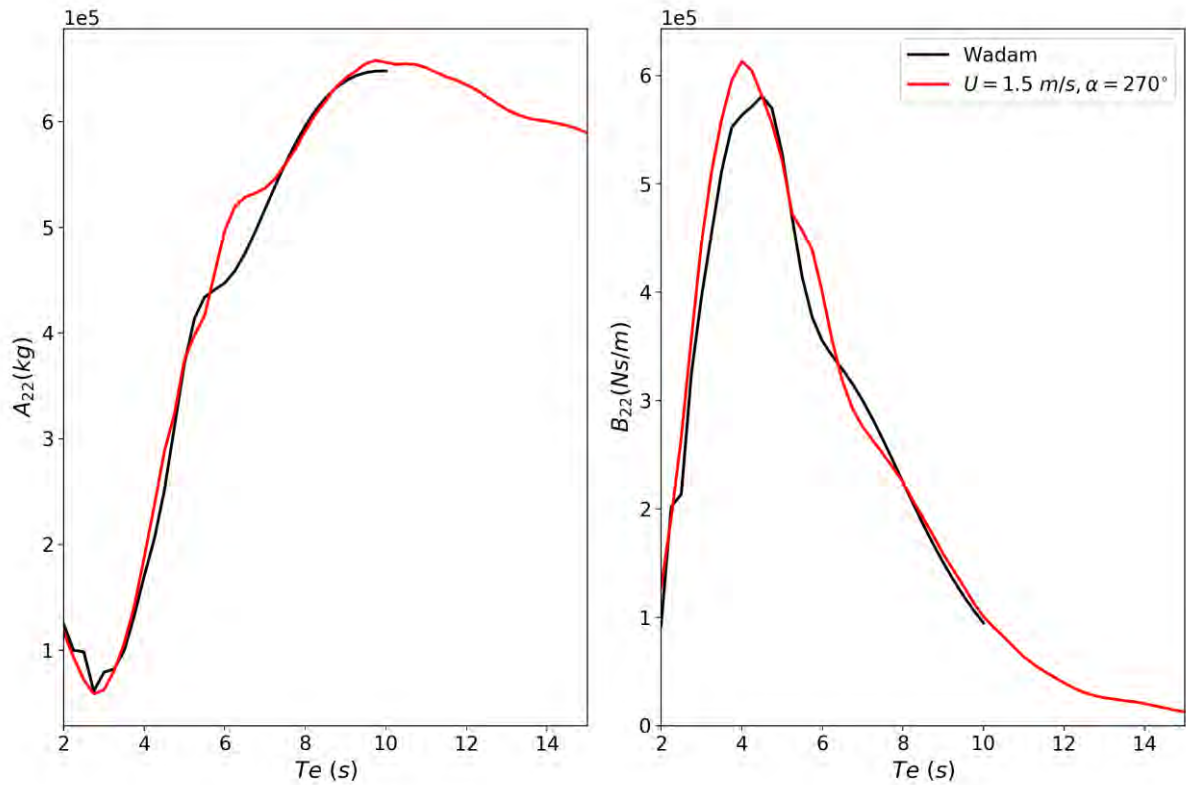
Figure 3-15 Added mass (left) and potential flow damping (right) for the sway motion for 1.5m/s current from 270 degrees. WADAM represents the zero-current case.
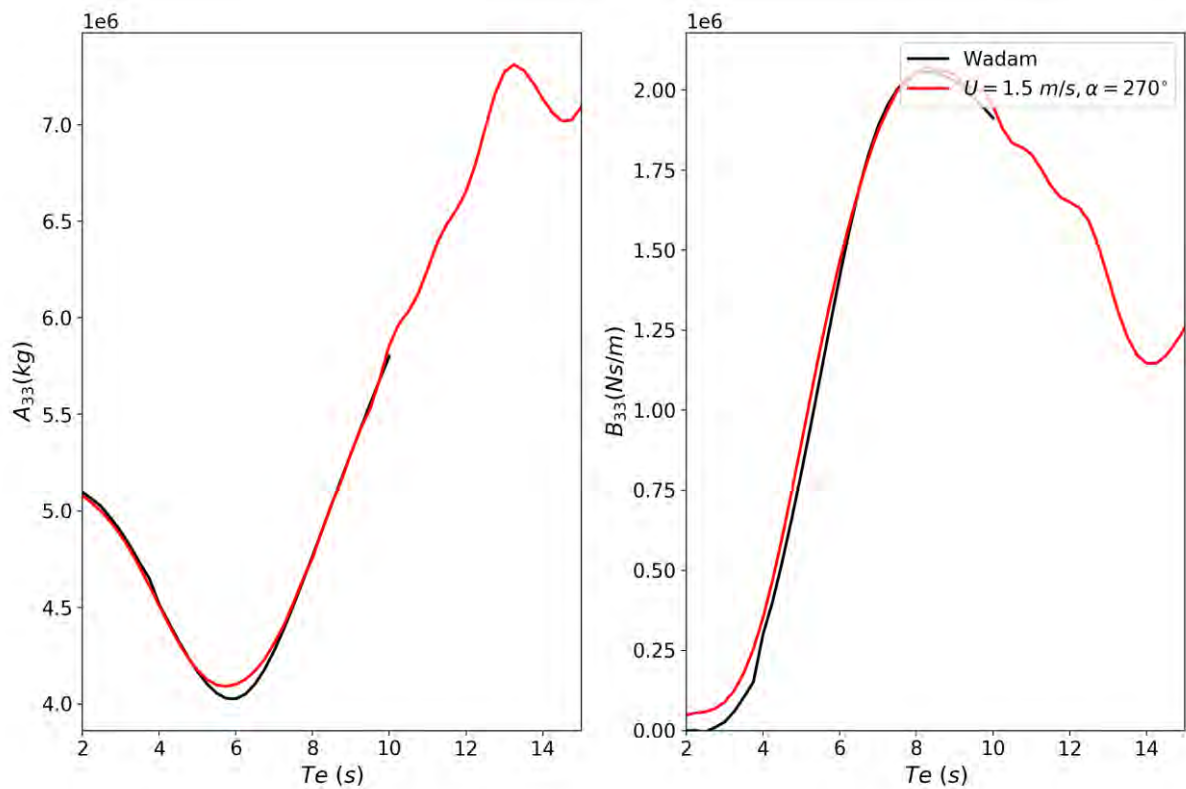
Figure 3-16 Added mass (left) and potential flow damping (right) for the heave motion for 1.5m/s current from 270 degrees. WADAM represents the zero-current case.
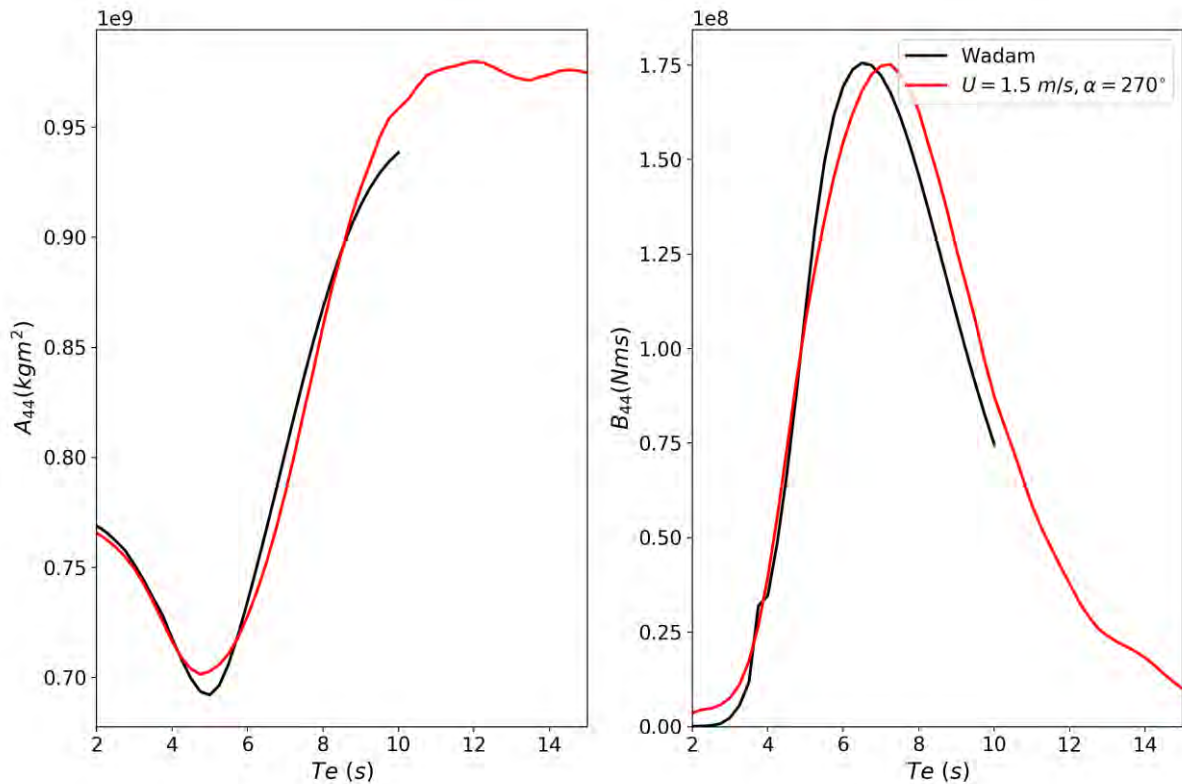
Figure 3-17 Added mass (left) and potential flow damping (right) for the roll motion for 1.5m/s current from 270 degrees. WADAM represents the zero-current case.

3.6   Global analysis results

Two different inputs in the global analysis must be changed in order to study the wave-current interaction problem. First, the frequency dependent added mass, damping and wave excitation force coefficient. Secondary, the input wave spectra must be changed to account for the frequency of encounter, since they are in the metocean design basis [11] given without current present. A simplified approach has been chosen here, where analysis of long-crested waves incoming normal to the K13_06 bridge is possible. Other effects are also turned off, resulting in a study where it is purely the effect of wave-current interaction that influences the results. The study is performed in the frequency domain. The results below are for a current velocity of 1.5 m/s in either following or opposing direction to the waves. The realism of the opposing current is questionable, since the extreme currents in Bjørnafjorden may be wind driven. However, this needs to be further investigated and clarified as part of the metocean design basis.

The result in Figure 3-18 shows a significant increase in the strong axis moment for waves and current opposing each other. Waves and current in opposing directions give waves with lower frequency of encounter, resulting in excitation of modes with higher periods.

The vertical motion is increased in opposing current as seen in Figure 3-19. For the weak axis moment, it is difficult to conclude from long-crested beam sea. Further studies with other directions and short-crested seas are needed.

As seen in Figure 3-20 and Figure 3-21 the torsional moment and rotational motion of the bridge are also significantly higher than the zero-current velocity with waves and current in opposing direction.
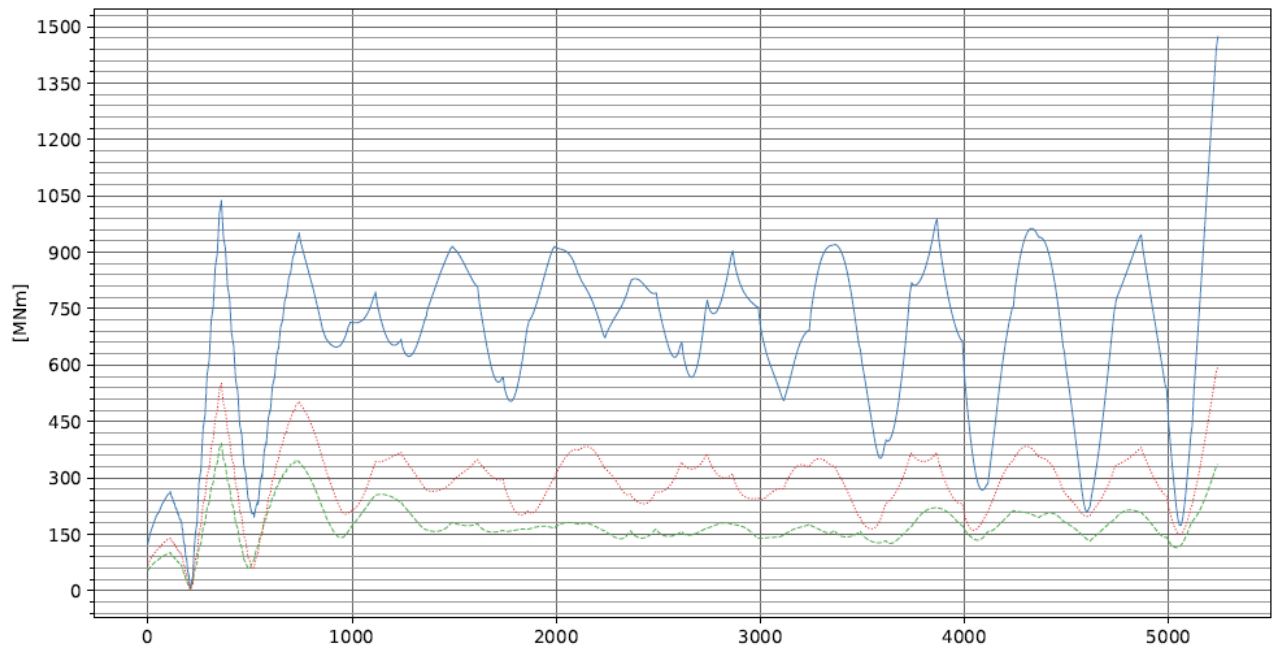
Figure 3-18 Comparison of the strong axis moment for long crested 100-y waves normal to the bridge (Hs=2.1m and Tp=5.5s). In blue is waves and current in opposite directions, red is without current and green is for waves and current in same direction.
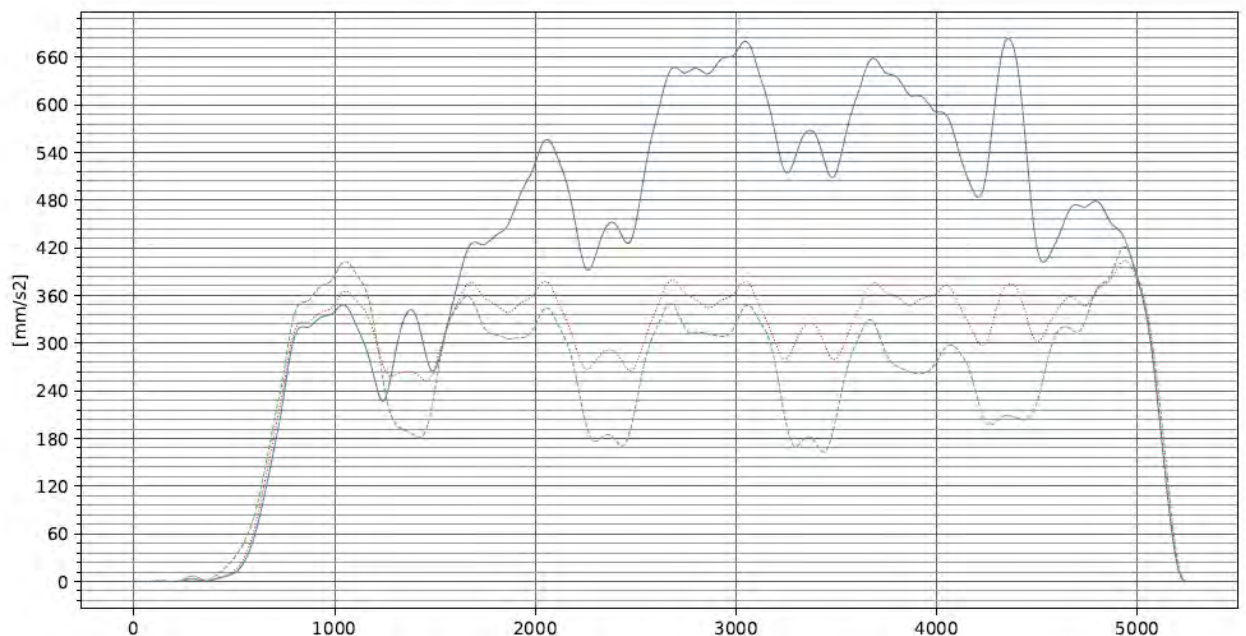

*Figure 3-19 Comparison of the vertical acceleration for long crested 100-y waves normal to the bridge (Hs=2.1m and Tp=5.5s). In blue is waves and current in opposite directions, red is without current and green is for waves and current in same direction.*

Torsional moment
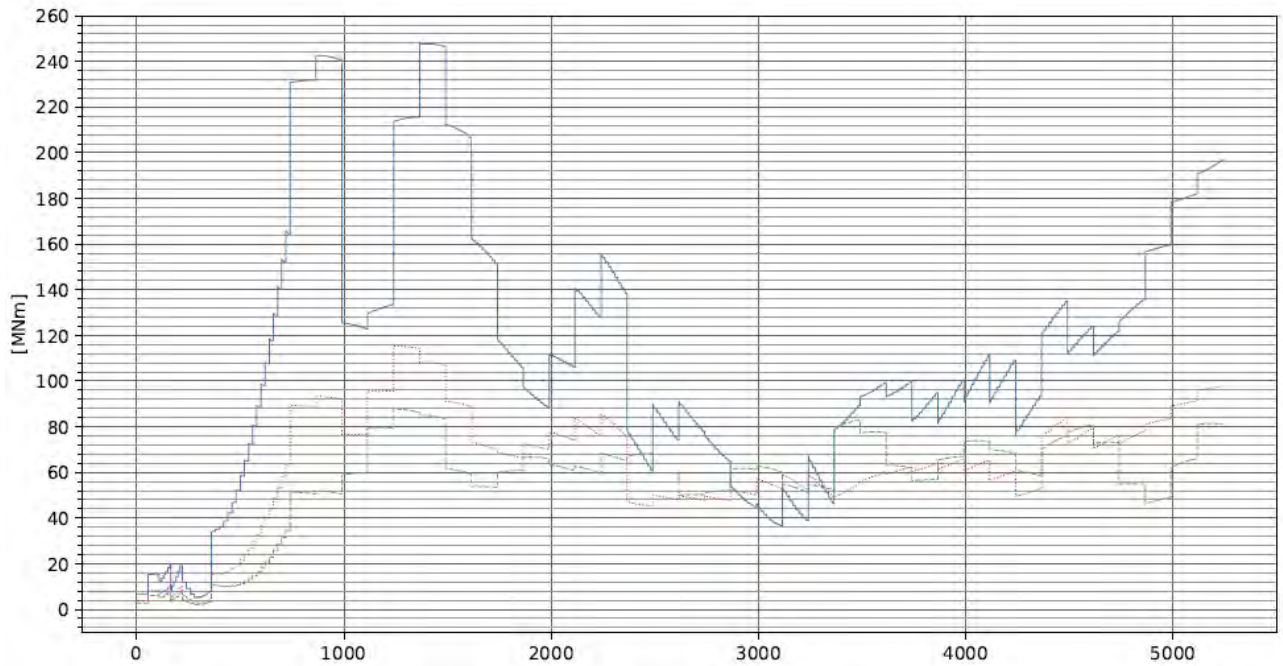
Figure 3-20 Comparison of the torsional moment for long crested 100-y waves normal to the bridge (Hs=2.1m and Tp=5.5s). In blue is waves and current in opposite directions, red is without current and green is for waves and current in same direction.

Rotation about bridge axis
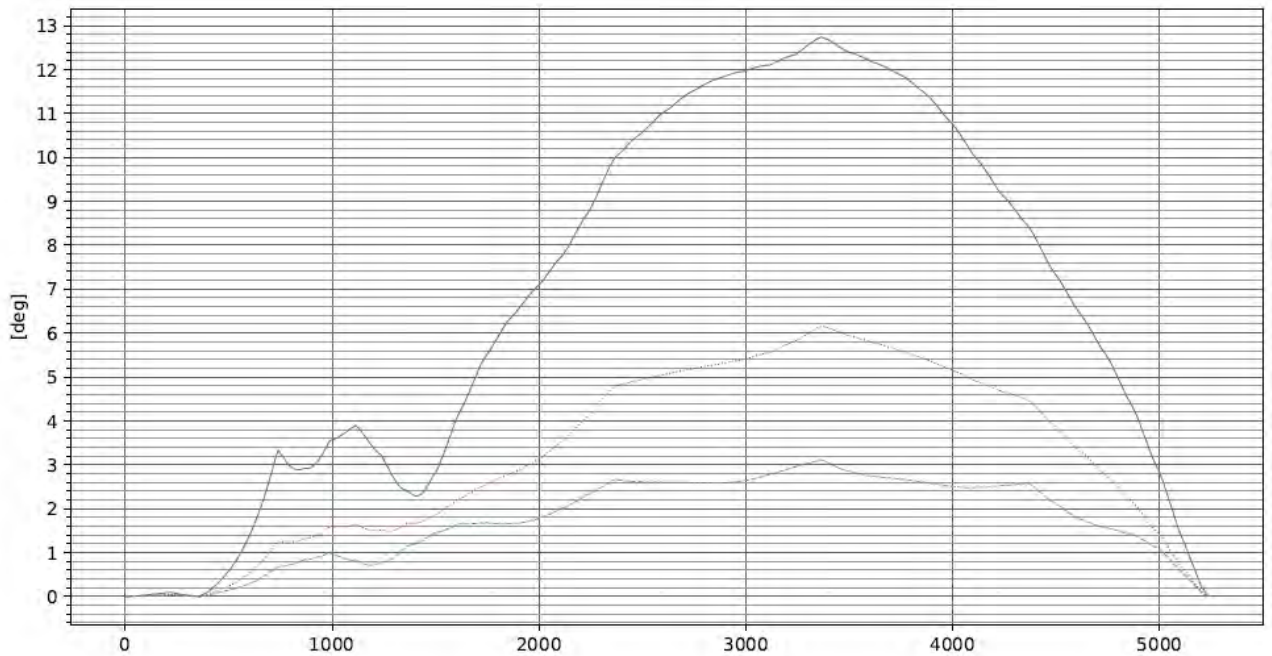
Figure 3-21 Comparison of the rotation about the bridge axis for long crested 100-y waves normal to the bridge (Hs=2.1m and Tp=5.5s). In blue is waves and current in opposite directions, red is without current and green is for waves and current in same direction.

3.7   Uncertainties and limitations

The wave-current interaction studies presented herein are based on the following limitations:

-   Metocean data in [11] for the wind waves are interpreted as valid without any current present.

    o   Input wave spectrums to the global analysis have been frequency shifted to account for the presence of current. It is assured that the wave components have the same amplitudes after the frequency shift (i.e. the energy is conserved).

-   Long-crested 100-year wind wave (Hs=2.1m and Tp=5.5s) normal to the bridge.

-   Uniform current of 1.5 m/s across the fjord opposing or following the waves

    o   Spatial variation across the fjord is not considered

    o   Extreme currents may be wind driven, the realism of an extreme current opposing wind waves is then questionable

-   Viscous drag has not been included. This will give an additional static contribution to the response, but also increase the damping in the cases with current compared to the non-current case.

-   Frequency domain OrcaFlex calculations

Based on the preliminary results the consequence on the bridge response may be significant. A simplified estimate gives an increase in the total stresses in the order of 20%, which for some areas on the bridge will be dimensioning, see Figure 3-22. However, the study is still somewhat immature and further work is needed to fully establish the consequence and realism of the preliminary results.
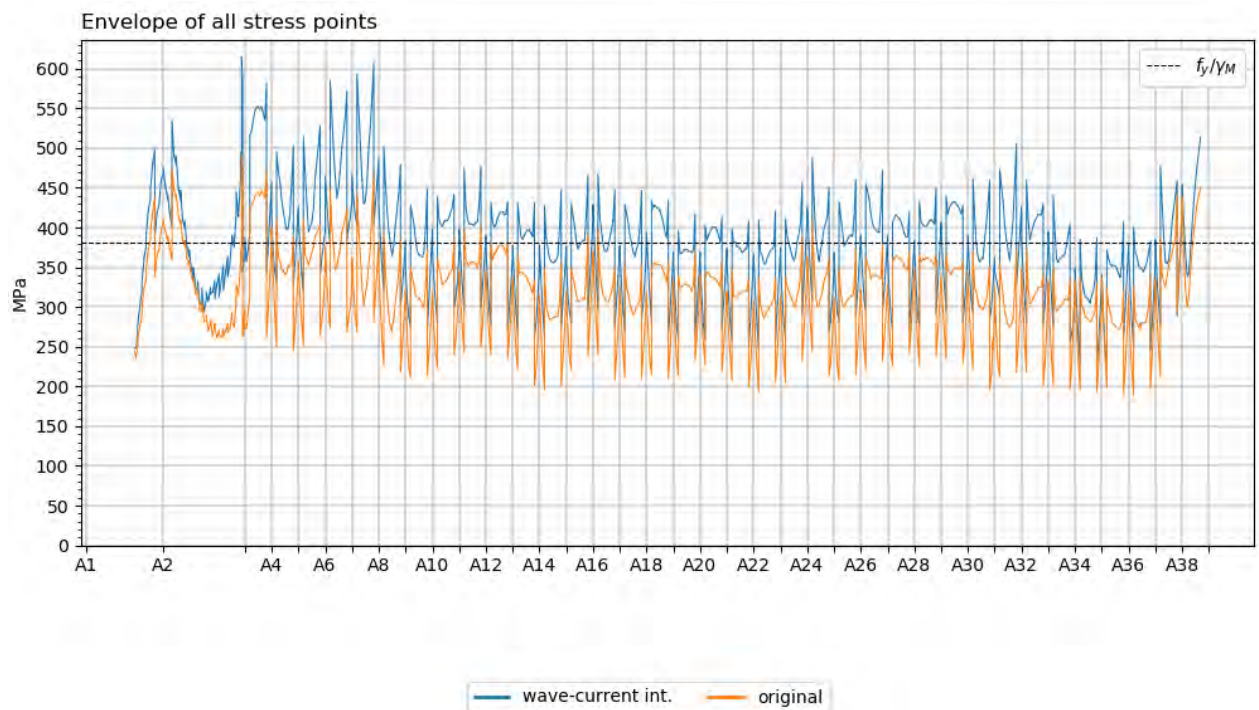
Figure 3-22 Simplified estimate on the consequence on the resulting stresses on K13_06 for ULS3, where the original strong axis and torsional moments from wind sea are multiplied by a factor 2.

3.8   Summary of wave-current interaction

The comparison between Wasim and Wadam analyses showed that wave-current interactions may have a significant effect on wave excitation loads beyond a pure frequency (Doppler) shift. The effect was more significant for sway and roll than for heave. The effect on added mass and damping was much less pronounced. Importing the Wasim transfer functions into OrcaFlex revealed an increase in global responses such as the strong axis moment. The effect of wave-current interactions is more severe for K13 than for K12. The analysis is however done only with a current speed of 1.5 m/s, assumed uniform over the span of the bridge, and with current either aligned with or opposite of the wave direction. In order to have a better understanding of the significance of wave-current interaction effects, more detailed metocean data is required. Information about the instantaneous spatial variation of current across the fjord as well as the joint distribution of wave and current directions is needed. In general, it is found that the wave-current interaction effects are more significant for the Bjørnafjorden bridge than for typical offshore projects, since the waves are both shorter and lower compared to the current velocity than in design sea states offshore. It is also a matter of fact that the global response of the bridge is sensitive to wave-current interaction effects, largely because different modes can be triggered depending on the encounter frequency.

One of the principles for the pontoon design have been to have a cancellation in sway excitation for at the highest wave period for the 100-year wind wave. This has been achieved by having the length of the pontoon close to the 1.5 times the critical wave length. A small shift in the frequency of encounter due to current can therefore lead to a large change in the sway excitation loads on the pontoon, see Figure 3-6 - Figure 3-8. The global analysis results with long-crested waves ($H_s = 2.1\ m$ and $T_p = 5.5\ s$) normal to the bridge with an opposing current of 1.5 m/s show a significant increase in response. The strong axis moment is for instance increased by a factor up to 2.5. The influence of wave-current interaction on typical fatigue sea states must be investigated.

It is not possible to conclude on the importance of wave-current interaction without better environmental data with correlated wave and current. Using the current metocean design basis with worst-case assumptions (most likely unrealistic) yields an increase of 20% in the bridge girder utilization.

Since wave-current interactions have an important effect that should be accounted for in the design, it is recommended to do a further effort to reduce the uncertainty in future phases of the project. This effort should consist in 1) obtaining more accurate metocean data with respect to the joint distribution of waves and current, 2) to validate and verify the numerical model through model tests for a single pontoon and 3) to do more extensive studies on the global bridge model in OrcaFlex. The present assessment of wave-current interaction effects in OrcaFlex is done solely in frequency domain. This assumption should be verified by doing additional studies in time domain. An additional difficulty in OrcaFlex is that the wave spectrum must be modified manually in order to shift its different frequency components. This operation is not straightforward in short-crested waves, and hence only long-crested waves are considered here. Future work should investigate how to properly scale wave spectra for short-crested sea states and further assess the importance of wave-current interaction effects in short-crested versus long-crested waves.

4 Inhomogeneous wave conditions

One of the challenges in numerical modelling of the floating bridge is that environmental conditions in the fjord, for instance waves, are inhomogeneous. This can for instance be that the wave spectra changes for different points along the fjord. The global models used until now in the project have employed fully correlated short crested seas. This means that every wave component has an infinite extent with constant amplitude and phase both transverse and parallel to the wave propagation direction. Further, the correlation length of individual wave components is difficult to determine by either measurements or numerical analysis. This correlation length is dependent on several parameters and difficult to determine at the present stage of the project.

4.1 Varying wave phase

For the analysis considered here, the correlation between each pontoon is considered negligible. In principle this means that a new seed for the wave elevation is drawn at each pontoon. In OrcaFlex this is achieved by changing the phase angle on the excitation force with a separate random variable for each pontoon. This still allows the simulations to be performed in frequency domain.

To get the purest excitation of an eigenmode, in addition to having the wave frequency overlapping with the eigenmode it is also important that the form of the excitation coincides with the form of the eigenmode. In a sea state with fully correlated wave components between the pontoons, there exists a limited amount of excitation forms. However, in an inhomogeneous wave condition a much larger selection of excitation forms will exist and possibly an excitation form that will overlap more closely with the mode form. In the present study with only a small selection of different seeds, it is hard to determine if this effect is captured. In most cases the creation of an inhomogeneous sea state by the proposed method creates a wave field with an excitation form that lowers the response of the bridge. Either a larger selection of seed needs to be checked, or an inverse methodology must be developed. I.e. for every mode, find the wave pattern that gives the highest excitation. This quickly escalates to an unmanageable amount of numerical simulations.

A simplified study of varying phase between the pontoons was conducted, with three different realizations of phase difference. An example of the result is shown below, in which the response with inhomogeneous conditions was compared to the correlated short-crested seas assumption as used for the main global analysis as a relative difference in %. Figure 4-1 to Figure 4-3 shows the strong-, weak- and torsional moments respectively. A significant variation is observed when then phase variation is introduced for the various sea states that are checked, and there is a randomness to where the results increase or decrease due to the phase variation. A large variation in percentage may occur for a low sea state where two low numbers are compared, whereas a large variation in response may give a low variation in percentage for a governing sea state. The results are not weighted to assess the variation of the absolute value of response in the governing sea states, and as such inconclusive both considering FLS and ULS/ALS.
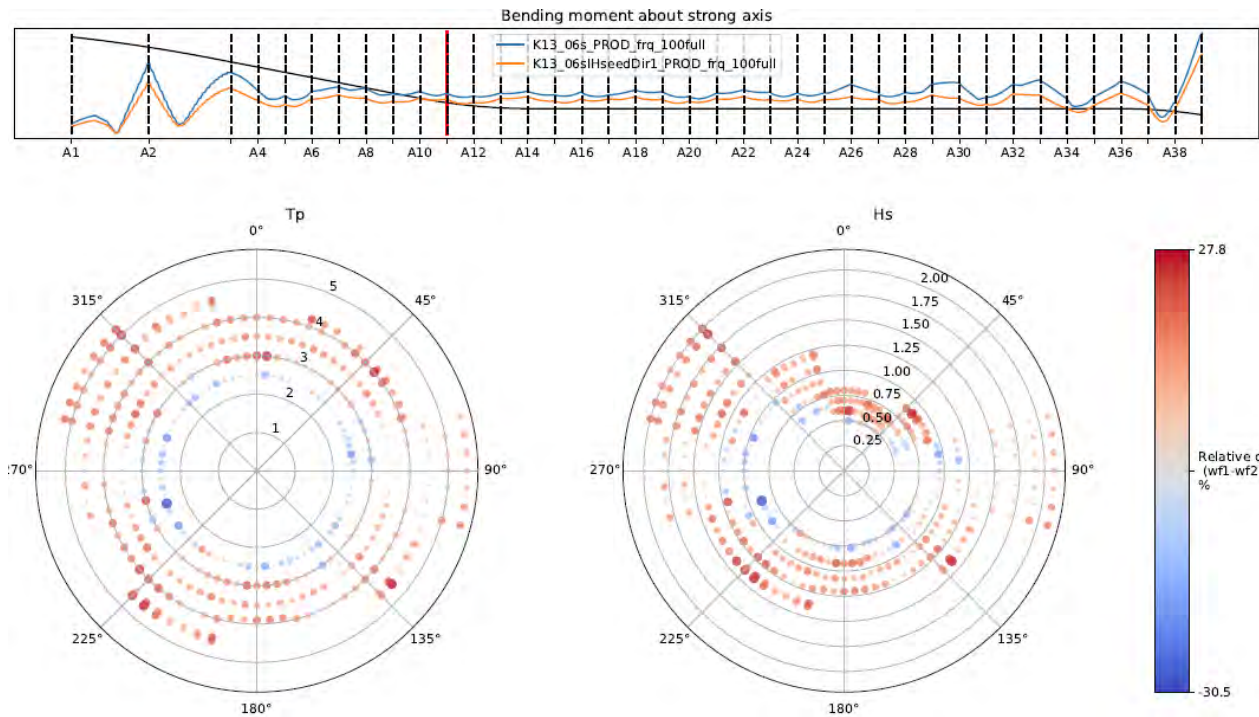
Figure 4-1 Difference of the standard deviation for strong axis moment between fully correlated sea and a single seed with inhomogeneous sea for a range of wave directions, periods and heights. Red indicates that the inhomogeneous sea state gives lower response. The picture on top shows the maximum standard deviation from all simulations along the bridge, the difference at axis 10 is illustrated here in the rose plots.
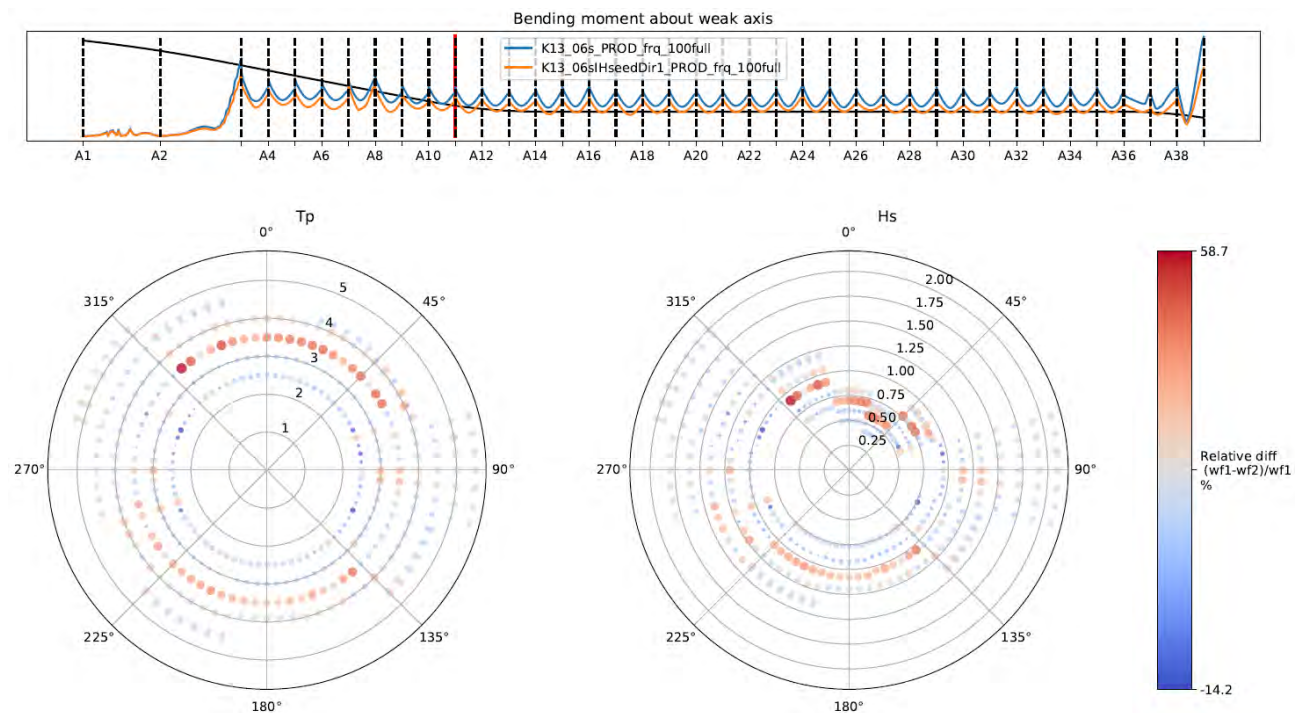

Figure 4-2 Difference of the standard deviation for weak axis moment between fully correlated sea and a single seed with inhomogeneous sea for a range of wave directions, periods and heights. Red indicates that the inhomogeneous sea state gives lower response. The picture on top shows the maximum standard deviation from all simulations along the bridge, the difference at axis 10 is illustrated here in the rose plots.
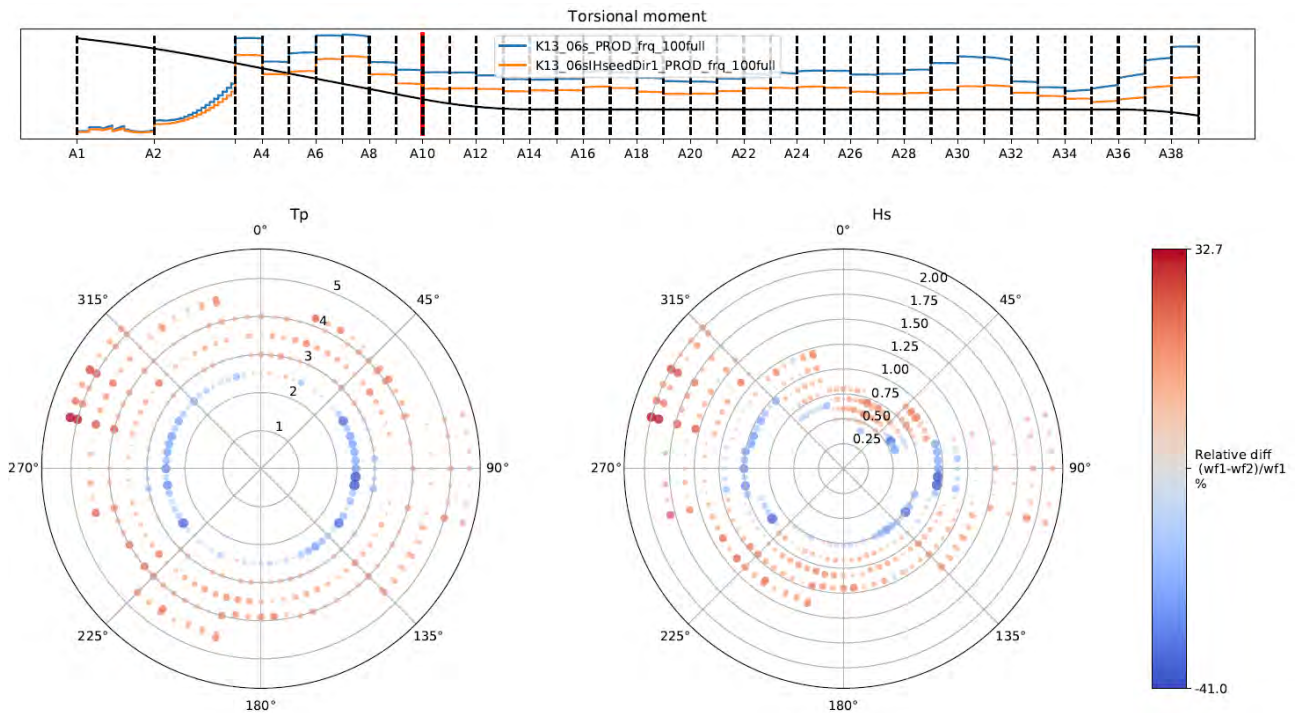
Figure 4-3 Difference of the standard deviation for torsional moment between fully correlated sea and a single seed with inhomogeneous sea for a range of wave directions, periods and heights. Red indicates that the inhomogeneous sea state gives lower response. The picture on top shows the maximum standard deviation from all simulations along the bridge, the difference at axis 10 is illustrated here in the rose plots.

4.2 Varying wave height

According to Table 7 in the metocean design basis [11] the significant wave height varies across the fjord. To sum up the table, waves coming from north/northwest gives waves that are higher towards the south and sheltered towards the north. For waves coming from south/southwest the result is opposite. Two wave screenings were conducted in which the excitation RAOs of the pontoons were modified to include the variation of significant wave height across the fjord as specified in [11]. This kind of inhomogeneity gives a clearer trend than the wave phase inhomogeneity and is as such easier to account for during design.

Figure 4-4 and Figure 4-5 give bending moments (strong axis and weak axis) for inhomogeneous wave waves heights for wind waves from the sector between 285 and 315 degrees. In the north abutment the maximum response is decreased, while minimal effect is seen in the south abutment.

Figure 4-6 and Figure 4-7 gives bending moments (strong axis and weak axis) for inhomogeneous wave waves heights for wind waves from the sector between 195 and 315 degrees. In the north abutment the maximum response is increased up to 16% at axis 38.
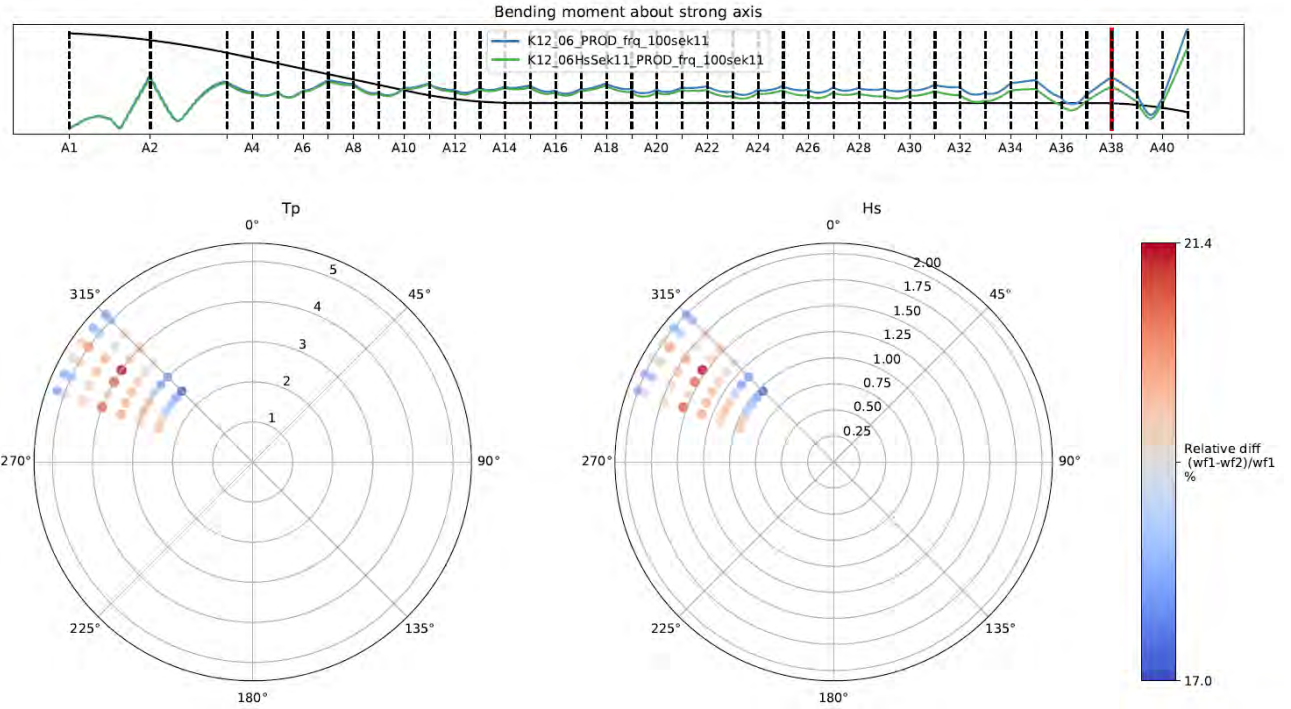
Figure 4-4 Difference of the standard deviation for strong axis moment between inhomogeneous sea with different wave height for waves from 285 and 315 degrees. Red indicates that the inhomogeneous sea state gives lower response. The picture on top shows the maximum standard deviation from all simulations along the bridge, the difference at axis 38 is illustrated here in the rose plots.
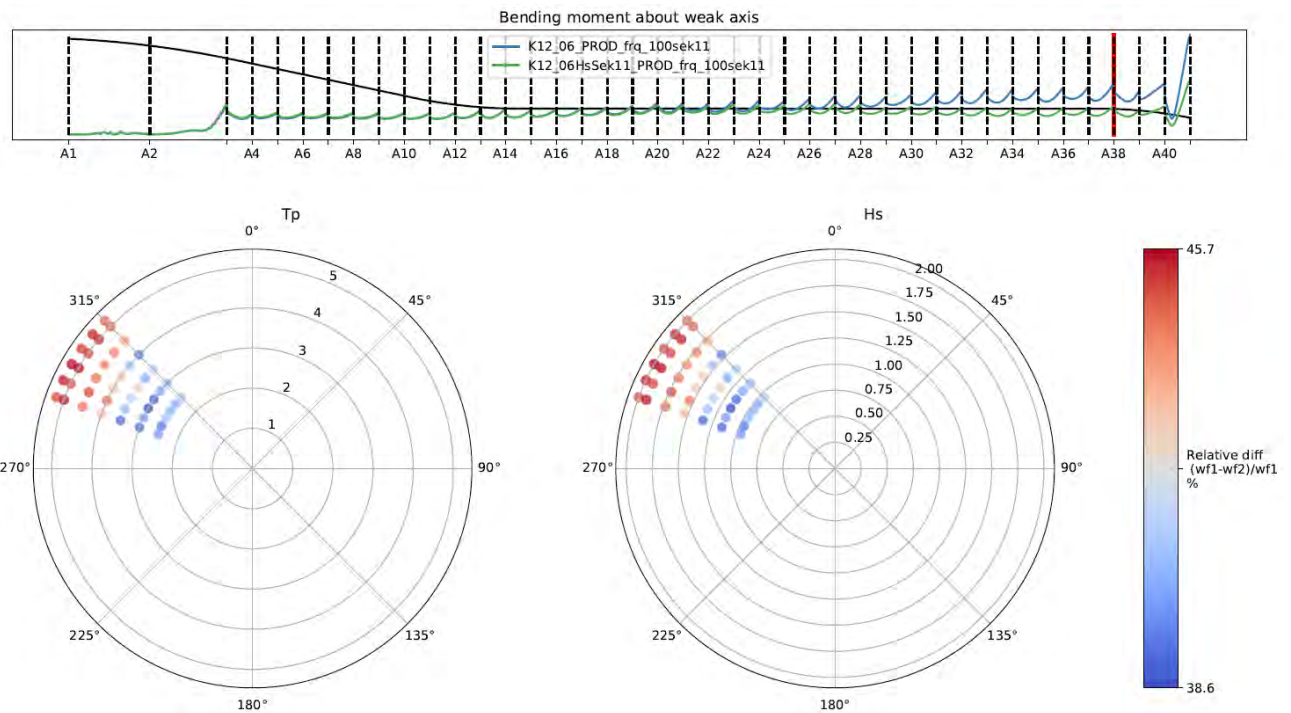

Figure 4-5 Difference of the standard deviation for weak axis moment between inhomogeneous sea with different wave height for waves from 285 and 315 degrees. Red indicates that the inhomogeneous sea state gives lower response. The picture on top shows the maximum standard deviation from all simulations along the bridge, the difference at axis 38 is illustrated here in the rose plots.
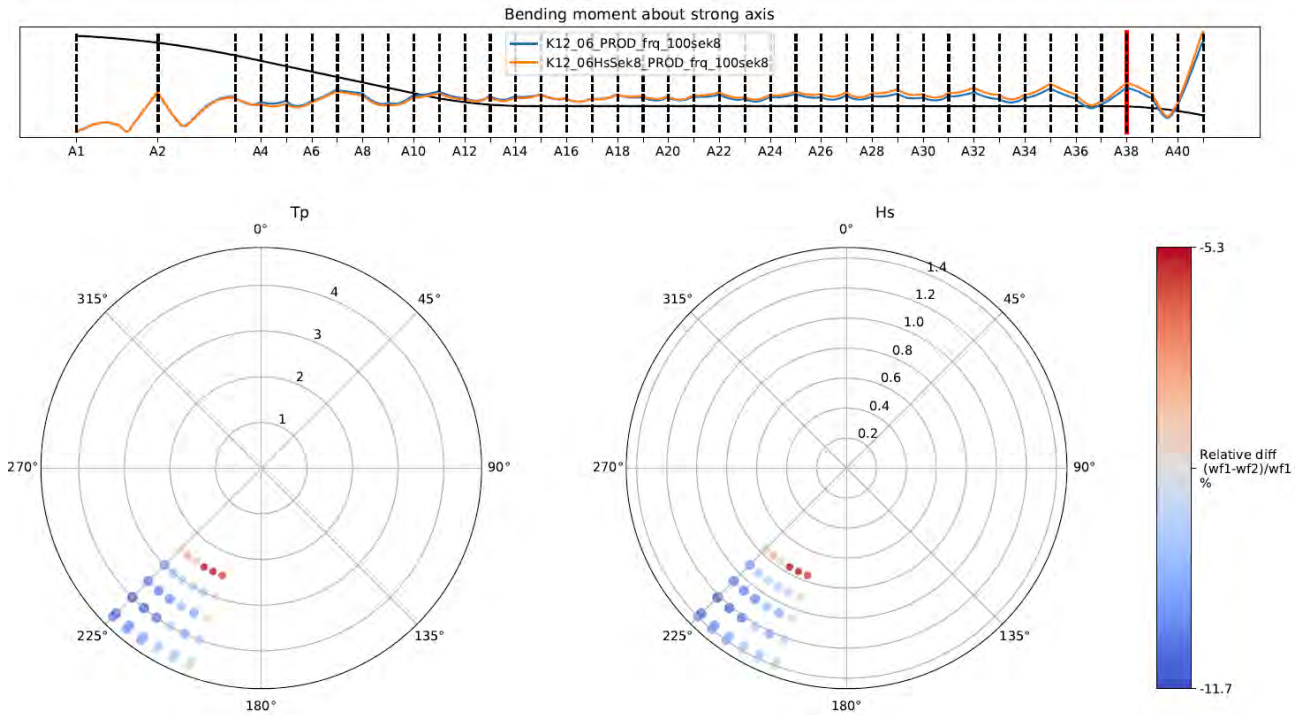
Figure 4-6 Difference of the standard deviation for strong axis moment between inhomogeneous sea with different wave height for waves from 195 and 225 degrees. Red indicates that the inhomogeneous sea state gives lower response. The picture on top shows the maximum standard deviation from all simulations along the bridge, the difference at axis 38 is illustrated here in the rose plots.
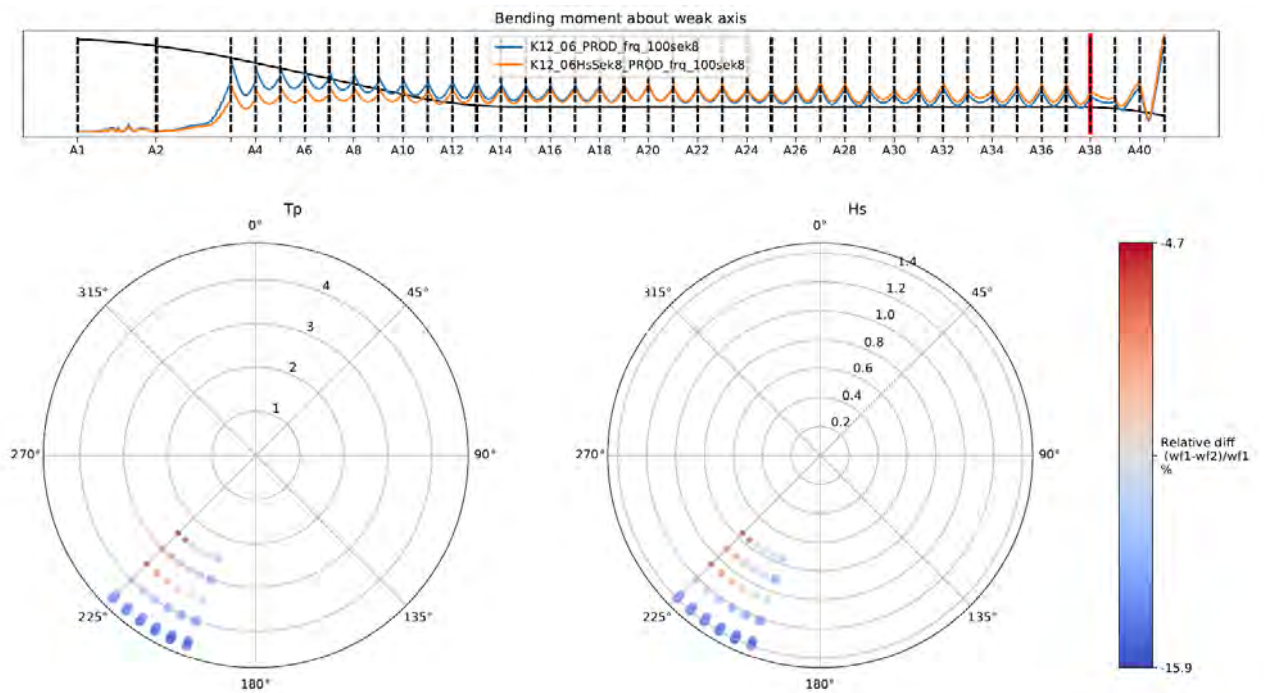
Figure 4-7 Difference of the standard deviation for weak axis moment between inhomogeneous sea with different wave height for waves from 195 and 225 degrees. Red indicates that the inhomogeneous sea state gives lower response. The picture on top shows the maximum standard deviation from all simulations along the bridge, the difference at axis 38 is illustrated here in the rose plots.

4.3   Discussion

By considering the phase angle of the wave excitation loads on individual pontoons as a random variable, the maximum bending moments about the strong and weak axes, as well as the torsional moment, are reduced over the bridge span. However, if the responses are investigated for a fixed location along the bridge for various combinations of the direction, height and period of the incident waves, the conclusion is more complex. Even though the extreme response is reduced, the response for a certain wave direction and period may very well increase as a function of inhomogeneity. This shows that one must carefully assess the effect of inhomogeneous sea states on a consequence level. As an example, increasing the response at certain critical periods may increase the risk of parametric excitation. When the wave height was varied along the bridge, an increase in maximum bending moments was observed towards the bridge ends.

The studies performed show that spatial variations of wave properties along the bridge may have a significant influence on global responses that are hard to anticipate. Moreover, it cannot be concluded in general that neglecting these effects is conservative, and the effect of inhomogeneous sea states should be further analysed. In the present phase, the study has focused on maximum loads, while the consequences for fatigue life have not been explored. Furthermore, the focus has been on the phase of wave excitation loads and varying wave height. One should also consider, and possibly analyse, spatial changes in wave periods, wave spectra, wave spreading, wave direction and current. This is a comprehensive list of parameters, and rational ways to simplify the analysis matrix and to process results statistically are required. For such assessment to be meaningful, metocean data with detail level beyond what is presently available is required.

5   Hydrodynamic interaction effects

All global response analysis which are used for input to design at this stage of the project are performed with hydrodynamic coefficients resulting from a WAMIT analysis using a single pontoon in infinite fluid. In this chapter the importance of hydrodynamic interaction between pontoons is checked.

To understand the interaction effect better a short summary of the assumptions behind linear potential flow theory is given. First, the total problem is split into two, the radiation and the diffraction potential. Here, the radiation problem is forced oscillation of the structure in each of the 6 degree of freedoms and the corresponding force in phase with the acceleration (added mass) and force in phase with velocity a (potential flow damping) is measured. Further, the second problem is the diffraction forces that are wave forces on the structure held in a fixed position.

For the hydrodynamic interaction between multiple pontoons:

-       The radiation problem is further split into forced oscillation of each pontoon independently, while all other pontoons are kept fixed. Resulting in a force on the considered pontoon, but also in a hydrodynamic force on the neighboring pontoons due hydrodynamic interaction between pontoons. In principle, this gives added mass and potential flow damping matrixes with nonzero values with dimensions [6xNBp X 6xNBp] for every wave period. Where NBp is the number of pontoons.

-       The diffraction problem is similar to the single pontoon cases, with all pontoons kept fixed. The result is a force in 6 degrees of freedom for every pontoon for every wave direction and period.

5.1   Local interaction effects

In order to initially estimate the effect of different span widths, hydrodynamic interaction analysis of 1 pontoon with two neighboring pontoons (one on each side) is checked in WAMIT. The pontoon chosen is the circtangle pontoon (53m long, 14.9m wide and 5m deep), this pontoon has a weight/displacement which is optimal for the 125m span width. In reality, pontoons for bridges with shorter span widths will also get lower displacements, similar pontoons for bridges with longer span widths will get higher displacements. See Figure 5-1 for how the heave added mass (A33) is

influenced by the span width.
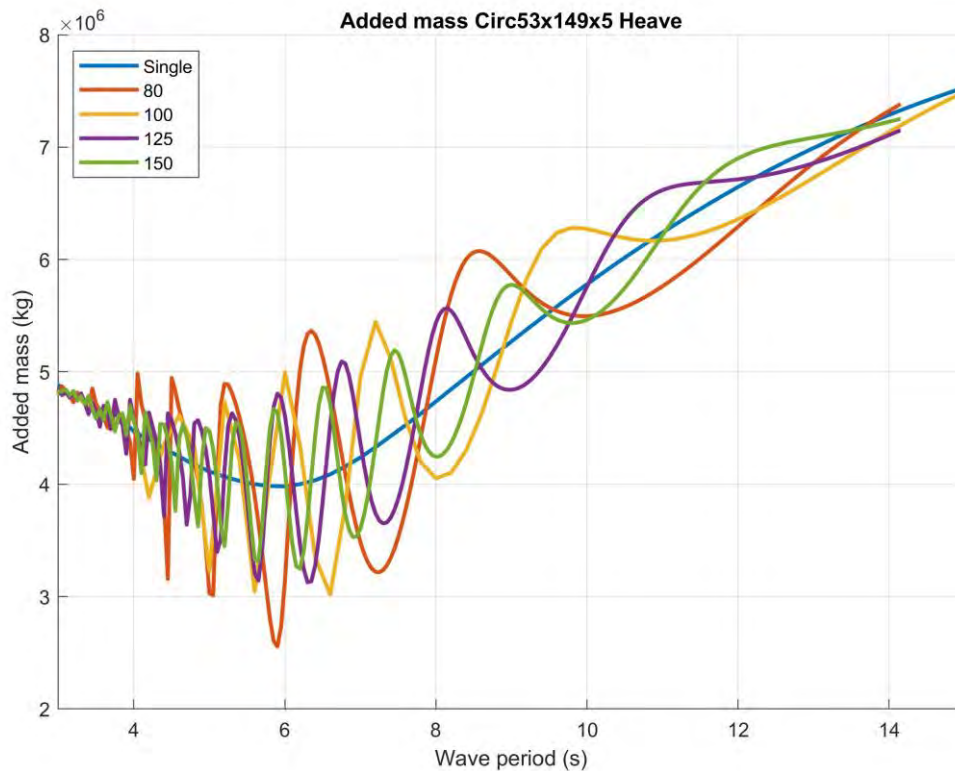
Figure 5-1 Heave added mass (A33) for different span widths

Figure 5-2 shows results (wave excitation force divided by potential flow damping) for sway motion with waves normal to the bridge for different span widths, the results represent the expected response at resonance. Similar, results for heave is seen in Figure 5-3. Different span lengths have waves with different wave period that can setup resonant sloshing type behavior between the pontoons. The result of this is seen as the different oscillating behavior for different span lengths in both Figure 5-2 and Figure 5-3.

Resonant response between bodies (piston-mode and sloshing type) can be overpredicted in potential flow theory. One alternative method to avoid this is to introduce a numerical damping lid on the free surface. However, the coefficient associated with the numerical damping lid must be calibrated towards experiments.
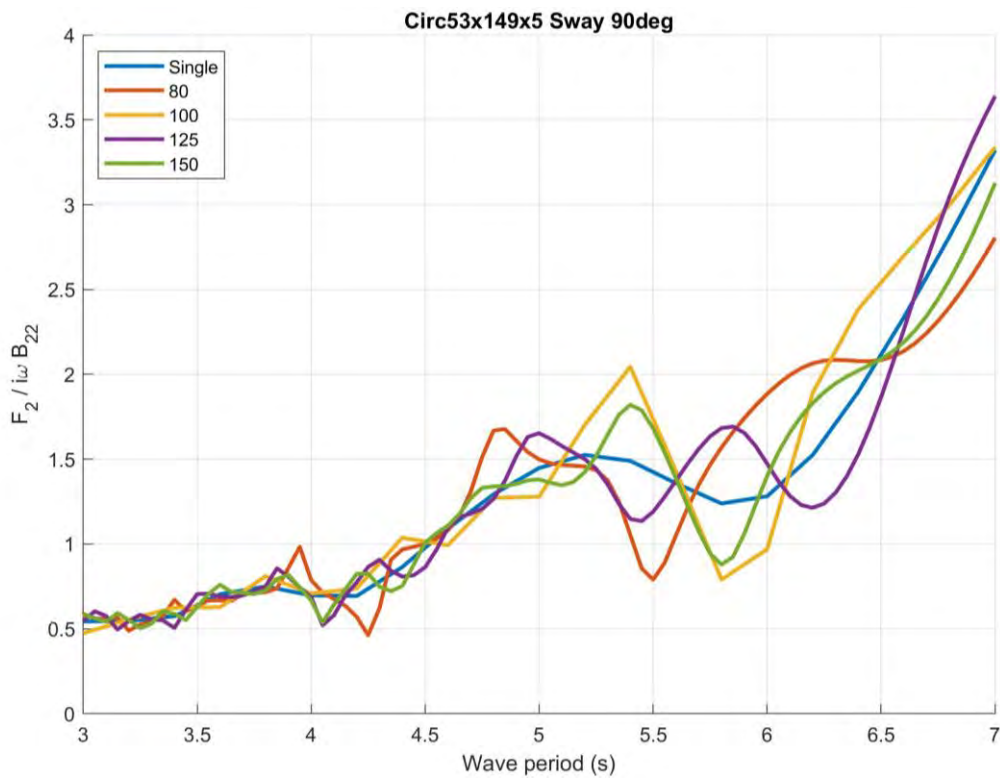
Figure 5-2 Response at resonance for sway with waves normal to the bridge (Force divided by damping) for hydrodynamic interaction for the circtangle shaped pontoon (53m long, 14.9m wide and 5m deep) for different span lengths.
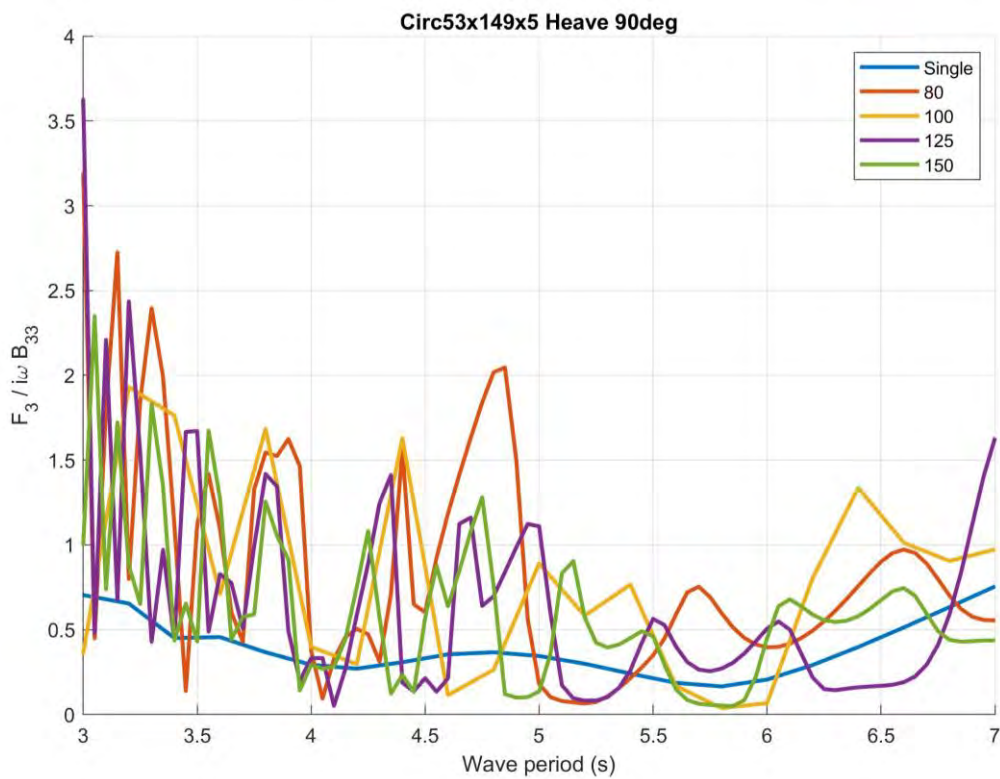
Figure 5-3 Response at resonance for heave with waves normal to the bridge (Force divided by damping) for hydrodynamic interaction for the circtangle shaped pontoon (53m long, 14.9m wide and 5m deep) for different span lengths.

Some initial WAMIT analyses were performed to establish the necessary number of pontoons to be included in the WAMIT analysis for export to the global OrcaFlex analyses.

The results presented below are again for the circtangel pontoon with dimensions 53 m · 14.9 m · 5 m, and at four different motion periods. The periods are 5 s, 6.95 s, 7.69 s and 8.95 s. The first period of 5 s was chosen out of convenience, and the two next periods were chosen based on the heave damping curve of the WAMIT run with three pontoons. The spacing between the pontoons is 125 m, and the last period of 8.95 s is chosen so that its wavelength matches the pontoon spacing.
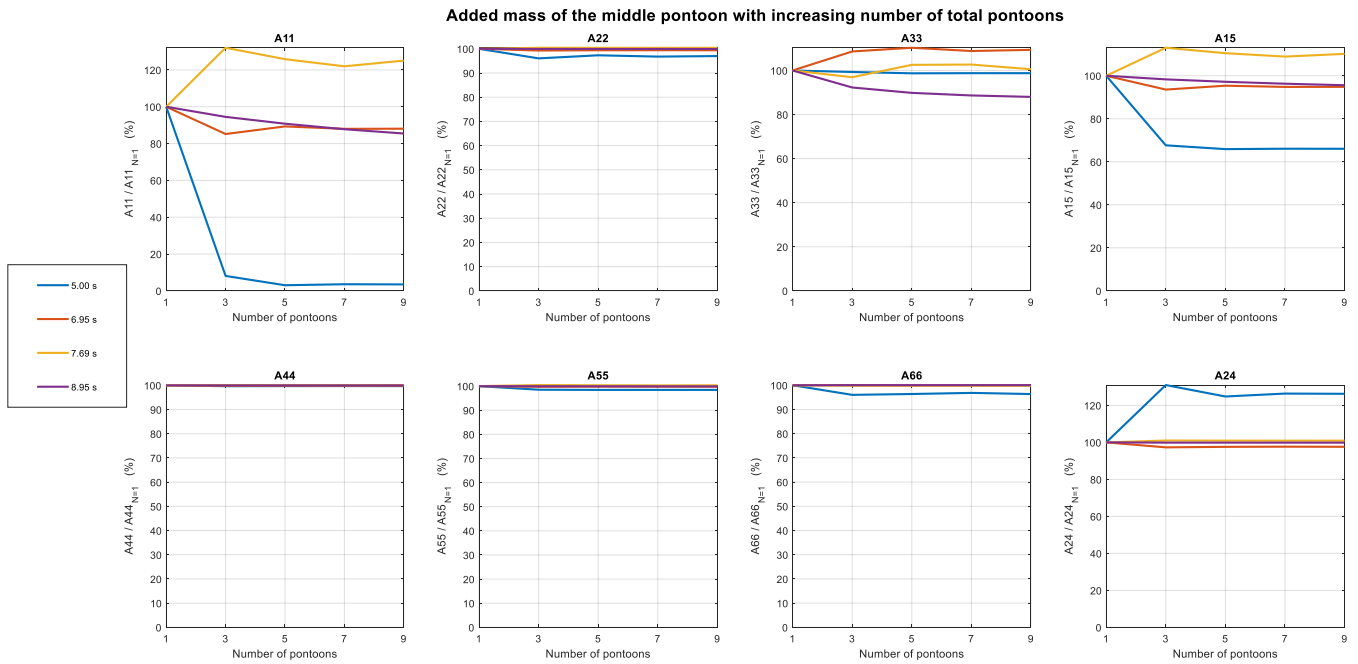
Figure 5-4 Non-dimensional added mass of the middle pontoon with increasing number of total pontoons.
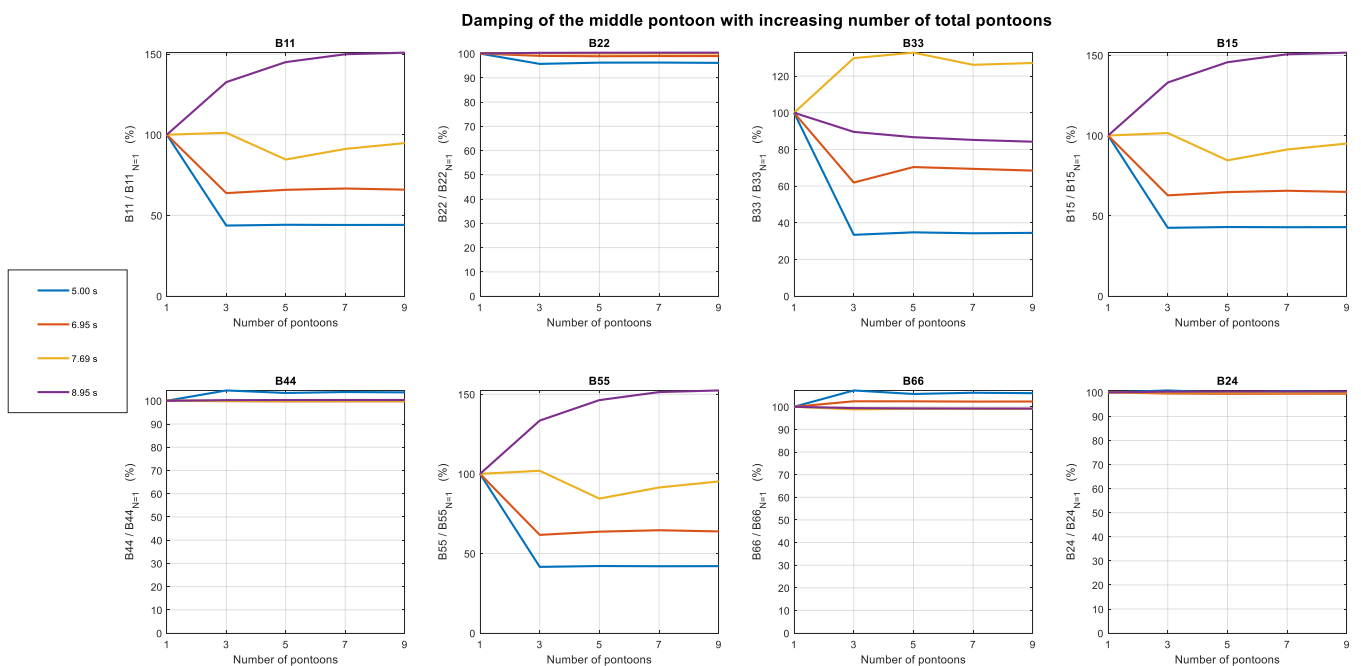
Figure 5-5 Non-dimensional damping of the middle pontoon with increasing number of total pontoons.

It is evident from Figure 5-4 and Figure 5-5 that there is a big jump in the results between one pontoon and three for certain degrees of freedom, but the difference is not as visible between three to more than three pontoons. A high period variation is also present.

The sensitivity of heave coupling between two neighbouring pontoons have been studied. The results presented in Figure 5-6 show that the coupling effects vary with increasing number of total pontoons, in addition to a strong period variation. For example, the coupled heave damping (B39) increases quite a lot with larger number of pontoons for the highest period, but not for the other periods. However, all of these coupling terms are small compared to the others closer to the matrix diagonal. It is therefore concluded that it is sufficient to proceed with three pontoons as a basis for the continuing study, especially when seen in light of Figure 5-4 and Figure 5-5.
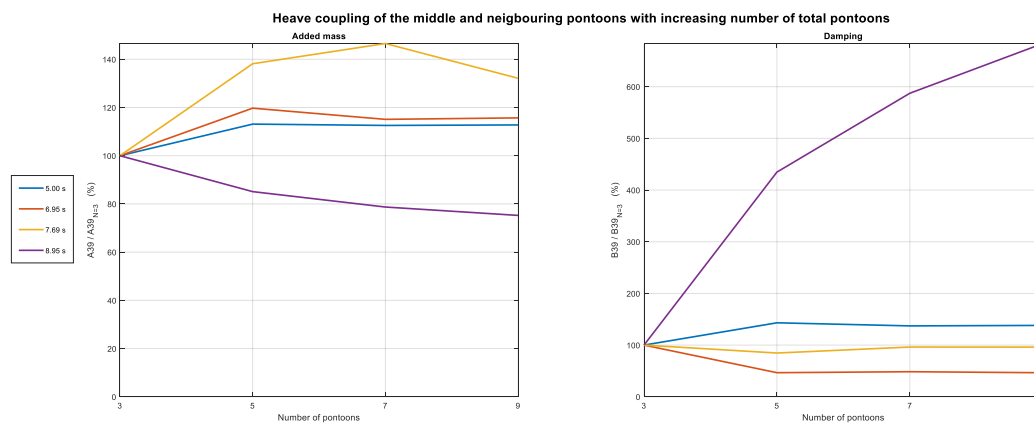
Figure 5-6 Non-dimensional added mass and damping terms for the heave coupling of the middle and neighbouring pontoons as a function of increasing number of total pontoons.

OrcaFlex allows for global simulations with hydrodynamic coefficients from a multibody analysis in WAMIT. However, this feature is at the moment only available in time domain simulations, the drawback is that then the convolution integral has to be solved to generate an impulse response function. The numerical inaccuracies associated with this approach is described further in section 5.3.

To allow for frequency domain simulations the main added mass and potential flow damping matrices from the 3 by 3 pontoon simulation in WAMIT are used to replace the single pontoon solution. Similar, the wave excitation loads are replaced by the wave excitation loads on the middle of the three pontoons from the multibody WAMIT analysis.

5.2 Frequency domain

Based on Figure 5-2 and Figure 5-3 it is difficult to conclude if hydrodynamic interaction is more severe for shorter span widths. To get a better estimate on the importance of hydrodynamic interaction for different span widths the K13_03 model is used to check the hydrodynamic interaction with 125 m and 100 m span width. The model is further simplified by having all pontoons in the bridge equal to the low bridge standard pontoon.

Here the model with 100 m span width is generated with smaller circtangle pontoons with dimensions, 53 m long, 12.8 m wide and 4.5 m deep.

A full screening of wave conditions up to the 100-year environmental contour is performed, with a wave spreading exponent of 4 and gamma parameter of 2. Due to the oscillatory type behavior seen in both Figure 5-2 and Figure 5-3 the result with hydrodynamic interaction is expected to be sensitive to the parameters of the considered wave spectrum.

The results for 125 m span width is given in Figure 5-7 for the strong axis bending moment and in Figure 5-8 for the weak axis bending moment. The results are presented as relative difference between the single pontoon results (without interaction) and the results with interaction (only main diagonal). The strong axis bending moment show small influence of hydrodynamic interaction, however, the reduction of the response when considering interaction can for some directions and periods be significant. The weak axis bending moment is more sensitive to hydrodynamic interaction, with a significant increase in the response for some wave directions. The relative difference is larger for what is typically fatigue sea states, although there are some increase in the response for the ULS sea state. The latter is not significant for design.

Comparing the response for the 125 m span width with the 100 m case, the 100 m shows higher influence of hydrodynamic interaction on the weak axis response (see Figure 5-10).

125 m
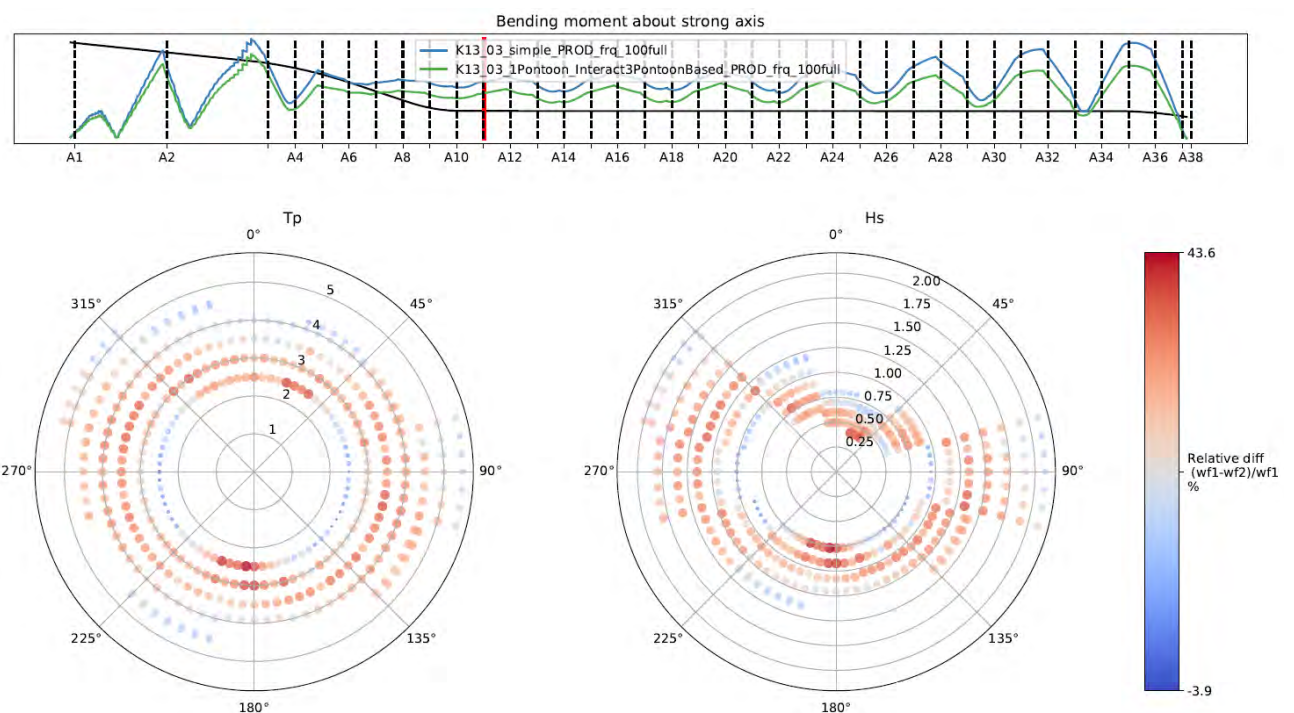
Figure 5-7 Difference in strong axis bending moment without (blue/wf1) and with (green/wf2) hydrodynamic interaction with 125m span width (K13_03)
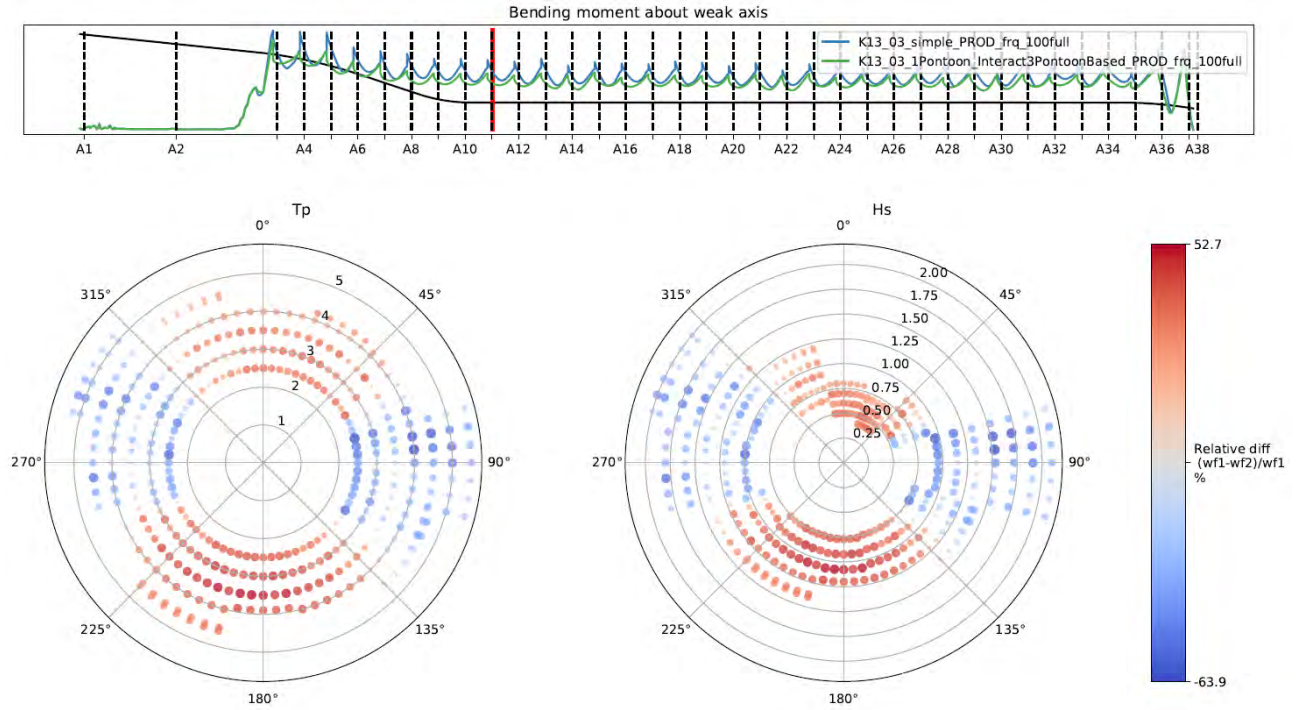
Figure 5-8 Difference in weak axis bending moment without (blue/wf1) and with (green/wf2) hydrodynamic interaction with 125m span width (K13_03)

100 m
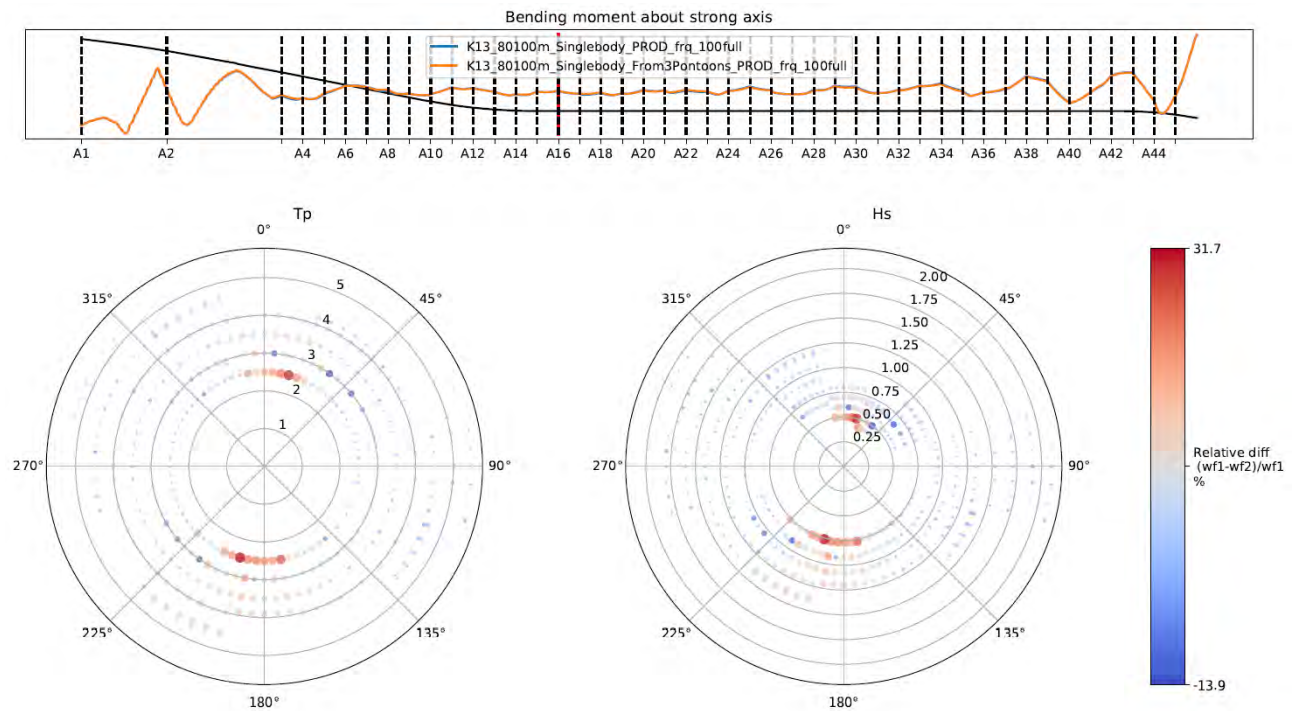
Figure 5-9 Difference in strong axis bending moment without (blue/wf1) and with (red/wf2) hydrodynamic interaction with 100m span width (K13_03)
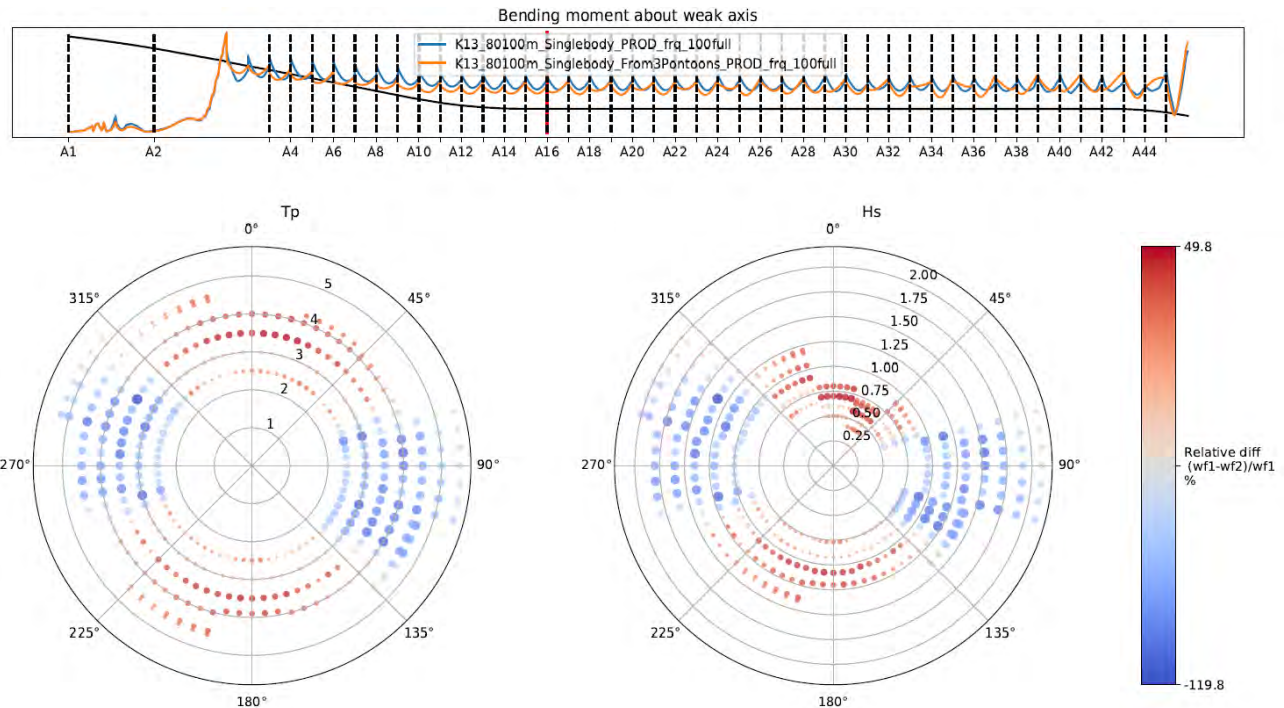
Figure 5-10 Difference in weak axis bending moment without (blue/wf1) and with (red/wf2) hydrodynamic interaction with 100m span width (K13_03)

5.3   Time domain

Attempts on performing time domain simulations in OrcaFlex with a fully coupled added mass and potential flow damping matrix for all pontoons have failed with numerical instabilities of the convolution integral (impulse response function). Several attempts on stabilizing the solutions have been attempted; increased number of calculated wave periods in WAMIT to capture the oscillations in added mass and damping due to the hydrodynamic interaction between the pontoons. Further, the available parameters in OrcaFlex to calculate the impulse response functions from the potential flow damping curves has been tried. A limiting factor in this investigation has been the extremely long simulation time necessary to perform these OrcaFlex analysis, up to a week.

These functions are supposed to die out after some time, but many of them don't, or they do so only after a very long time. The reason for this behaviour is small damping at certain frequencies where the hydrodynamic interaction effects gives standing sloshing wave between the pontoons. This gives rise to performance issues, and possibly erroneous results, which must be understood better. There is a 'cutoff' time parameter in OrcaFlex that may be tweaked to alter the computation of these functions, so it is advised to do a study of different runs with different values of this parameter to check the sensitivity and impact on the results. For higher 'cutoff' time the discretization time step becomes too large to resolve the wave frequency oscillations, as can be seen in Figure 5-16. Changing the 'cutoff' time parameter makes a huge influence on the impulse and damping functions, as can be seen in the figures below. Figure 5-16 and Figure 5-17 for example, are very different – and most of the functions die out quickly when the cutoff time is set to 200 s, although the idealised function does not behave in the same manner.

The implications of this should be investigated further. At the current stage it was not possible to conclude based on the time-domain simulations with interaction effects.

OrcaFlex 10.3a
Impulse response: Vessel type1, Draught1 surge – Vessel type1, Draught1 surge component
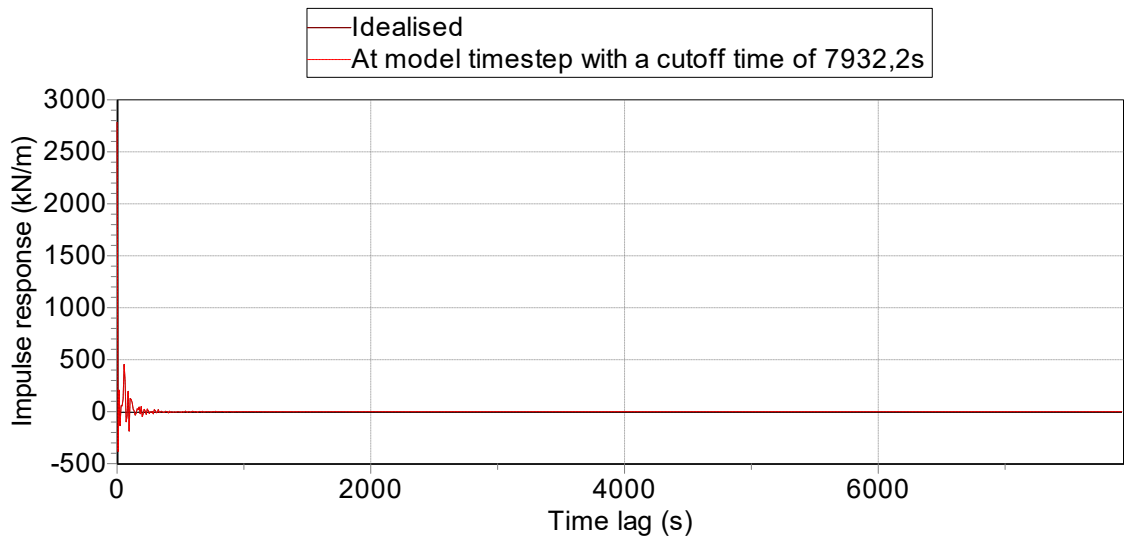
Figure 5-11 Surge-surge impulse function with standard value on the cutoff time.

OrcaFlex 10.3a
Impulse response: Vessel type1, Draught1 surge – Vessel type1, Draught1 surge component
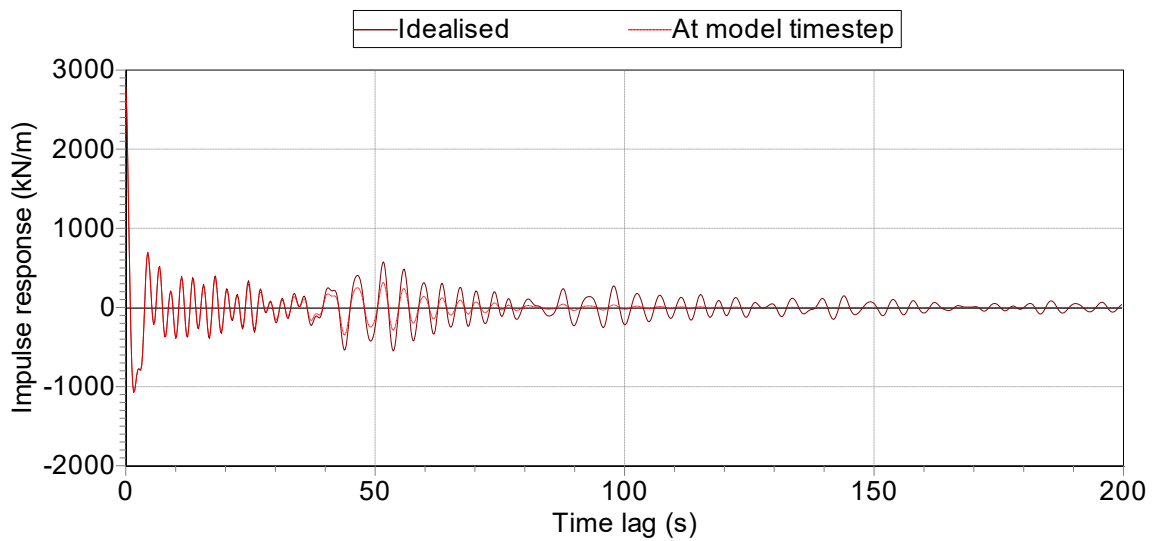
*Figure 5-12 Surge-surge impulse function with the cutoff time set to 200 s.*

OrcaFlex 10.3a
Damping: Vessel type1, Draught1 surge – Vessel type1, Draught1 surge component
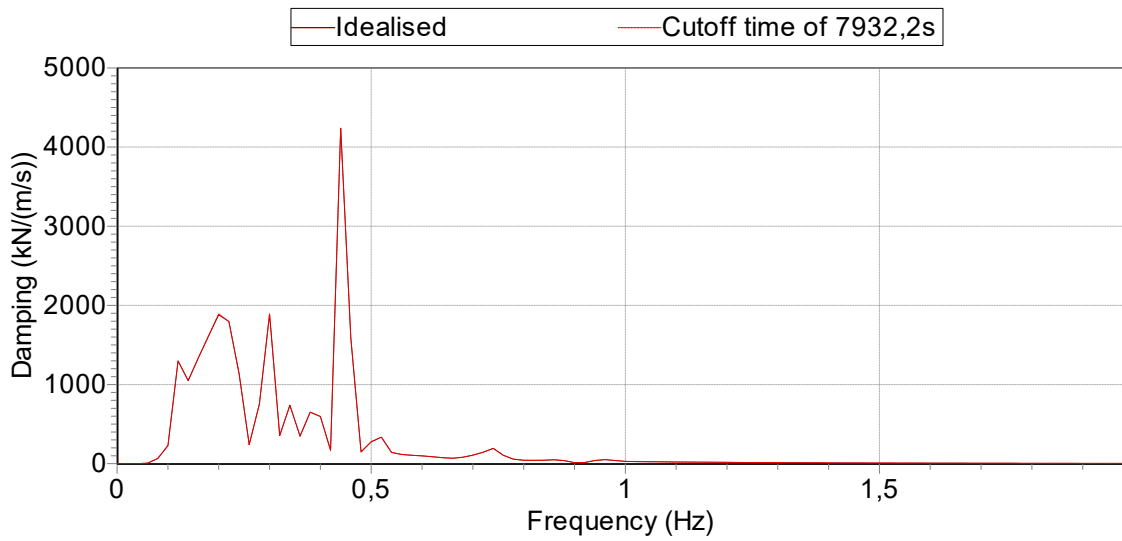
Figure 5-13 Surge-surge damping function with standard value on the cutoff time.

OrcaFlex 10.3a
Damping: Vessel type1, Draught1 surge – Vessel type1, Draught1 surge component
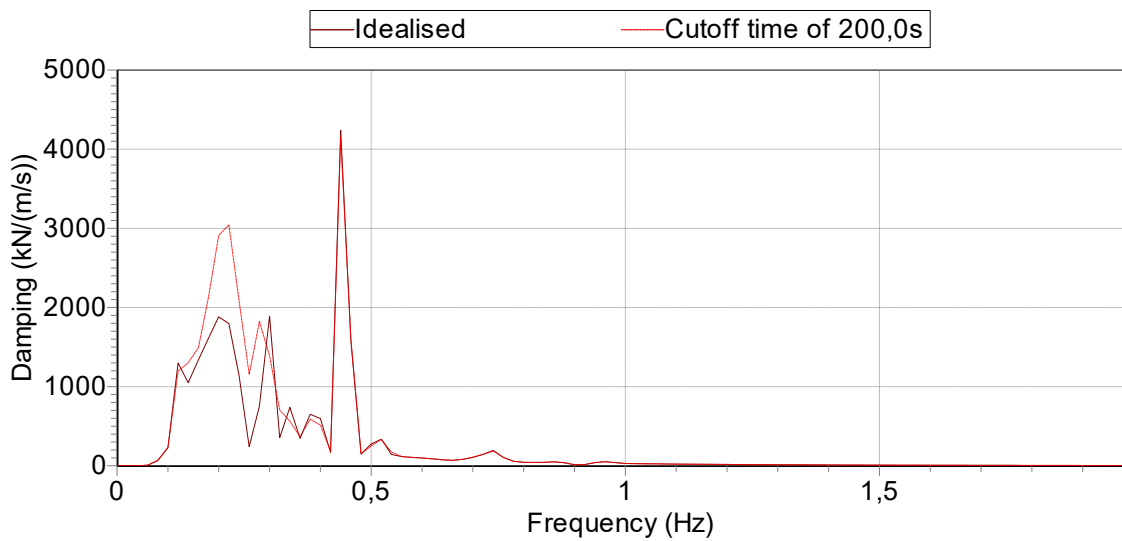
Figure 5-14 Surge-surge damping function with the cutoff time set to 200 s.

OrcaFlex 10.3a
Impulse response: Vessel type2, Draught1 pitch – Vessel type3, Draught1 heave component
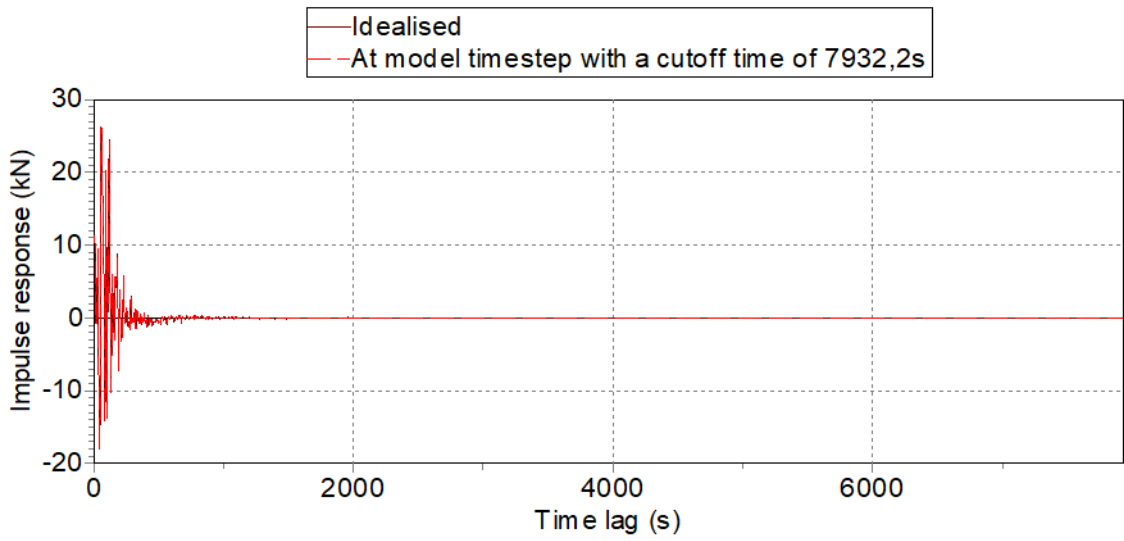
Figure 5-15 Pitch-heave impulse function with standard value on the cutoff time.

OrcaFlex 10.3a
Impulse response: Vessel type2, Draught1 pitch – Vessel type3, Draught1 heave component
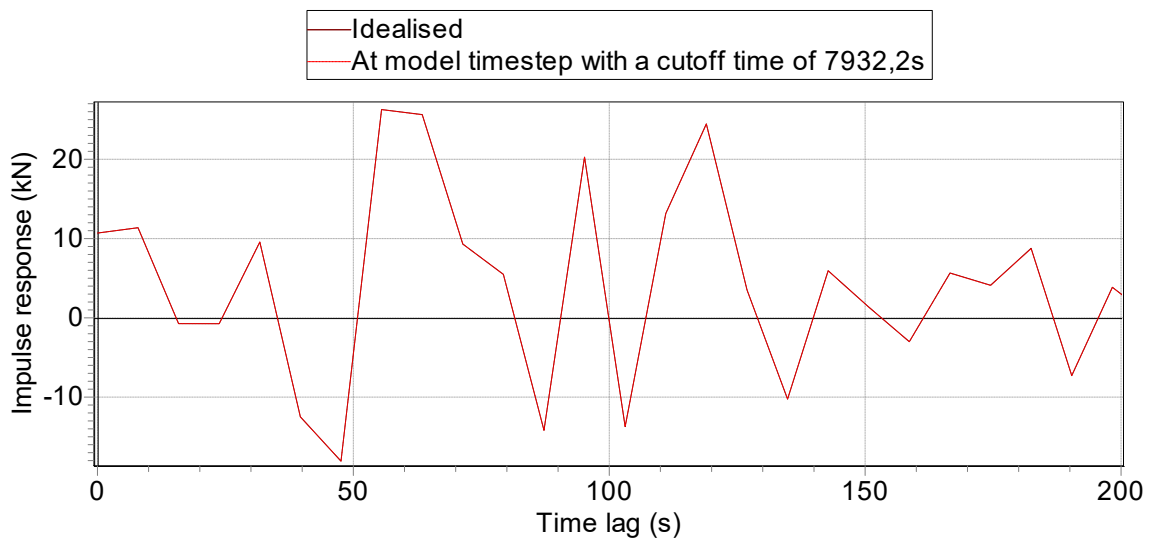
Figure 5-16 Pitch-heave impulse function with standard value on the cutoff time, but now focused on the 200 first seconds.

OrcaFlex 10.3a
Impulse response: Vessel type2, Draught1 pitch – Vessel type3, Draught1 heave component
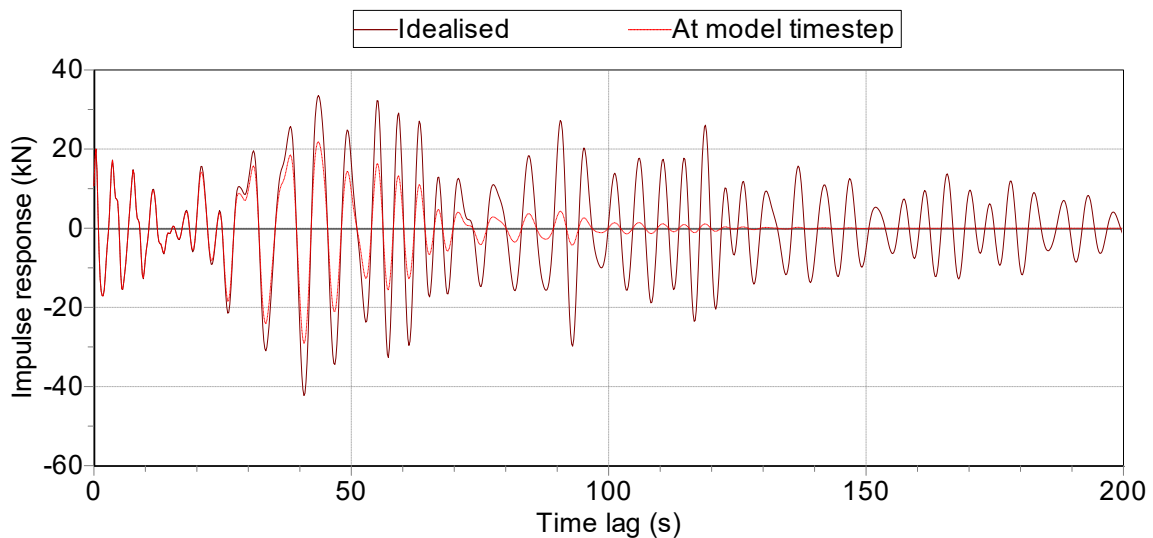
Figure 5-17 Pitch-heave impulse function with the cutoff time set to 200 s.

5.4　Discussion

The hydrodynamic analysis demonstrated that it is generally sufficient to consider three pontoons in a multibody analysis, i.e. to determine the loads on a pontoon it is enough to consider on adjacent pontoon on each side. Only small changes were observed by increasing the number of pontoons in the analysis to five or beyond. From the frequency domain OrcaFlex analysis, hydrodynamic interaction effects appear to either have little effect on or reduce the maximum bending moments about the strong axis. The bending moment about the weak axis is found to be more sensitive, especially with 100 m span width. The analysis indicates that hydrodynamic interaction effects may be more important in fatigue sea states than in ULS conditions.

The method used to study global responses in frequency domain is incomplete in the sense that some coupling terms are neglected. Future studies should consider global time domain analysis. This was also attempted here but failed due to instabilities/convergence issues related to the so-called retardation functions (the time domain equivalents of the frequency domain added mass and damping). More effort is required to overcome this issue.

One possibility that was not addressed is to neglect certain terms that are not considered important for the physical response, but that nevertheless can generate numerical problems. This has indeed been the experience when working with side-by-side mooring of LNG vessels, where the gap between the bodies is smaller and the hydrodynamic interaction stronger. Another measure that may improve the retardation functions is to use a lid in the hydrodynamic analysis in Wamit, where artificial damping is added to the free surface in order to avoid unrealistic sloshing wave elevations. This is also known to have a beneficial effect on the convergence and stability of the time domain retardation functions. The damping associated with such lids is however in general sea state dependent, and a careful calibration against model tests is necessary in order to obtain realistic values. This should be considered as future work, i.e. performing model tests designed to investigate hydrodynamic interaction effects and to calibrate the lid damping coefficient in the Wamit analysis. Such model tests need to be carefully planned in order to be valuable. The calibrated time domain model will indicate whether the frequency-domain approach is appropriate. With a validated model,

it is recommended to do further analysis to investigate the influence of hydrodynamic interaction effects on fatigue life for the chosen concept.

6   Second order wave effects

Proper calculation of second order loads on the global bridge system through full quadratic transfer functions (QTF) is numerically challenging. In the following we will concentrate on the slowly varying drift force coefficients.

Calculation of the second order potential flow force is in principle dependent on the following:

- First order motion and velocity potentials

- Wave-current interaction

- Hydrodynamic interaction.

The value of the second order slowly varying drift coefficients has previously been calculated by the OrcaFlex implementation of Newmans approximation. Whereas the Newman approximation follow the arithmetic mean of the two diagonal QTFs, OrcaFlex has implemented a variant following the geometric mean of the two diagonal QTFs. The mean drift force coefficient used as input to the OrcaFlex calculation have been based on single fixed pontoon.

Here we present the difference between the full QTF on a single fixed pontoon for a selected number of frequencies against the OrcaFlex Newman approximation implementation. The selected pontoon is the circtangle pontoon with dimensions 53 m long, 14.9 m wide and 5 m deep.

To avoid months of computational time, a pre-selection of frequencies has been done based on the following criteria; We are interested in difference periods above 20 seconds in the wind sea domain between 3 seconds and 10 seconds. With a discretization of the first order periods with a 0.2 s interval, this has given us 318 cases to analyze in WAMIT v6.4s.

The results for the sway QTF for uni-directional waves from 90 degrees are given in Figure 6-1. The results show a significant drop from the diagonal for low first order wave periods. While for higher first order periods, the QTF is relatively flat with a small increase when you move away from the diagonal. The comparison with the geometric mean Newman approximation is given in Figure 6-2, similarly the results show that the for low first order wave periods the Newman approximation is a conservative approximation. While for first order wave periods from 7-10 seconds the QTF is somewhat higher than the approximation used in OrcaFlex. The analysis has been performed for other wave directions with similar results.

It is based on this study not recommended to include the results from the full QTF into the global analysis calculation, as the Newman approximation is conservative and considerably less computational expensive.

There are however issues to be further clarified, such as the slowly-varying drift loads and damping of slowly-varying motions due to wave-current interaction effects. For the present project, the current is more significant relative to the water particle velocities than in traditional offshore applications, and it is not evident that traditional methods are valid. In order to study this in more detail, a combination of dedicated model tests and advanced numerical methods (either non-linear potential flow or CFD methods) are recommended. It should also be investigated if there are important viscous contributions to the slowly-varying wave loads, especially when the current speed is significant.

Sum-frequency loads have not been addressed in the present phase of the project. However, because the global bridge response has natural periods over a large period band from very small to large periods, one cannot conclude that these loads are not important. For instance, in a sea state with peak period $T_p = 6\ s$, there will be energetic wave components with e.g. periods $T = 5\ s$ and

$T = 7\ s$ giving rise to sum-frequency loads with frequency $f = \frac{1}{7\ s} + \frac{1}{5\ s} = 0.343\ hz$, i.e. a period of approximately 2.9 s. It is possible that such difference-frequency loading, particularly in heave, roll and pitch, may induce global responses in the bridge. It is therefore recommended to do a numerical study also of second-order sum-frequency effects in future phases of the project. In planning such study, one must be aware that sum-frequency effects can pose a numerical challenge with respect to convergence and stability. A thorough assessment of the numerical convergence is thus appropriate.
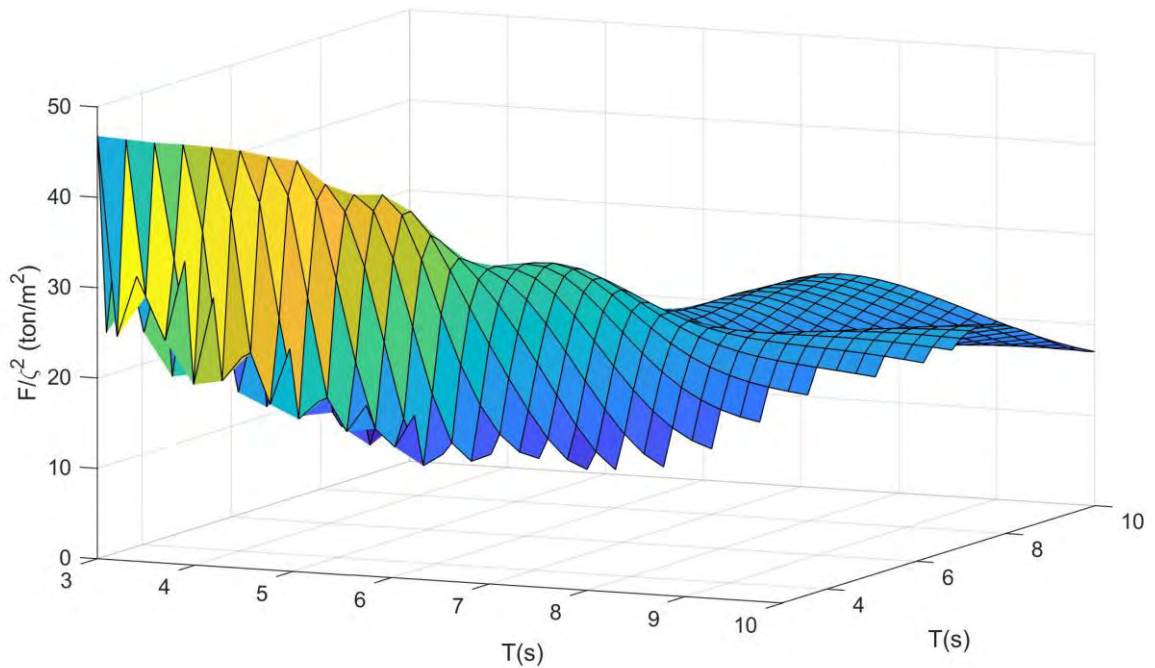
Figure 6-1 Full quadratic transfer function (QTF) for sway with waves from 90 degrees on the bridge axis for a single fixed circtangle pontoon, both sides of the diagonal is plotted).
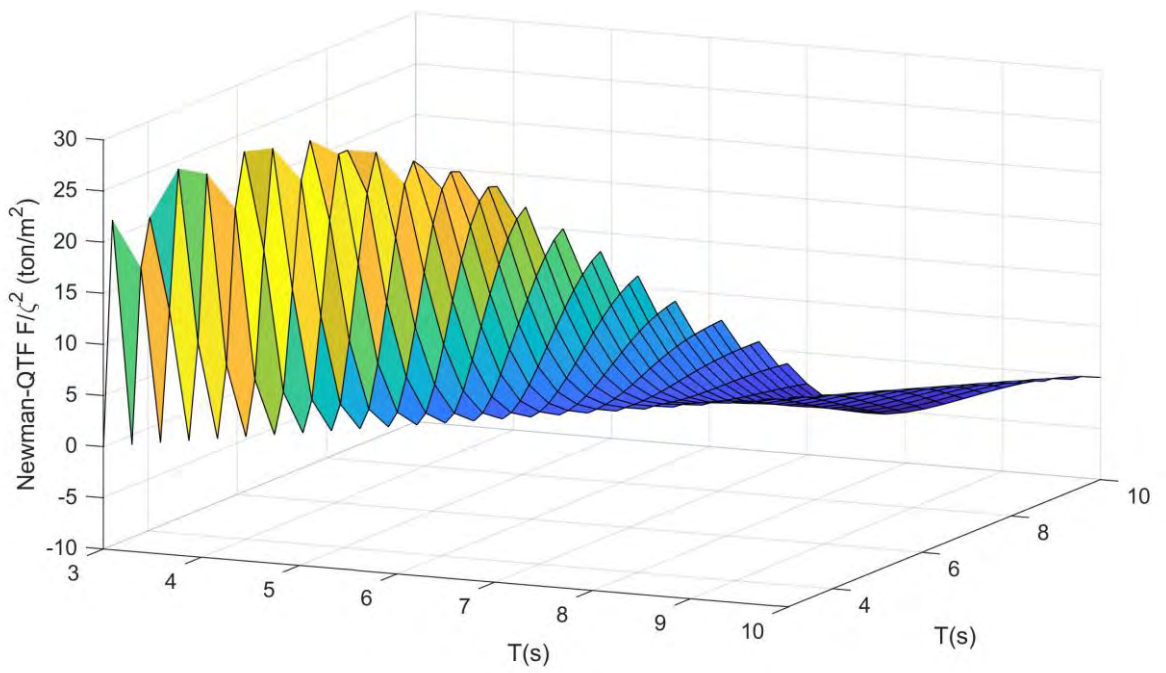
Figure 6-2 Difference between the geometric mean Newman approximation and the full QTF, (only one side of the diagonal is plotted)

7   Freeboard evaluation

The following concerns exceedance of the freeboard of pontoons due to combined bridge motions and wave action. A simplified model to account for the dynamic loading induced by negative freeboard was described in Enclosure 1, where also an extended discussion of the problem physics and relevant studies in the literature were given. Here, we give a short review of the key aspects of the model, before presenting a sensitivity study for a single pontoon in OrcaFlex.

7.1   Review of freeboard-exceedance model for OrcaFlex

As explained in Enclosure 1, a simplified model for OcraFlex is proposed in order to account for the loads induced on each pontoon due to freeboard exceedance. In general, it is found that the freeboard is only likely to be exceeded due to the combined effect of floater motions and wave elevations. The basis of the model lies in recognizing that the problem is physically similar to that of the wave-on-deck problem experienced by ship-shaped units in waves. The flow of water on deck is thus approximated using shallow-wave theory, where the pressure under the wave is essentially hydrostatic because the vertical fluid-particle motion is negligible. As found in the literature, the pressure is corrected to include the vertical acceleration of the deck. Each pontoon is divided into N strips, and the vertical force and roll moment on the pontoon are expressed as

$$F_z = \sum_{i=1}^{N} F_z(y_i),$$

$$M_x = \sum_{i=1}^{N} y_i F_z(y_i),$$

where the vertical force on strip i is expressed as

$$F_z(y_i) \equiv F_{z,i} = \rho H_i \left(g + \ddot{z}_p(y_i) \right) A_i.$$

Here ρ is the water density, g is the acceleration of gravity, $\ddot{z}_p(y_i)$ is the vertical acceleration of the pontoon and A_i is the deck area of the pontoon at strip i. $\ddot{z}_p(y_i)$ can be estimated as

$$\ddot{z}_p(y_i) = \ddot{\eta}_3 + y_i \ddot{\eta}_4,$$

where $\ddot{\eta}_3$ and $\ddot{\eta}_4$ are the heave and roll accelerations, respectively. A sketch showing the principle behind the strip model is seen in Figure 7-1.
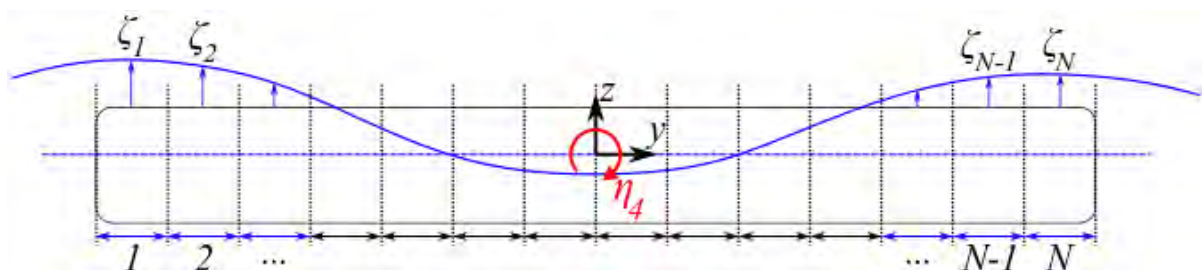

Figure 7-1 Principal sketch for simplified water-on-deck model seen from the side. In general, the pontoon is moving, but is here shown in its mean position for simplicity. The pontoon is divided into N evenly spaced strips. ζ_i is the total wave elevation at the middle of strip i. Each strip has a deck area A_i, which is here assumed to be equal for all strips. s_0 is the freeboard in still water.

The height of water on deck on each strip, H_i, is determined based on the relative vertical motion between the midpoint of the deck and the incident wave $\zeta(y_i) \equiv \zeta_i$ at the same location. The

incident wave is corrected by a factor $\nu(y_i)$ to account for diffraction effects, i.e. $\zeta_{i,tot} = \nu(y_i)\zeta_i$. For simplicity, $\nu(y_i)$ is set equal to 1.8. This is a conservative choice, since the value will in vary depending on the position and wave direction, and rarely be as large as 1.8. H_i is expressed by considering the *upwell* in the same way as is done in air gap analysis of semisubmersibles recommended in DNVGL-OTG-13 [2], i.e. the upwell at the center of strip i is given as

$$\chi_i = \alpha(y_i)\zeta_{i,tot} - z_p(y_i),$$

where $z_p(y_i)$ is the vertical displacement of the pontoons mean water line relative to the still water level expressed as

$$z_p(y_i) = \eta_3 + y_i\eta_4.$$

This variable is calculated directly inside OrcaFlex, as is ζ_i. $\alpha(y_i) \equiv \alpha$ is a wave asymmetry factor, taking into account the difference between the wave amplitude of a non-linear wave and the waves in OrcaFlex, which uses linear (Airy) wave theory. α is estimated by comparing Stokes 2nd order wave theory and Airy wave theory for regular waves with properties according to the 100 year and 10000 year given in the metocean report [11]:

- 100 year wave: $H_s = 2.1\ m, T_p = 5.0\ s$

- 10000 year wave: $H_s = 2.9\ m, T_p = 6.1\ s$.

The results following from this approach are plotted in Figure 7-2. As can be seen, the wave steepness is relatively similar between the 100 and 10000 year waves, and the asymmetry factor is close to 1.15. As a conservative estimate, we therefore take $\alpha = 1.2$ in the analysis. This allows for the wave asymmetry factor to also include a contribution from non-linear diffraction effects, even though these are not expected to be as severe in the present scenario as they can be for semisubmersibles in harsh offshore conditions. As a result, the height of water on deck is expressed as

$$H(y_i) \equiv H_i = \begin{cases} \chi_i - s_0 & if & \chi_i > s_0 \\ \\ 0 & otherwise \end{cases}.$$

where s_0 is the still-water freeboard equal to 3.5 m. In other words, if the upwell is less than this, the height of water on deck is zero.
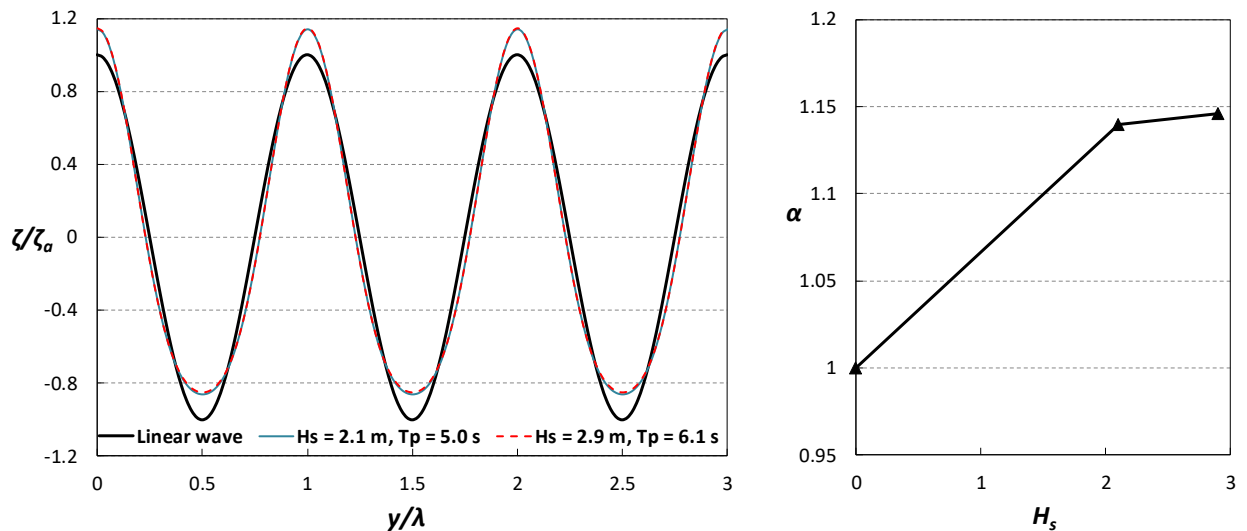
Figure 7-2 Estimation of wave asymmetry factor for 100 and 10000 year waves. $\zeta^{(1)}$ and $\zeta^{(2)}$ are the wave elevations estimated from linear (Airy) wave theory and 2nd order Stokes theory, respectively, λ is the wavelength and α is the asymmetry factor estimated as $max(\zeta^{(1)}) / max(\zeta^{(2)})$.

The model described above is implemented in OrcaFlex, so that the loading on a pontoon due to excess of freeboard is computed at every time step and imposed in the pontoon's equation of motion as external heave forces and roll moments. The model is schematically shown in Figure 7-3.
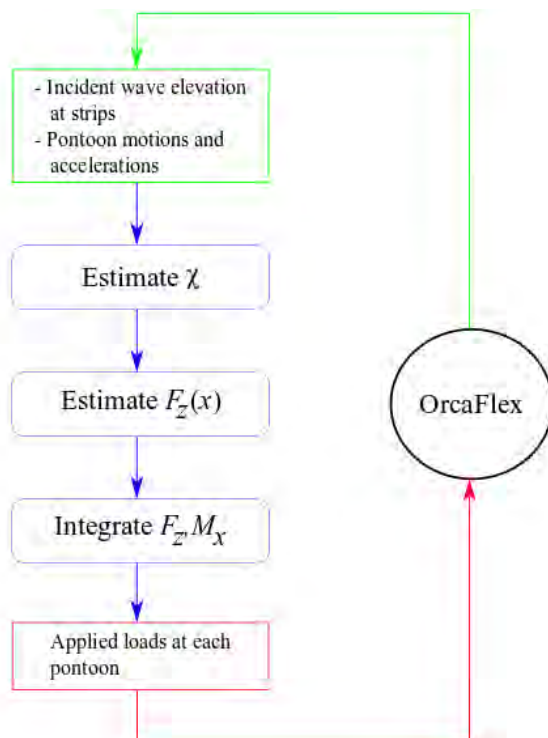
Figure 7-3 Schematic view of the water-on-deck model implemented in OrcaFlex.

7.2 Sensitivity studies

In order to examine the global effects of including the model described in the previous section in OrcaFlex, as single pontoon is modelled (Figure 7-4) with several combinations of added heave and roll stiffness (ΔC_{33} and ΔC_{44}) applied in the top of the column to represent the stiffness contribution to a single pontoon from the global bridge structure. The additional restoring is adjusted to give the following natural heave and roll periods, confirmed through decay tests:

- $T_{n3} = 3.7 \ s$ (approximately equal to mode with lowest natural period) and $T_{n3} = 5.0 \ s$ (close to a representative wave peak period)

- $T_{n4} = 5.0 \ s$ (close to a representative wave peak period).
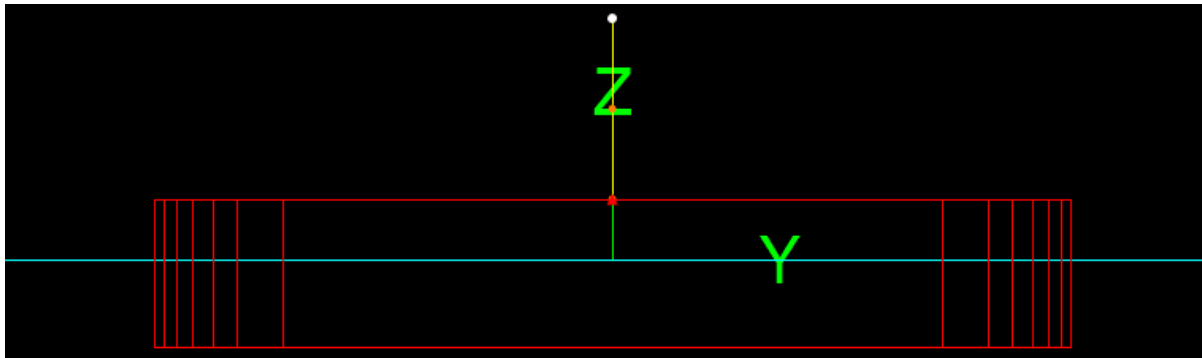
Figure 7-4 Model of a single pontoon in OrcaFlex. Additional restoring is applied at the top of the column.

Results of the performed decay tests are shown in Figure 7-5 - Figure 7-7. For the heave decay tests, it is clearly seen that the wave-radiation (potential) damping is much larger for the higher natural period.
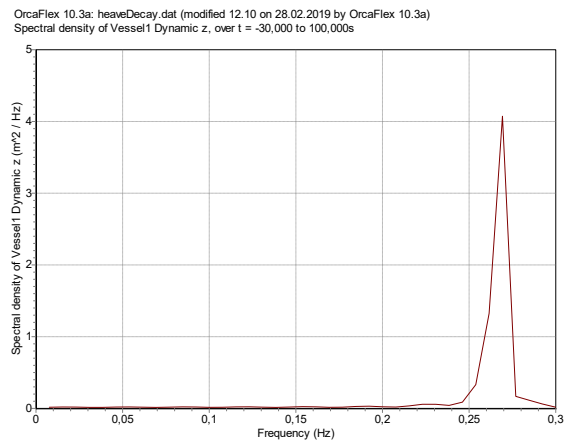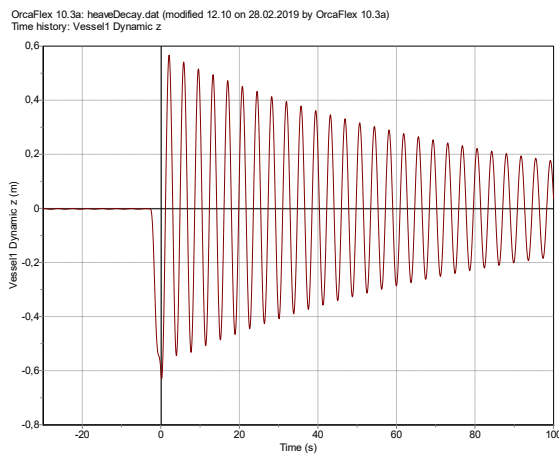
Figure 7-5 Heave decay test with $\Delta C_{33} = 16500 \ kN/m$ giving $T_{n3} = 3.7 \ s$.
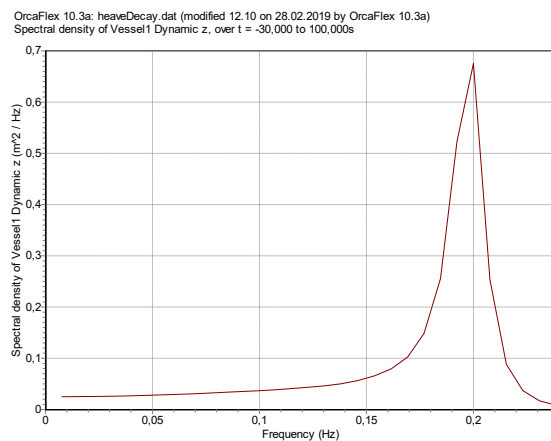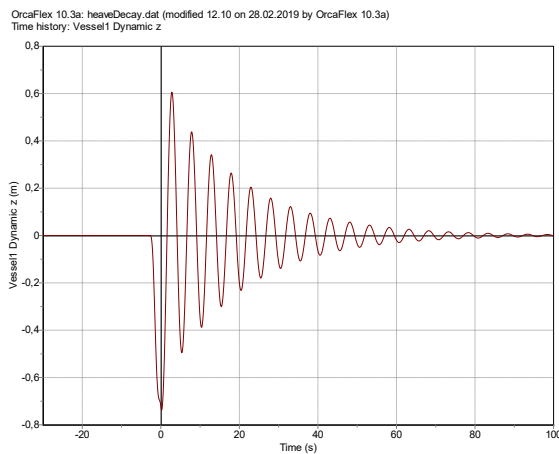
Figure 7-6 Heave decay test with $\Delta C_{33} = 4850 \ kN/m$ giving $T_{n3} = 5.0 \ s$.
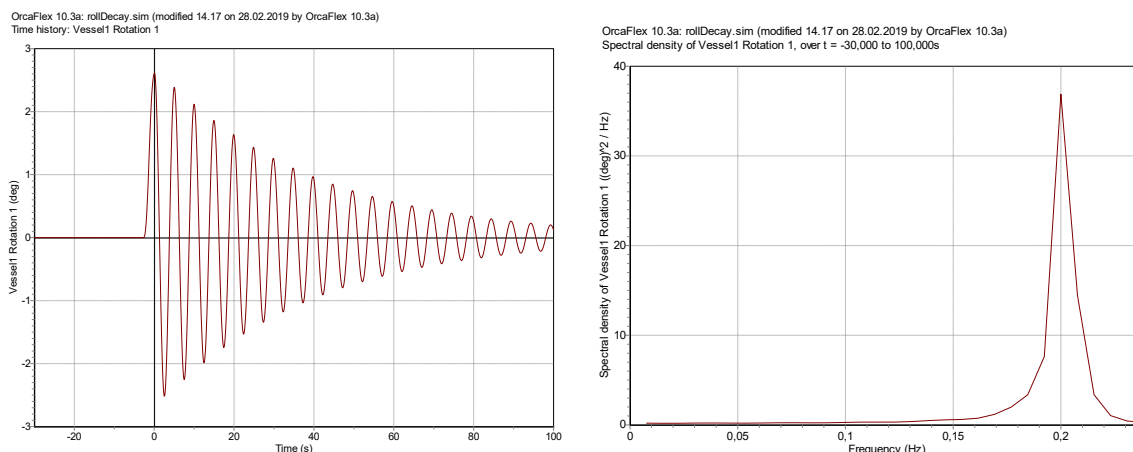
Figure 7-7 Roll decay test with $\Delta C_{44} = 30000 \; kNm/rad$ giving $T_{n5} = 5.0 \; s$.

The number of strips used in the strip model is taken as $N = 25$, which is expected to be sufficient. No additional sensitivity studies are performed for this variable.

With the model free to move in the xy plane, the following one-hour irregular sea states are simulated with and without the freeboard exceedance model activated for the same wave realization as listed in Table 7-1, where γ is the peak enhancement factor in the JONSWAP wave spectrum and θ is the incident wave direction. $\theta = 90°$ means that the wave direction is aligned with the longitudinal axis of the pontoon. Furthermore, the effect of short-crested waves is investigated by performing simulations with and without wave spreading.

Table 7-1 Sea states used to simulate the response of a single pontoon with and without the freeboard exceedance model activated in OrcaFlex.

H_s (m)	T_p (s)	γ (−)	θ (°)	Wave spreading	T_{n3} (s)	T_{n4} (s)
2.1	5.3	2.3	90	0	5.0	5.0
2.1	5.3	2.3	90	10	5.0	5.0
2.1	5.3	2.3	90	0	3.7	5.0
2.1	5.3	2.3	90	10	3.7	5.0
2.9	6.1	2.3	90	0	5.0	5.0
2.9	6.1	2.3	90	10	5.0	5.0
2.9	6.1	2.3	90	0	3.7	5.0
2.9	6.1	2.3	90	10	3.7	5.0

7.2.1 Results for 100 year sea states

Figure 7-8 – Figure 7-11 show the loads induced by freeboard exceedance and the resulting floater motion for the four 100 year sea states defined in Table 7-1, and with response spectra for heave and roll motion in Figure 7-12. Even though there are several events where the freeboard is exceeded, the induced loads have only a moderate effect on the heave and roll motions. In general, the effect on heave motion is more significant than on roll motion. For $T_{n3} = 5.0 \; s$, the heave motions are generally slightly reduced due to water-on-deck loading, while for $T_{n3} = 3.7 \; s$ they increase. The latter is likely because the heave force "impulses" are seen to be relatively short, and are more likely to amplify responses with short natural periods.

The effect of short-crested waves is small to negligible.
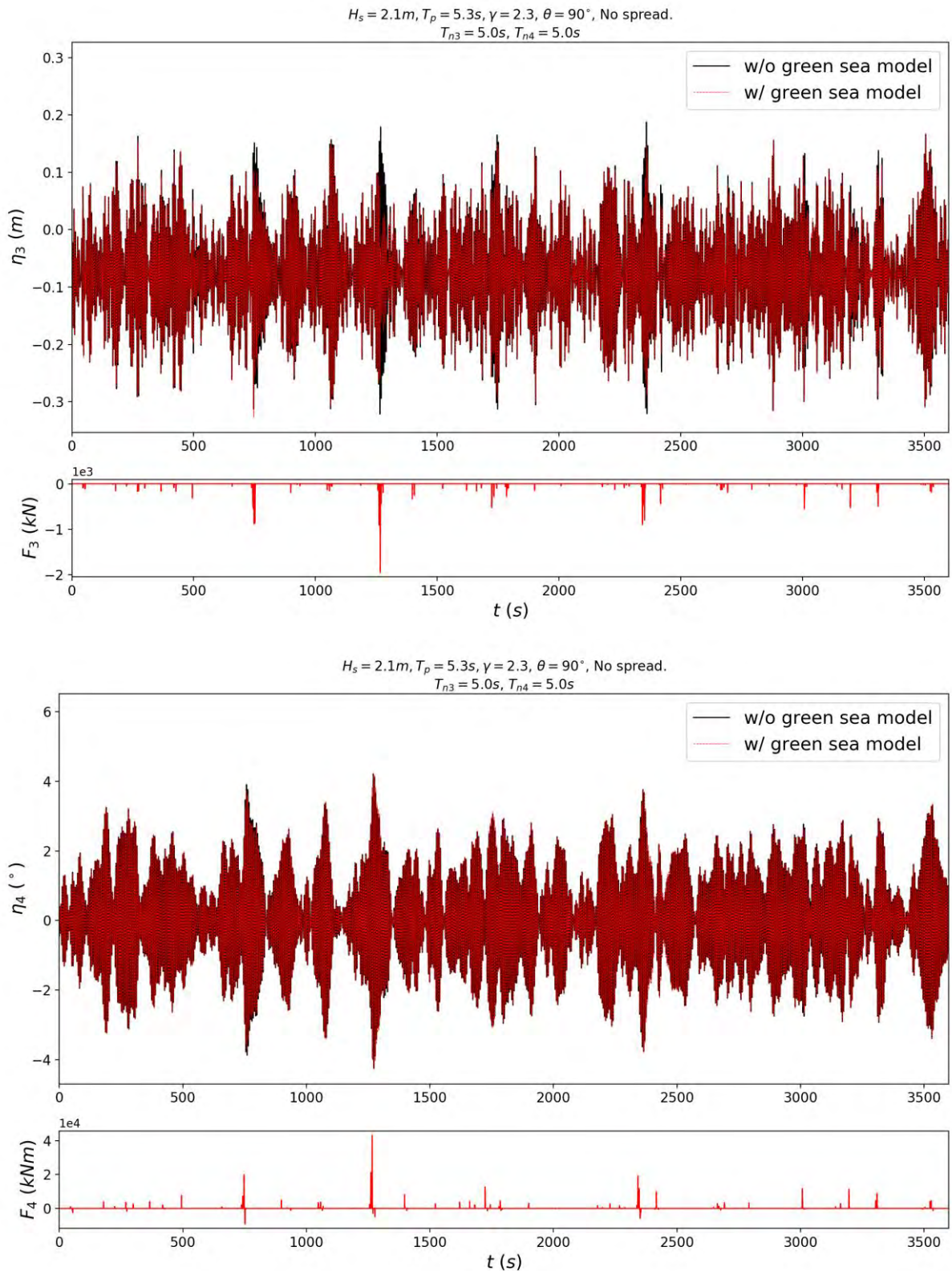
Figure 7-8 Time series of applied loads and resulting pontoon motions in heave and roll for $H_s = 2.1\ m, T_p = 5.3\ s$ with $T_{n3} = 5.0\ s, T_{n4} = 5.0\ s$ and no wave spreading.
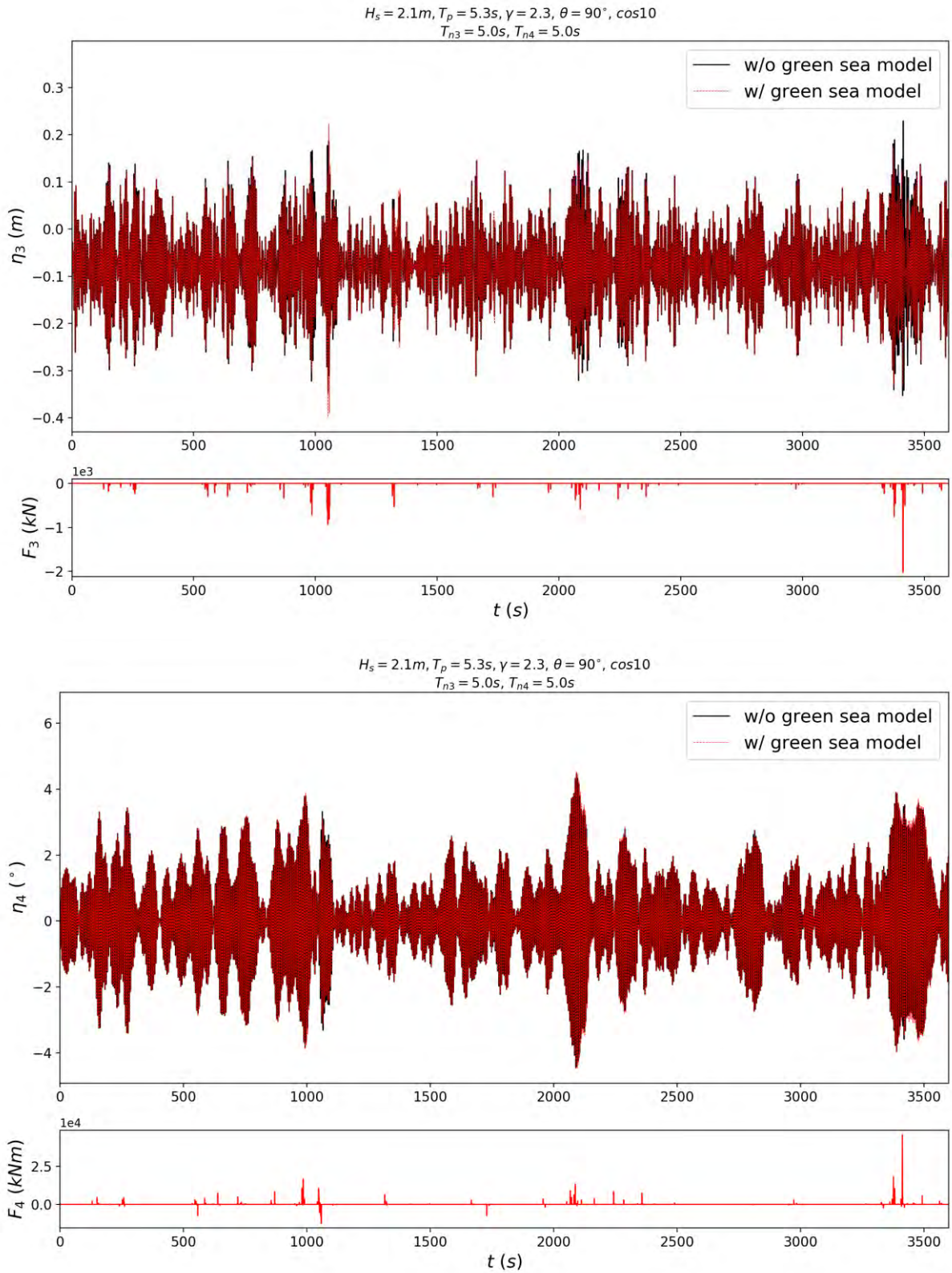
Figure 7-9 Time series of applied loads and resulting pontoon motions in heave and roll for $H_s = 2.1\ m, T_p = 5.3\ s$ *with* $T_{n3} = 5.0\ s, T_{n4} = 5.0\ s$ *and with wave spreading.*
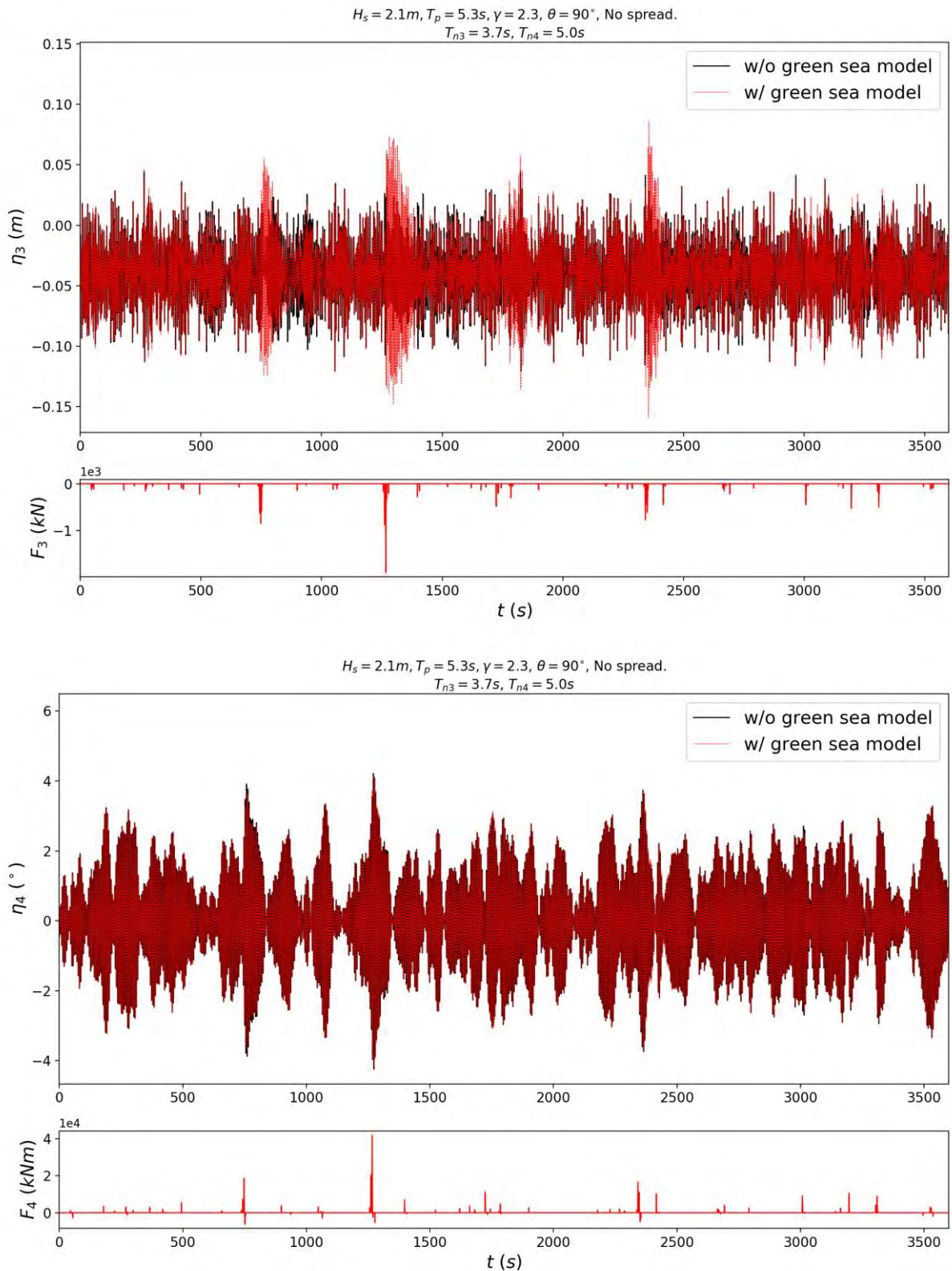
Figure 7-10 Time series of applied loads and resulting pontoon motions in heave and roll for $H_s = 2.1\ m, T_p = 5.3\ s$ with $T_{n3} = 3.7\ s, T_{n4} = 5.0\ s$ and no wave spreading.
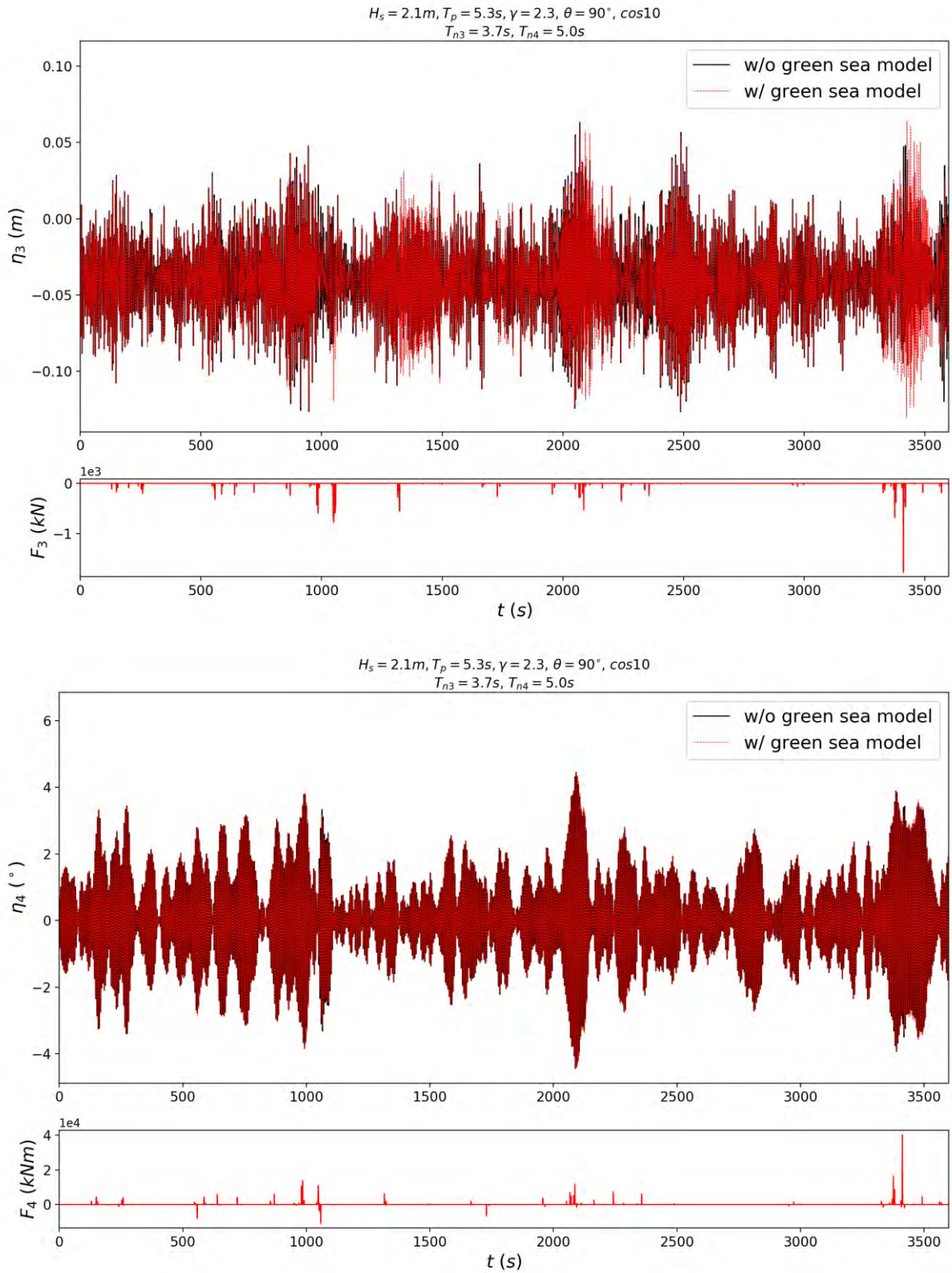
Figure 7-11 Time series of applied loads and resulting pontoon motions in heave and roll for $H_s = 2.1\,m, T_p = 5.3\,s$ with $T_{n3} = 3.7\,s, T_{n4} = 5.0\,s$ and with wave spreading.
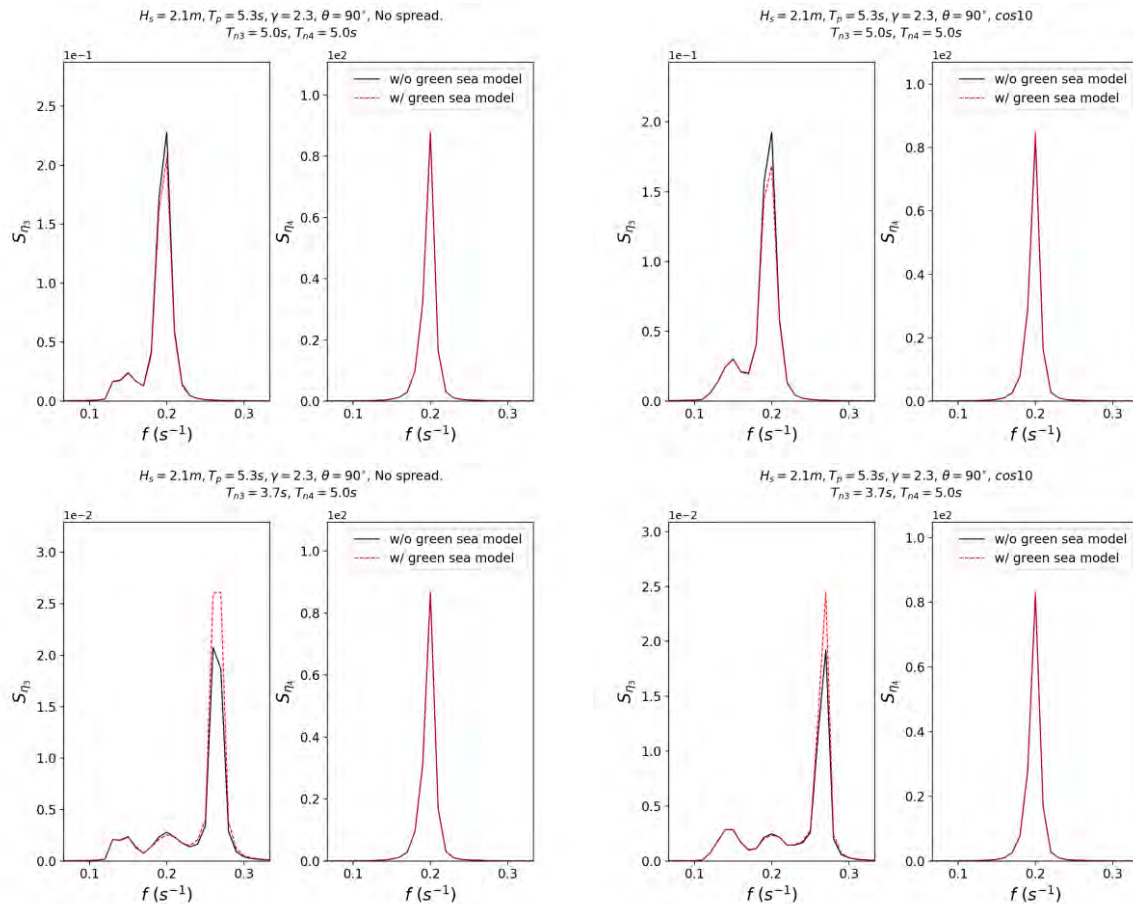
Figure 7-12 Heave and roll response spectra for 100 year sea states defined in Table 7-1.

7.2.2 Results for 10000 year sea states

Figure 7-13 - Figure 7-16 show the loads induced by freeboard exceedance and the resulting floater motion for the four 10000 year sea states defined in Table 7-1, and with response spectra for heave and roll motion in Figure 7-17.

As for the 100 year sea states, the water-on-deck loading is generally seen to reduce heave motions when $T_{n3} = 5.0 \ s$ while amplifying them for $T_{n3} = 3.7 \ s$.

The effect on roll motions is again small, as is the effect of short-crested waves. However, in Figure 7-14 a severe spike in the heave motion is seen around 1200 s in the case of short-crested waves that was not observed for long-crested waves. A sensitivity study is performed where the time step in the simulation is reduced, without changing the result. Hence, the observed effect is more likely due to an unfavorable combination of events. Indeed, by looking closer at the vertical force, it is observed that several water-on-deck load impulses follow shortly after each other. For the pontoon as a mechanical system, the effect is probably like having a single impulse with longer duration. Consequently, a large heave response is induced. Thus, for the 10000 year wave it appears that the wave spreading may have an adverse effect on the response of the floater. However, it is just as likely that the observation is linked to short-term variability rather than long vs. short-crestedness, i.e. that we just happened to encounter a severe combination of events.
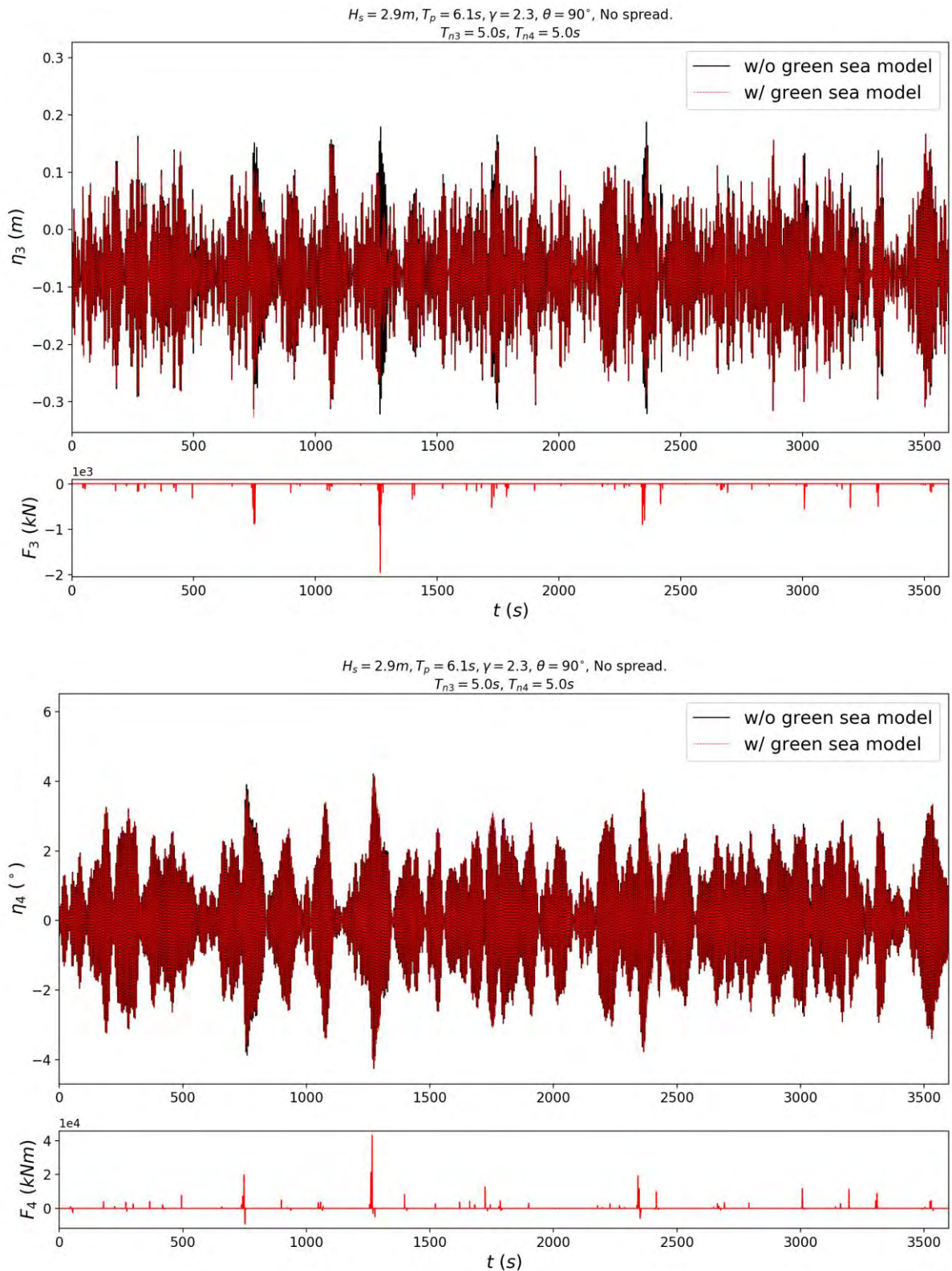
*Figure 7-13 Time series of applied loads and resulting pontoon motions in heave and roll for $H_s = 2.9\ m, T_p = 6.1\ s$ with $T_{n3} = 5.0\ s, T_{n4} = 5.0\ s$ and no wave spreading.*
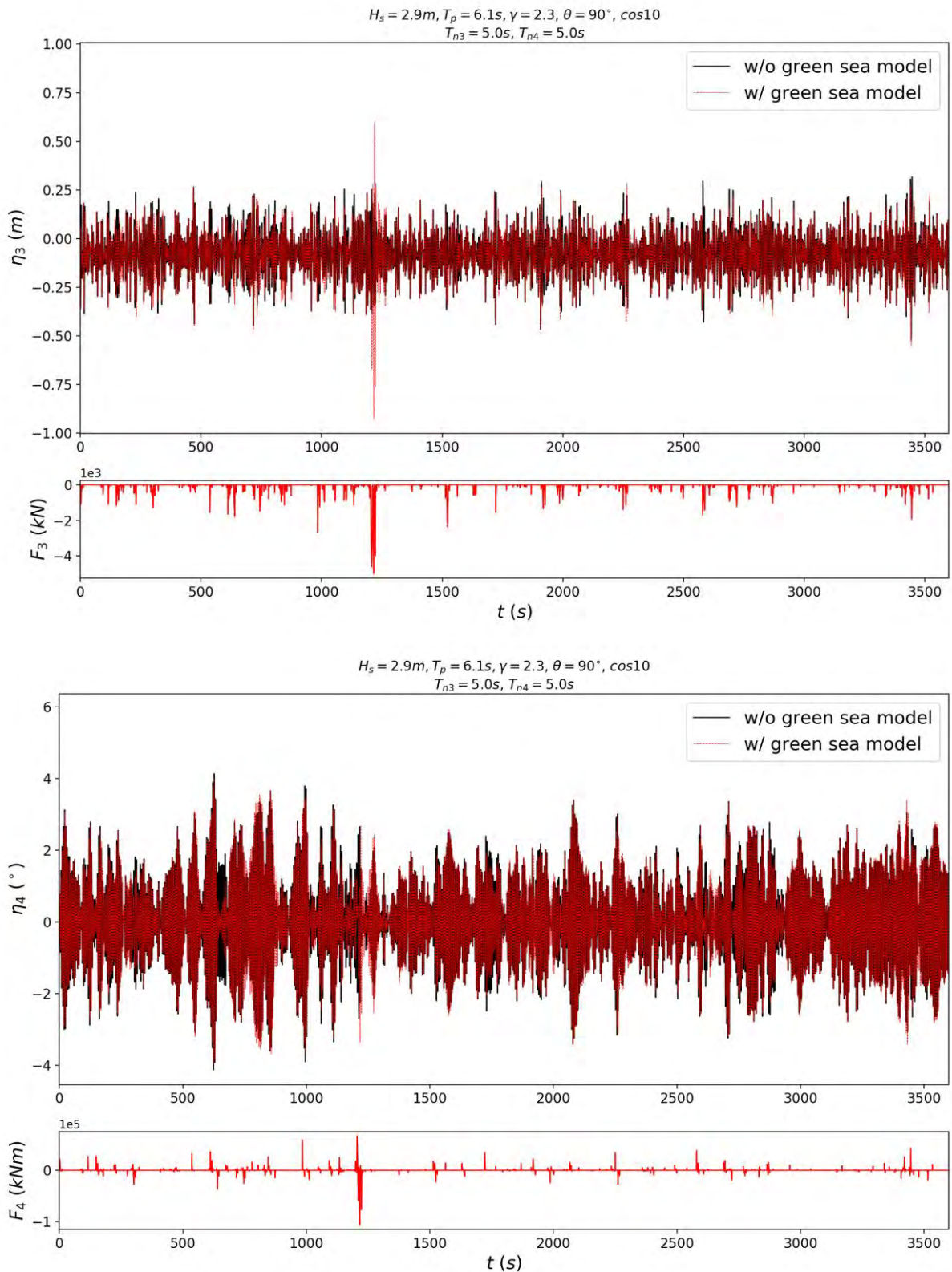
Figure 7-14 Time series of applied loads and resulting pontoon motions in heave and roll for $H_s = 2.9\,m, T_p = 6.1\,s$ with $T_{n3} = 5.0\,s, T_{n4} = 5.0\,s$ and with wave spreading.
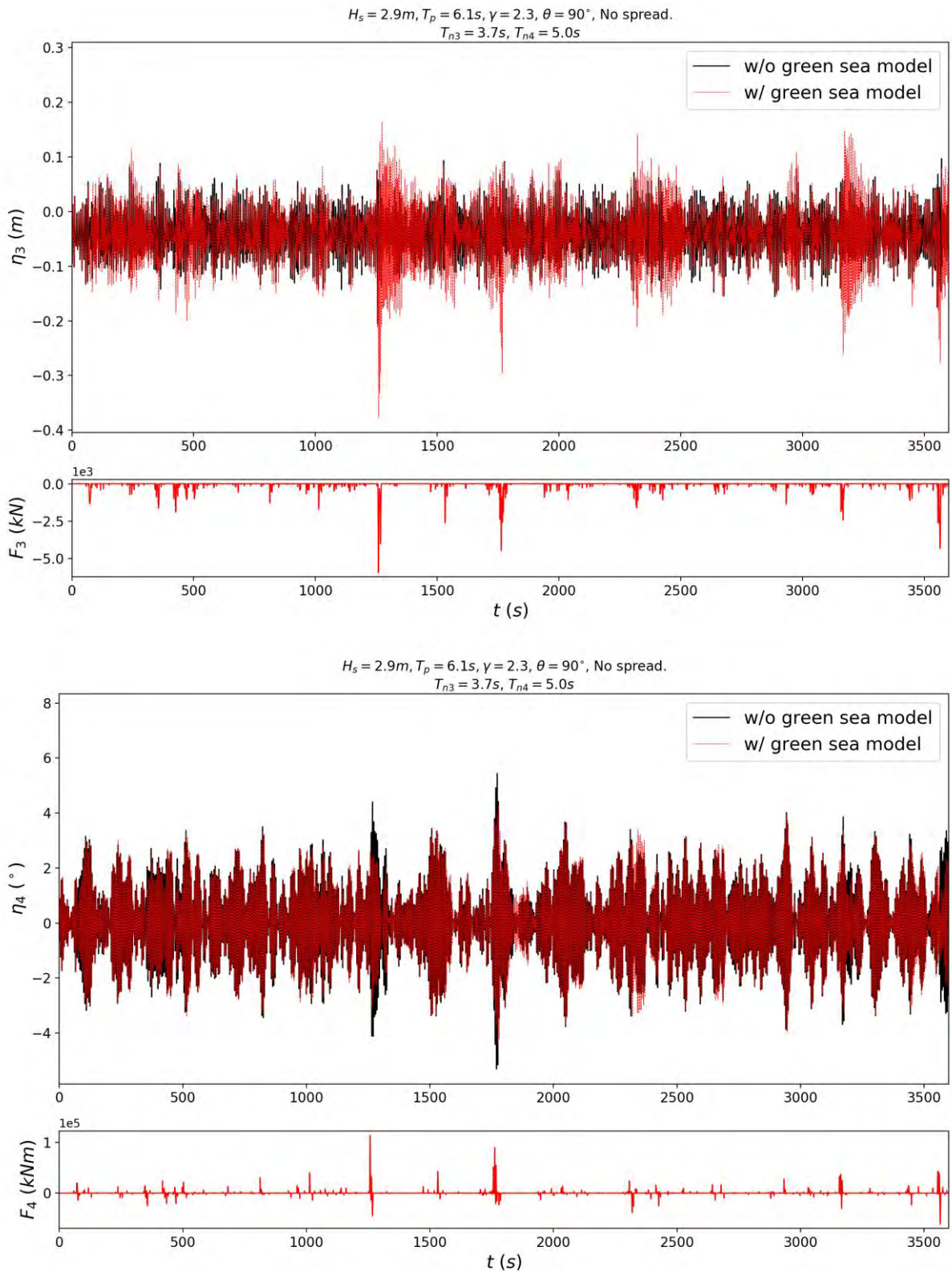
Figure 7-15 Time series of applied loads and resulting pontoon motions in heave and roll for $H_s = 2.9\,m, T_p = 6.1\,s$ with $T_{n3} = 3.7\,s, T_{n4} = 5.0\,s$ and no wave spreading.
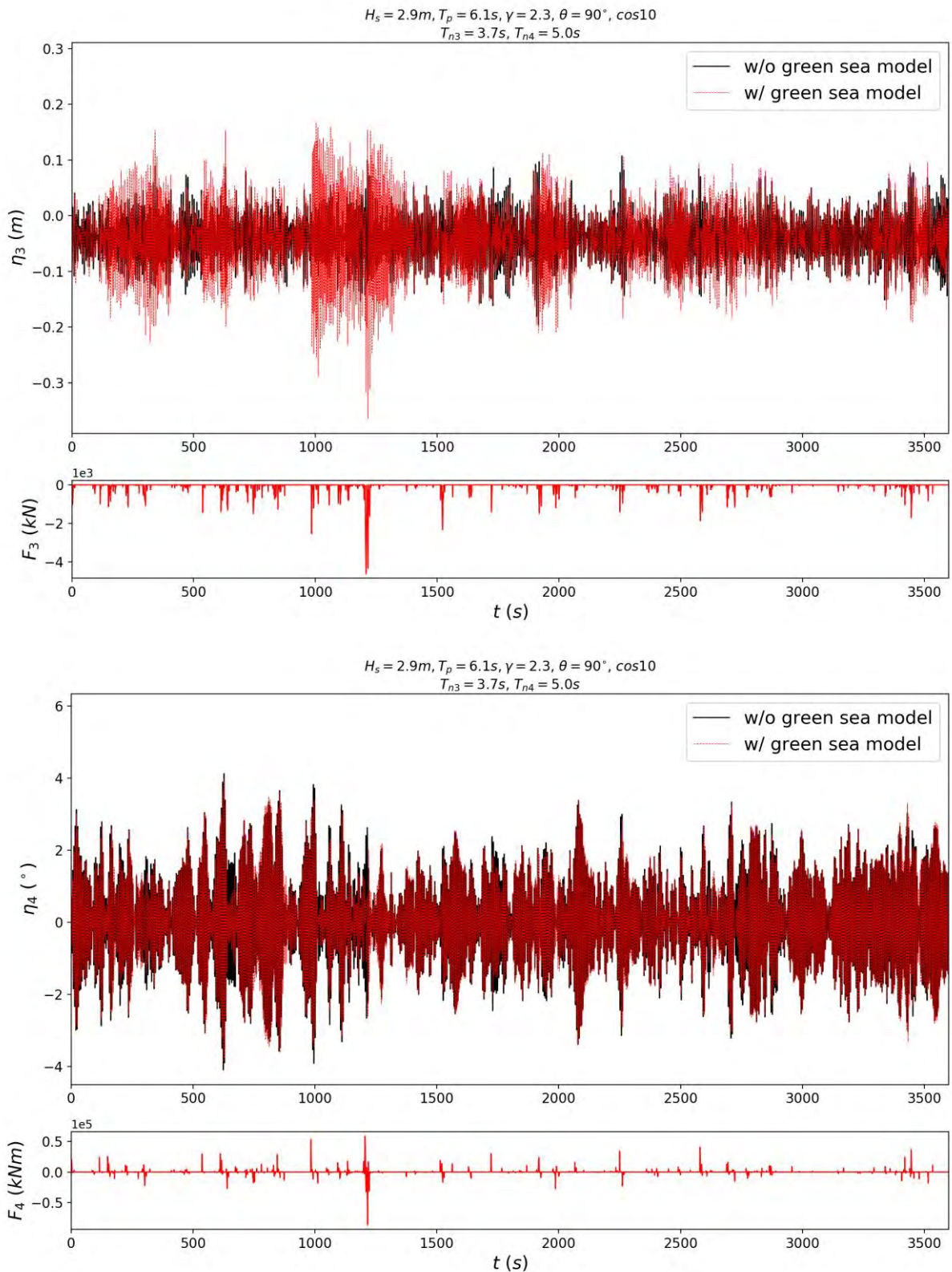
Figure 7-16 Time series of applied loads and resulting pontoon motions in heave and roll for $H_s = 2.9\ m, T_p = 6.1\ s$ with $T_{n3} = 3.7\ s, T_{n4} = 5.0\ s$ and with wave spreading.
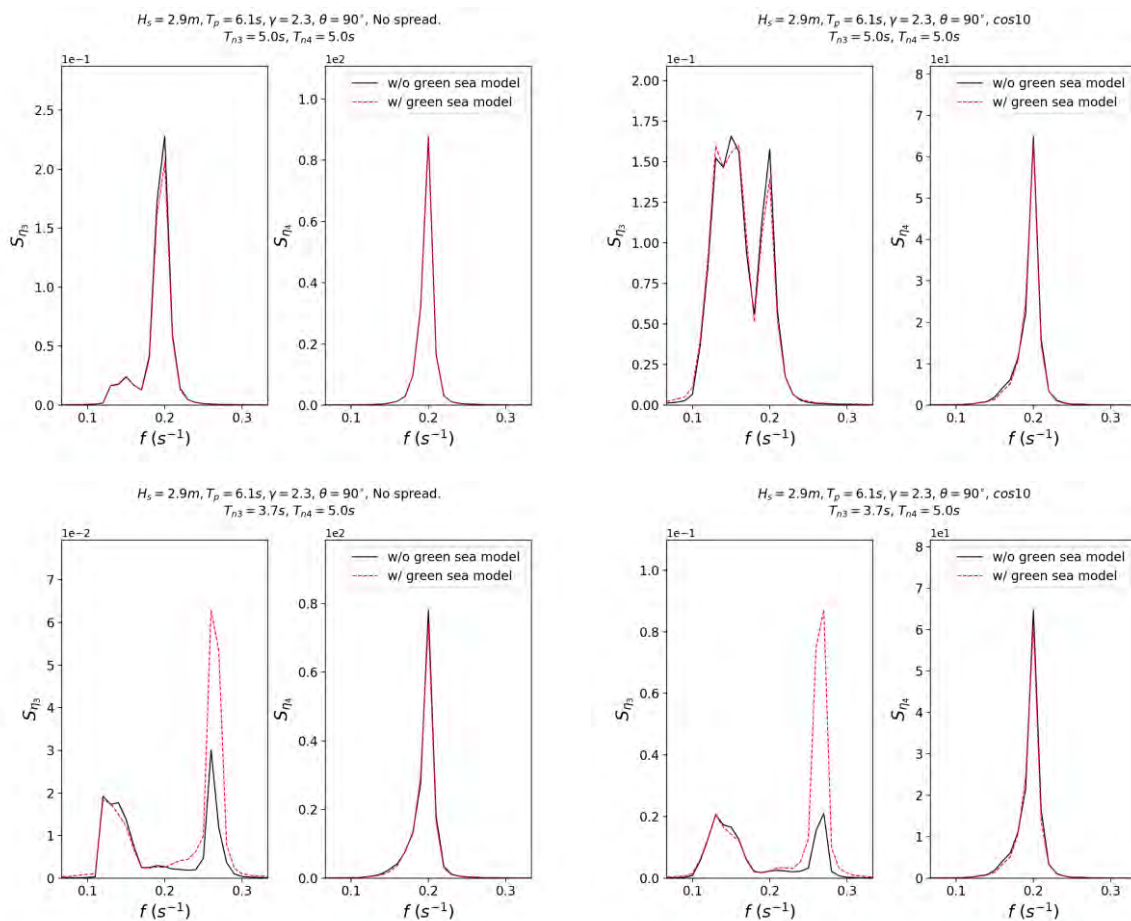
Figure 7-17 Heave and roll response spectra for 10000 year sea states defined in Table 7-1.

7.3 Global analysis results

The described methodology has been implemented and tested on the K11_06 model. Two environmental conditions have been tested: a 100-year wind-wave sea state with heading normal to the bridge ($H_s = 2.1\ m$ and $T_p = 5.2\ s$). The second is a generic condition with artificially high waves to force some difference with and without the freeboard exceedance model. For this we have chosen $H_s = 3.5\ m$ and $T_p = 5.2\ s$, and denoted the condition as *higher*. The results are presented in Figure 7-18 for the strong axis bending moment and in Figure 7-19 for the weak axis bending moment. The results for the case with the 100-year wind wave does not show any influence from freeboard exceedance. For the generic extreme case there is some increase in both the strong axis and the weak axis moment due to freeboard exceedance. However, one should keep in mind that this wave is significantly higher than the 10 000-year sea state given in the metocean design basis
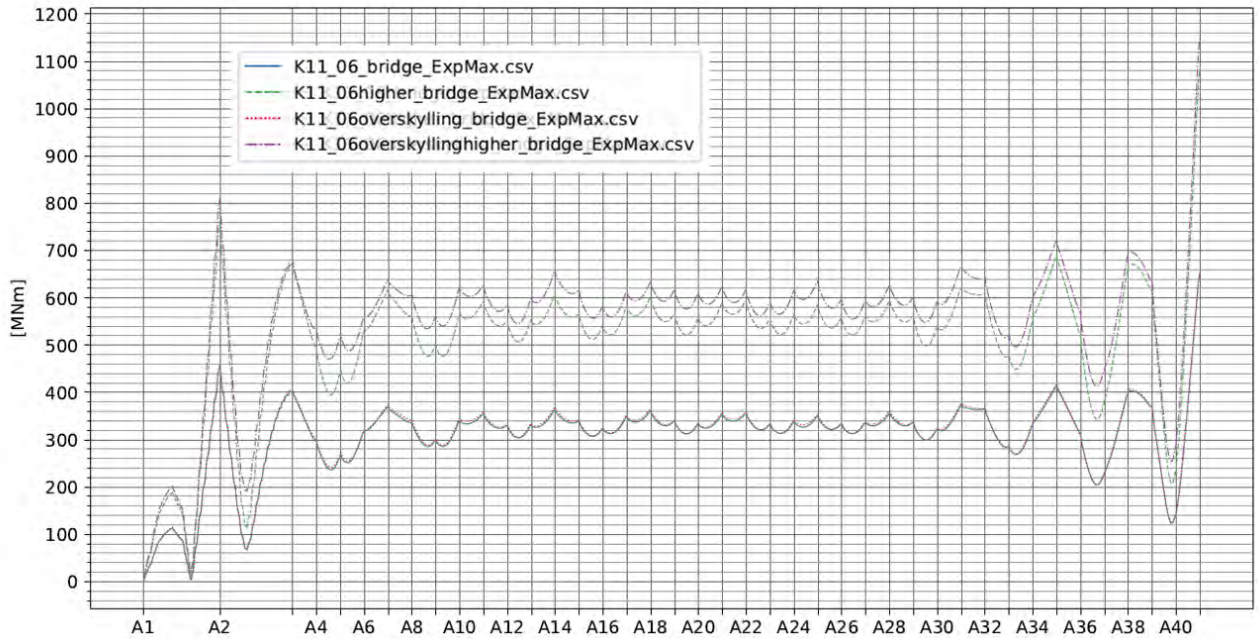
Figure 7-18 Strong-axis bending moment from global analysis simulation for the bridge model K11_06 with and without freeboard exceedance model.
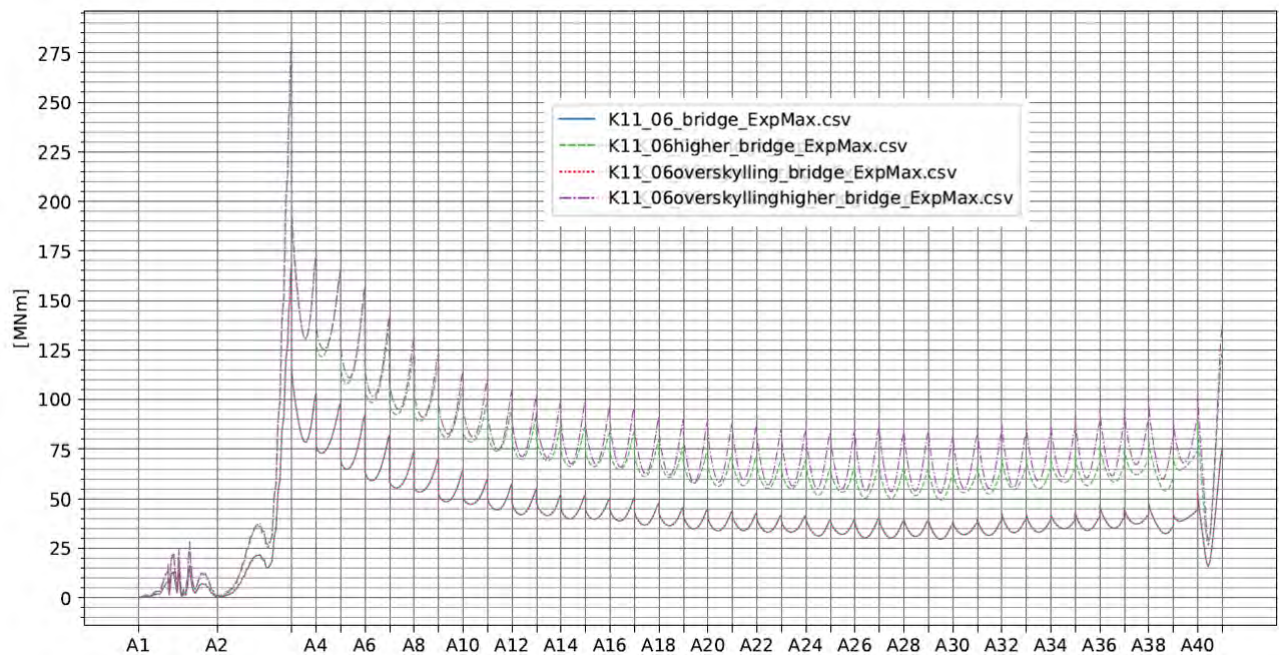

Figure 7-19 Weak-axis bending moment from global analysis simulation for the bridge model K11_06 with and without freeboard exceedance model.

7.4 Conclusive remarks on freeboard exceedance

The proposed freeboard exceedance model has been tested for a single pontoon in 100 and 10000 year irregular waves, varying the natural period in heave in order to examine the effect on different modes corresponding to the global response of the bridge. Several events where freeboard is exceeded are observed both in the 100 and 10000 year condition. As expected, the magnitude of water-on-deck loads, and their frequency of occurrence, are largest for the 10000 year condition. In general, it is found that imposed loads due to excess of a pontoon freeboard may

1. reduce responses with long natural periods

2. amplify responses with short natural periods.

In practice, it seems that adverse effects at the 100 year return period level are only likely to be seen for the shortest mode included in the present study, i.e. the case where the heave natural period is set equal to 3.7 s. Moreover, the effect of short-crested waves does not significantly affect the water-on-deck loads and induced motions relative to the simulations with long-crested waves.

For the 10000 year condition, a particularly large heave response is observed with wave spreading included, exciting heave motion with natural period 5 s. Thus, one may not formally conclude that the influence of wave spreading is insignificant with respect to water-on-deck loading. However, it is deemed more likely that the observation is due to short-term variability and a particularly unfavorable combination of floater motions and wave elevation.

The present study is meant to verify that the model works as intended, and to understand the nature of the induced loading and its ability to induce motions that may influence the global response of the bridge. The boundary conditions and the behavior of the modelled single pontoon are inevitably less complex than when the pontoon is actually included in the global bridge model. Although it seems reasonable that the induced responses will be less for a pontoon that is part of the global model than for the single pontoon studied here, this should be verified by including the proposed model for all pontoons in the global model and run some relevant scenarios in time domain. This is in order to complete the understanding of the loading process, where the following issues are relevant:

1. Is there a risk that the water-on-deck loading induces adverse responses through global coupling effects?

2. It is reasonable to assume that the loads induced on individual pontoons are relatively uncorrelated i.e. statistically independent. However, what is the effect if negative freeboard is detected at numerous pontoons simultaneously?

The simplified assessment indicates that exceedance of the freeboard is not a cause of great concern for the considered scenarios but may be provoked in extreme sea states outside of the 10 000 year contour.

For future work, it is recommended that the proposed freeboard model is verified by performing model tests and/or CFD analysis prior to drawing any conclusions from a more comprehensive global simulation scheme.

8 References

[1] DNV-GL, *RP-C205 - Environmental conditions and environmental loads,* 2017.

[2] DNV GL, "Offshore Technical Guidance DNVGL-OTG-13 Prediction of air gap for column, Edition March 2017," 2017.

[3] D. Sumner, H. Heng and A. Beitel, "The effect of aspect ratio on the aerodynamic forces and bending moment for a surface-mounted finite-height cylinder," *Journal of Wind Engineering & Industrial Aerodynamics,* vol. 186, p. 204–213, 2019.

[4] N. Rostamy, D. Sumner, D. J. Bergstrom and J. D. Bugg, "Local flow field of a surface-mounted finite circular cylinder," *Journal of Fluids and Structures,* vol. 34, pp. 105-122, 2012.

[5] V. Venugopal, K. S. Varyani and N. D. P. Barltrop, "Wave force coefficients for horizontally submerged rectangular cylinders," *Ocean Engineering,* vol. 33, pp. 1669-1704, 2006.

[6] B. M. Sumer and J. Fredsøe, Hydrodynamics around cylindrical structures, World Scientific, 2006.

[7] CoreMarine, "Document No: CMA-19-008-MCO-RT-001 Potoon CFD," 2019.

[8] DNV GL Software, "Sesam User Manual, WASIM v. 5.5," 2017.

[9] DNV GL Software, "Sesam User Manual, WADAM v. 9.4," 2017.

[10] T. K. Vada, "DNV GL Webinar, Hydrodynamics with forward speed, 27th November 2018".

[11] Statens Vegvesen, "SBJ-01-C4-SVV-01-BA-001 MetOcean Design basis Rev. 1," 30.11.18.

[12] AMC, "SBJ-33-C5-AMC-21-RE-108 : Appendix H: Global Analyses - Special studies Rev. 0," 15-08-2019.

9 Enclosures

Enclosure 1 F.-C. W. Hanssen, "10205546-09-NOT-067 AMC status 2 - A simplified model to implement freeboard exceedance scenarios in OrcaFlex", rev. 1, 29.03.2019

Enclosure 2 CFD analysis report for viscous forces on pontoon, CMA-19-008-MCO-RT-001 PONTOON CFD, Rev. B3.